

**Nanoscale magnetometry  
with a single spin  
in diamond at cryogenic temperatures**

**Inauguraldissertation**

zur  
Erlangung der Würde eines Doktors der Philosophie  
vorgelegt der  
Philosophisch-Naturwissenschaftlichen Fakultät  
der Universität Basel

von

*Lucas Thiel*

aus Brombach, Deutschland

Basel, 2019



This work is licensed under a Creative Commons  
Attribution-NonCommercial-NoDerivatives 4.0 International License.

The complete text may be reviewed here:

<http://creativecommons.org/licenses/by-nc-nd/4.0/>



Genehmigt von der Philosophisch-Naturwissenschaftlichen Fakultät  
auf Antrag von  
Prof. Dr. Patrick Maletinsky  
Prof. Dr. Vincent Jacques

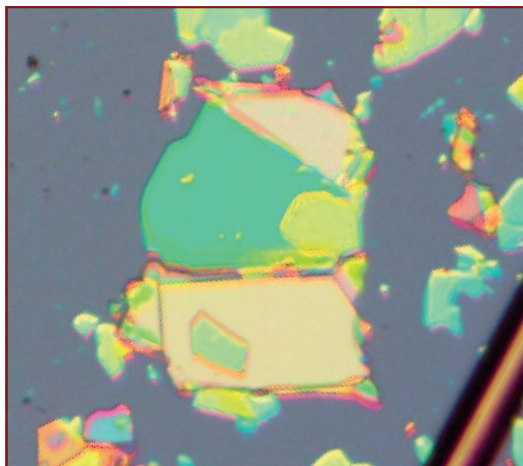
Basel, den 21.05.2019

Prof. Dr. Ralph Ubl  
Dekan

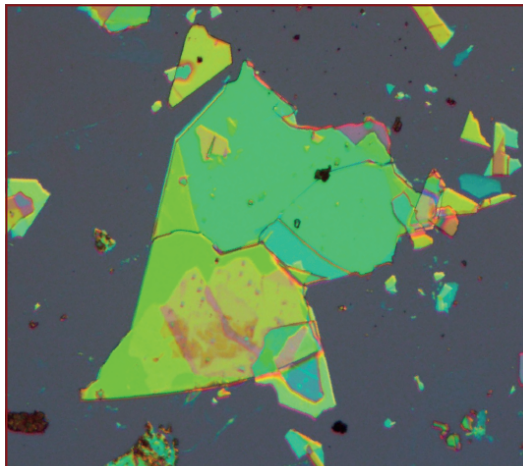


*Fortunately, I didn't have to do it all by myself...*

*...I had help of a small manikin...*



*...and a small dinosaur!*





# Abstract

Individual electronic spins can yield close-to-ideal magnetometers to investigate magnetic phenomena on the nanoscale. Spins offer sensitivity to magnetic fields by virtue of the Zeeman effect and can be localized to atomic length scales, which enables nanoscale resolution in imaging. The electronic spin of the Nitrogen-Vacancy (NV) center in diamond has been identified as a particularly fruitful system to implement these concepts, as its additional ability of optical spin initialization and readout renders the NV center a non-invasive and quantitative magnetometer with single-spin sensitivity and nanoscale spatial resolution. Nitrogen-Vacancy based magnetometry has been widely exploited exclusively under ambient conditions. Advancing the frontiers of nanoscience at low temperature, however, hinges on the availability of novel sensors for nanoscale imaging such as the Nitrogen-Vacancy center.

To fill this gap, in this thesis we developed and employed an NV-based scanning magnetometer at cryogenic temperatures. We present the implementation of an atomic force microscope, which is functionalized with a single NV center, situated in a liquid helium bath cryostat, and interfaced with a confocal microscope for optical initialization and readout of the NV's electronic spin. We demonstrate DC magnetic field sensitivities better than  $\mu\text{T}/\sqrt{\text{Hz}}$  and an unprecedented spatial resolution of 30 nm. Moreover, we introduce powerful post-processing techniques and employ them on the recorded quantitative magnetic stray field maps. This allows for the retrieval of important material parameters by recovering the underlying planar current distribution or spin texture.

To demonstrate the performance of our cryogenic magnetometer, we focused on nanoscale studies of magnetic phenomena in superconductors. We were able to image stray fields of individual vortices with highest spatial resolution and perform nanoscale studies of the Meissner effect in superconductor nanostructures. Both of these measurements enabled the unambiguous determination of the London penetration depth, allowed for the inspection of nanoscale defects inhibiting superconductivity and for benchmarking competing, microscopic models for supercurrent flow.

In a second experiment, the application of the cryogenic scanning setup to recently discovered two-dimensional magnets in van der Waals heterostructures led to one of the key results of this thesis. We quantitatively determined the magnetization of a monolayer  $\text{CrI}_3$  and demonstrated that the magnetic coupling between individual layers in a multi-layer stack  $\text{CrI}_3$  is intimately connected to the material structure, and that structural modifications can induce a relaxation to the magnetic ground state, which has not been observed so far in this material.

Our results therefore illustrate the power of NV magnetometry in exploring local magnetic properties of electronic systems with high resolution, and the great potential for future nanoscale explorations of a large range of complex, condensed matter systems at cryogenic temperatures.





# Contents

<b>Titel</b>	<b>a</b>
<b>Abstract</b>	<b>i</b>
<b>Contents</b>	<b>k</b>
<b>List of symbols and abbreviations</b>	<b>m</b>
<b>1. Introduction</b>	<b>1</b>
<b>2. Cryogenic magnetometry with a single spin in diamond</b>	<b>5</b>
2.1. NV center physics and magnetic imaging . . . . .	6
2.1.1. Electronic structure and optical properties . . . . .	7
2.1.2. Optically detected magnetic resonance . . . . .	9
2.1.3. Response to DC magnetic fields . . . . .	11
2.1.4. Full field imaging . . . . .	13
2.1.5. Iso-field imaging . . . . .	13
2.2. Reverse Propagation . . . . .	16
2.2.1. Upward and downward continuation . . . . .	18
2.2.2. Reconstruction of vector magnetic field from single field component . . . . .	19
2.2.3. Reconstruction of two-dimensional magnetization . . . . .	20
2.2.4. Reconstruction of two-dimensional current distribution . . . . .	23
2.2.5. Windowing technique . . . . .	24
2.3. Implementation of the cryogenic setup . . . . .	26
<b>3. Magnetic imaging of superconductors</b>	<b>31</b>
3.1. Theoretical background . . . . .	31
3.1.1. London penetration depth and coherence length . . . . .	32
3.1.2. Type-I vs type-II superconductor and vortices . . . . .	34
3.2. Experimental Realization . . . . .	37
3.2.1. Yttrium barium copper oxide fabrication and samples . . . . .	37
3.2.2. Quantitative vortex imaging and analysis . . . . .	39
3.3. Summary and outlook . . . . .	46
<b>4. Two-dimensional magnetic systems</b>	<b>51</b>
4.1. Motivation: 2D magnetic materials . . . . .	51
4.2. CrI <sub>3</sub> – a ferromagnetic 2D material . . . . .	52
4.3. Sample preparation . . . . .	59
4.4. Quantitative magnetization measurements of CrI <sub>3</sub> . . . . .	61

4.5. Summary . . . . .	69
4.6. Outlook . . . . .	69
<b>5. Summary and Outlook</b>	<b>75</b>
5.1. Summary . . . . .	75
5.2. Outlook . . . . .	76
<b>A. Appendix</b>	<b>83</b>
A.1. NV magnetometry . . . . .	83
A.1.1. Fabrication of NV cantilevers . . . . .	83
A.1.2. History of deployed NV cantilevers . . . . .	86
A.1.3. SEM images of broken cantilever devices . . . . .	87
A.1.4. General remarks on Fourier-space propagation . . . . .	87
A.1.5. Pulsed experiments and field dependent ODMR contrast . . . . .	89
A.2. Superconductivity . . . . .	91
A.2.1. Flux quantization . . . . .	91
A.2.2. Determination of stray field sign in NV magnetometry . . . . .	92
A.2.3. Numerical implementation of vortex stray fields . . . . .	93
A.2.4. Magnetic field data . . . . .	94
A.3. Two-dimensional magnetic systems . . . . .	95
A.3.1. Characterization of $\text{CrI}_3$ samples . . . . .	95
A.3.2. Direct measurement of the magnetization . . . . .	98
A.3.3. Influence of DMI on a domain wall . . . . .	100
A.3.4. Stray magnetic field of a 1D spin chain . . . . .	101
A.3.5. Magnetic field data . . . . .	102
A.3.6. Raman spectra . . . . .	104
A.4. Current Imaging in Graphene . . . . .	105
A.5. Code snippets . . . . .	106
A.5.1. Calculation of $k$ values . . . . .	106
A.5.2. $B_x$ , $B_y$ and $B_z$ from $B_{\text{NV}}$ . . . . .	107
A.5.3. $M_z$ from $B_{\text{NV}}$ . . . . .	109
A.5.4. $J$ from $B_{\text{NV}}$ . . . . .	111
<b>B. Bibliography</b>	<b>I</b>
<b>Curriculum Vitae</b>	<b>XXIII</b>

# List of symbols and abbreviations

## Abbreviations:

---

2D	two-dimensional
AC	alternating current
A-FM	anti-ferromagnet
AFM	atomic force microscope
AFP	adiabatic fast passage
CVD	chemical vapor deposition
DC	direct current
DFT	density functional theory
DMI	Dzyaloshinskii-Moriya interaction
FFT	fast Fourier transform
FM	ferromagnet
h-BN	hexagonal boron nitride
HT	high temperature
ISO	iso-magnetic
LT	low temperature
MFM	magnetic force microscopy
MRFM	magnetic resonance force microscopy
MOKE	magneto-optic Kerr effect
MW	microwave
NA	numerical aperture
NV	Nitrogen-Vacancy
ODMR	optically detected magnetic resonance
PLD	pulsed laser deposition
RF	radio-frequency
RHEED	reflection high-energy electron diffraction
RMS	root mean square
SEM	scanning electron microscope
SQUID	superconducting quantum interference device
TMF	transverse magnetic focusing
ZPL	zero-phonon line

## Chemical elements and compounds:

---



---

Br	bromine
Cl	chlorine
Cr	chromium
CrI <sub>3</sub>	chromium triiodine
F	fluorine
He	helium
I	iodine
N <sub>2</sub>	nitrogen
Si	silicon
SiO <sub>2</sub>	silicon dioxide
STO	SrTiO <sub>3</sub>
YBCO	YBa <sub>2</sub> Cu <sub>3</sub> O <sub>7-<math>\delta</math></sub>

## Constants:

---



---

$e = 1.602 \cdot 10^{-19} \text{ C}$	elementary charge
$\gamma_{\text{NV}} = 2.79 \text{ MHz/G}$	gyromagnetic ratio NV spin
$h = 6.626068 \cdot 10^{-34} \text{ m}^2\text{kg/s}$	Planck's constant
$\hbar = 1.05457148 \cdot 10^{-34} \text{ m}^2\text{kg/s}$	reduced Planck's constant
$k_B = 1.38064852 \cdot 10^{-23} \text{ m}^2\text{kg/s}^2\text{K}$	Boltzmann constant
$\mu_B = 9.274009994 \cdot 10^{-24} \text{ J/T}$	Bohr magneton
$\mu_0 = 4\pi \cdot 10^{-7} \text{ Tm/A}$	vacuum permeability
$\theta_{\text{NV}} = \arccos(1/\sqrt{3}) = 54.74^\circ$	characteristic angle in NV geometry
$g_e \approx 2.0002$	NV electron g-factor
$\Phi_0 = h/2e = 2.07 \text{ mT}\mu\text{m}^2$	flux quantum

## Physical Quantity:

---



---

<b>A</b>	magnetic vector potential
<b>B</b>	magnetic field
$B_c$	critical field in superconductivity
$B_{\text{NV}}$	magnetic field projected on the NV axis
$B_{\text{NV}}^{\text{bias}}$	static background magnetic field along the NV axis
$\xi$	coherence length in superconductivity
<b>E</b>	electric field
$E_C$	condensation energy in superconductivity
$E_B$	expulsion energy in superconductivity
<b>J</b>	current

---

$\mathcal{J}$	exchange constant
$J_c$	critical current in superconductivity
$\lambda_L$	London penetration depth in superconductivity
$\Lambda$	effective London penetration depth in superconductivity
$m$	mass
$m^*$	effective mass of a Cooper pair
$n_s$	number density of superconducting electrons
$\Phi$	magnetic flux
$\sigma_z$	out-of-plane magnetization in $\mu_B/\text{nm}^2$
$\sigma_z^{\text{mono}} = 14.7 \mu_B/\text{nm}^2$	monolayer $\text{CrI}_3$ magnetization
$T$	temperature
$T_c$	critical temperature in superconductivity
$z_{\text{NV}}$	NV sample distance

Units:

---



---

A	Ampere
g	gram
h	hours
Hz	Hertz
K	Kelvin
m	meter
nm	nanometer
s	seconds
T	Tesla
$\mu\text{m}$	micrometer



# 1. Introduction

Human beings interact with the environment on a daily basis using their senses. They can touch material to get a feeling of its texture, they can taste food and smell odors, they can get a visual impression of the world around them and listen to its sounds to learn about their surrounding environment. Sensing capabilities are of unique and vital importance and help us to react on events and changes.

In former times, researchers used only their god-given senses to observe nature and deduce laws and dependencies from it like Darwin's theory of evolution or Newton's law of motion. Our senses are however only qualitative in that we can differentiate between smooth and rough surfaces, mild and hot taste, pleasant and stinky odor, close and distant objects or quite and loud environment. What we cannot, is to put a precise number on these quantities. Nowadays however, it is not only necessary to measure qualitatively, we also need more precise, more sensitive and higher resolution measurements as we keep exploring the world from the big scale down to micro-organisms, molecules and atoms. Consequently, we need tools that are sensitive to quantities to which humans are not, such as light beyond the visible spectrum, pressure or magnetic fields, in order to discover new aspects of the world. Therefore, humans expanded their senses by constantly trying to develop and improve sensors through novel technologies.

At the forefront of current research are sensors based on quantum systems with sensitivities, precisions and non-invasiveness not possible with classical schemes. A particularly exciting quantum sensor is the Nitrogen-Vacancy center (NV center) in diamond. It is sensitive to temperature variations [1–4], electric fields [5], pressure [6] and strain [7]. However, much attention has been given to the magnetic field sensing capabilities of the NV center [8–11] for the following reasons: First, the electronic spin associated with the NV center is coupled to magnetic fields, which allows for quantitative determination of magnetic fields over a broad frequency range from direct current (DC) up to GHz [12, 13]. Second, the NV center is a point-like sensor that enables measurements with nanoscale spatial resolution limited only by the NV sample distance. Third, the NV center operates at various magnetic fields from zero to a few Tesla [14, 15] and under a broad temperature range from mK to above room temperature [3]. Finally, the sensor assures minimal back-action and is mechanically robust.

In this thesis, we focus on questions in condensed matter physics, which explore the physical properties of matter on length scales that we can address with the NV center. Matter consists of a collection of atoms and its properties are influenced by the behavior of electrons thereof. Mobility of electrons is different in insulators, semiconductors and conductors. Spins associated with electrons and interactions among them can lead to magnetic ordering, while strong correlation of electrons can lead to pairing and condensation as in the case of superconductors. Understanding the role of

electrons is therefore a key ingredient to widen our understanding of such phenomena in condensed matter physics.

Magnetic fields generated by moving electrons or electron spins give us a handle to study electronic behavior and to learn and extract material properties. Consequently, various magnetic field sensors have been developed and have played pivotal roles in the understanding of condensed matter. Spin-based magnetometers like muon spectroscopy, neutron scattering or nuclear magnetic resonance feature atomic scale resolution but they are in reciprocal space or are ensemble-averaged measurements. On the other hand, magnetic force microscopy (MFM), magnetic resonance force microscopy (MRFM), scanning superconducting quantum interference devices (SQUIDS), scanning Hall-bars, and Lorentz transmission electron microscopy provide real-space imaging but they are invasive, only offer a limited field and temperature range, require thin and conducting material or lack spatial resolution. Therefore, there is a significant need for a quantitative, real-space magnetometer that is not invasive, works under a broad range of fields and temperatures and allows high spatial resolution and field sensitivity.

NV centers emerge as a potential platform to fill this gap. After proof-of-principle experiments of NV magnetometry [10, 11, 16] have shown the great potential, first applications of it to probe correlated-electron physics of magnets and to explore current distributions in low-dimensional materials have been reported: Imaging of static magnetic textures revealed spin configurations in domain walls [17], skyrmions [18], and non-collinear antiferromagnets [19]. AC magnetometry allowed researchers to probe nanometer-scale spin-waves [20], to determine spin chemical potential in a magnetic insulator [21], and to characterize the transport regime of electrons in metals [22, 23]. Finally, stray field imaging can be used to reproduce static current pattern as shown in graphene [24], nanowires [25], and integrated circuits [26]. Although all these experiments brought advances to the field of condensed matter, they were all performed at room temperature, while many phenomena and exotic electronic phases have critical temperatures well below and could not profit from the rapid developments in NV magnetometry.

## Scope of this thesis

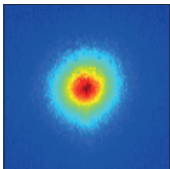
In this thesis, we report on the successful implementation of the first cryogenic, scanning NV magnetometer and its application to magnetic phenomena in superconductors and two-dimensional van der Waals material.



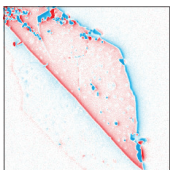
Chapter 2 starts off by describing the historical development of scanning NV magnetometry. It was launched with a proposal suggesting an atomic force microscope (AFM) functionalized with a single spin to detect magnetic stray fields on a nanometer scale, which was realized using the Nitrogen-Vacancy center at room temperature. We then list how we can initialize, manipulate and readout the spin of the NV center and introduce the magnetic field sensitivity along with the most common methods



to generate a two-dimensional field map. While we focus on measurements of DC magnetic fields throughout this thesis, we do this as a function of position, which allows for the mapping of the location and strength of the magnetic field source. To that end, we introduce a transformation in Fourier space, which we call *reverse propagation*, that yields the spin texture or planar current distribution in the sample given a stray field measurement in a plane above the sample. We walk the reader through the derivations, give useful hints for the computational implementation and provide MATLAB code for direct application. We end the chapter with the presentation of our cryogenic scanning NV setup, summarize its benefits and current challenges.



In order to benchmark our NV magnetometry system, we first applied it to well known magnetic phenomena in superconductors that were already imaged with other techniques. After setting the theoretical background, we show in Chap. 3 quantitative and high resolution images of the Meissner effect and vortices in a prototypical high-temperature superconductor. The close proximity of our sensor allows us for the first time to independently extract the London penetration depth and the sensor to sample distance and to discriminate between competing, microscopic models for supercurrent flow.



In Chap. 4 we dedicate our cryogenic magnetometer to a novel, two-dimensional magnetic material. Van der Waals heterostructures with intrinsic magnetic ordering were only discovered in 2017 and may enable fundamental discoveries and novel technologies. The magnetic properties of these materials have so far only been probed qualitatively or in an ensemble-averaged way. While the bulk version of the two-dimensional magnet exhibits ferromagnetic ordering, few-layer stacks of them show different magnetic ordering – an effect that could not be explained experimentally. The quantitative nature of the NV center provides further insight and we unambiguously prove a direct connection between the magnetic and the structural ordering. In particular, we are able to prepare the two-dimensional magnet into its magnetic ground state with ferromagnetic ordering, a state that has not been observed until now. In addition, we show magnetization maps of thus far undiscovered magnetic domains that feature ferromagnetic as well as antiferromagnetic interlayer coupling within the same stack.

In the final Chap. 5 we summarize our findings and highlight further routes that can be taken using the instrument developed here. By virtue of reverse propagation, we can directly image current flows, which is especially suitable for two-dimensional materials like graphene. We present potential interesting areas, which will profit from measurements of the spatial dependence of currents. Further, we advocate the use of the full potential of NV center and harness the high-frequency sensing capabilities. With that, one could address magnetic excitations such as spin-waves, which are generally hard to detect but offer fruitful insight into spin interactions. If successful, these experiments will render the NV center a novel and indispensable tool in the emerging field of magnonics.



## 2. Cryogenic magnetometry with a single spin in diamond

Advancing the frontiers of nanoscience and information technology hinges on the availability of novel tools for nanoscale magnetic field sensing and imaging. The approaches that offer the highest spatial resolution are mostly based on scanning probe microscopes, including magnetic force microscopy (MFM) [27], magnetic resonance force microscopy (MRFM) [28], and more recently superconducting quantum interference devices (nanoSQUIDs) [29], and Hall-bars [30]. In 2005, Chernobrod and Berman [31] proposed another approach to nanoscale magnetic field sensing based on optically detected magnetic resonance (ODMR). Their general layout is presented in Fig. 2.1. The setup is equipped with a permanent magnet and a radio-frequency coil that allows for the addressing of magnetic sublevels of an unspecified photoluminescent center. They envisioned to produce nanoscale magnetic field images by scanning a highly sensitive atomic force microscope (AFM) tip that is functionalized with a photoluminescent center over a magnetic sample.

An impressive implementation of the proposal was demonstrated in 2008 by Balasubramanian *et al.* [8] at room temperature. They attached a diamond nanocrystal containing a single electronic spin of the Nitrogen-Vacancy (NV) color center to the tip of an atomic force microscope. While scanning the NV center in close proximity to a magnetic material, they evaluated local magnetic fields by monitoring the Zeeman

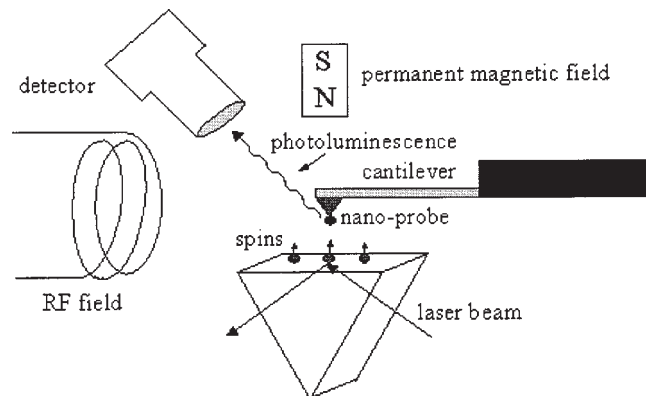


**Figure 2.1.:** A schematic view of an ODMR-based scanning microscope.

A photoluminescent center attached to the apex of an AFM tip is scanned over a sample and produces nanoscale resolution magnetic field images by virtue of optically detected magnetic resonance (ODMR). The figure is adapted with permission from [31], AIP Publishing.

shift of the magnetic sublevels of the NV center through ODMR. Although successful, NV centers in diamond nanocrystals suffer from short spin coherence times and inefficient far-field collection of the fluorescence. In 2012, Maletinsky *et al.* [16] addressed these issues and presented a robust, monolithic diamond cantilever used as the tip of an AFM. Both implementations enabled a wide range of research from the imaging of a single electronic spin [32] to imaging of domain-wall hopping [33], nanoscale microwave currents [34], antiferromagnetic order [19, 35] and direct measurement of interfacial Dzyaloshinskii-Moriya interaction [36].

In this chapter we show the next step in scanning NV magnetometry. We succeeded to bring this powerful imaging tool to low temperatures, opening up the possibility to look at the wealth of physical phenomena that require cryogenic conditions. In Sec. 2.1 we introduce the NV center, its spin and optical properties, and its response to external magnetic fields. In Sec. 2.1.5 and 2.1.4 we present the main imaging methods used throughout this thesis, namely iso-magnetic (ISO) field and full field imaging. In Sec. 2.2 we present a mathematical method that allows us to retrieve the nature of the two-dimensional source of the magnetic fields imaged with the NV center. Finally, in Sec. 2.3 we present the novel cryogenic scanning NV setup.

## 2.1. NV center physics and magnetic imaging

A key challenge in Chernobrod's and Berman's proposal was to find an appropriate photoluminescent center that is sensitive to magnetic fields. In the year 2008, multiple research groups [8–11] looked into the magnetic sensing properties of a defect center

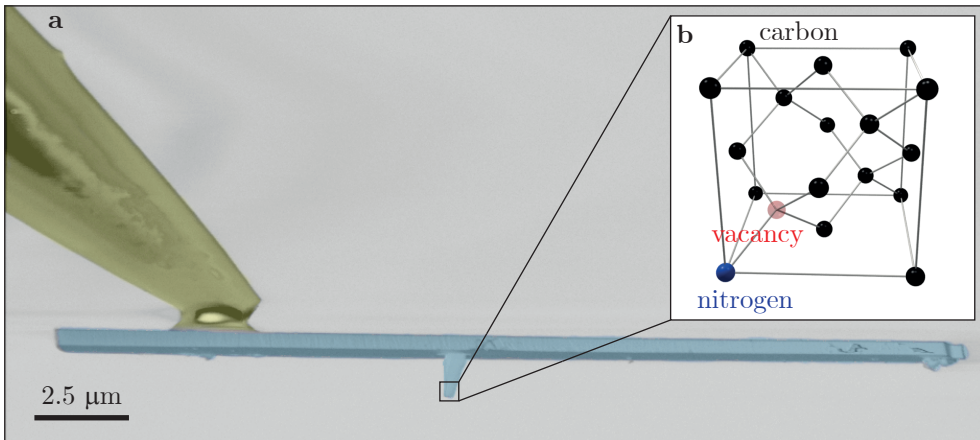


**Figure 2.2.: All-diamond cantilever with embedded NV center.** **a** False-color electron microscope image of an all-diamond scanning probe. The NV sensor spin is located at the apex of the nanopillar visible in the center of the diamond cantilever (blue). The device is glued via a quartz rod (golden) to a tuning fork (not shown). The fabrication and mounting of the sensor is published in [37]. **b** The NV center is a lattice defect in diamond with a substitutional Nitrogen (blue) and a neighboring vacancy (red). The NV-axis passes through both the Nitrogen and vacancy.

in diamond and identified this defect as a near-ideal candidate for Chernobrod's and Berman's approach. The NV center<sup>1</sup> in diamond is a lattice defect and consists of a substitutional nitrogen atom and a neighboring lattice vacancy as depicted in Fig. 2.2b. A combination of exceptional spin and optical properties make the NV center a very sensitive magnetometer that can be initialized and read out by purely optical means, and coherently manipulated with microwave magnetic fields.

After the identification of a suitable photoluminescent center, the tip of the AFM has to be functionalized with the magnetometer. To that end, Maletinsky *et al.* [16] fabricated all-diamond cantilevers (see Fig. 2.2a) with a single NV center placed at the end of a nano-pillar, which can be raster scanned over a magnetic sample as suggested by Fig. 2.1. Such probes are highly robust and allow for extended measurement times of up to several months. The diamond pillars that constitute the scanning probe act as optical waveguides that render optical excitation and readout of NV centers highly efficient. The fabrication process is elaborate and highly sophisticated and was published in [37]. We reviewed this process and implemented further improvements, which can be found in Appendix A.1.1.

### 2.1.1. Electronic structure and optical properties

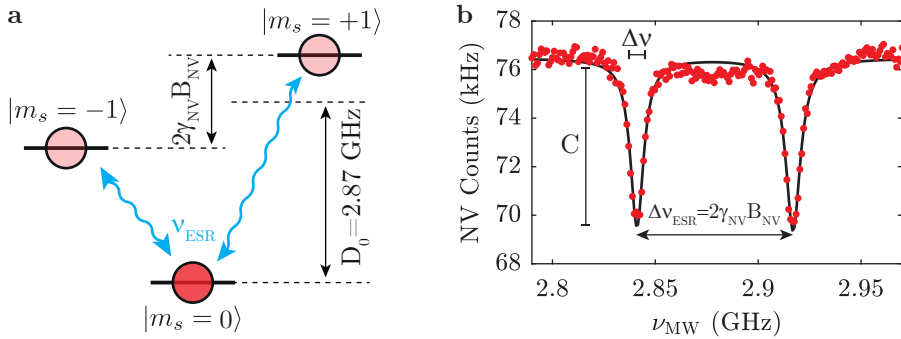


**Figure 2.3.: Electronic structure of the NV  $S=1$  ground state and electron spin resonance.** **a** Ground-state spin levels of the negatively charged NV center in diamond, which exhibit spin-dependent fluorescence rates (red circles) and optical spin pumping under green excitation. The  $|m_s = \pm 1\rangle$  sublevels are separated by the zero-field splitting  $D_0 = 2.87$  GHz from the  $|m_s = 0\rangle$  sublevel. The degeneracy of the  $|m_s = \pm 1\rangle$  magnetic sublevels is lifted by magnetic fields along the NV-axis. Microwave magnetic fields of frequency  $\nu_{\text{ESR}}$  drive electron spin resonance (ESR), which is optically detectable. **b** Typical NV ODMR trace obtained from a single NV in a diamond scanning probe at 4.2 K. Fluorescence count rate, ODMR contrast and linewidth yield a magnetic field sensitivity of  $7.5 \mu\text{T}/\sqrt{\text{Hz}}$ . The data is fitted with the sum of two Lorentzians.  $C$  ( $\Delta\nu$ ) illustrates the contrast (linewidth), respectively.

<sup>1</sup>The NV center predominantly occurs in two charge states, namely the neutral  $\text{NV}^0$  state and the negatively charged  $\text{NV}^-$  state. Only  $\text{NV}^-$  has optical and spin properties that are interesting for magnetometry and therefore we will neglect the neutral charge state and refer to the negative charge state as the NV center.

This section covers the electronic structure and optical properties of the NV center. Due to the numerous excellent descriptions of the NV center, we restrict ourselves to the key features relevant to this thesis. For more in-depth illustrations of the NV center physics, we refer the reader to [38, 39].

The negatively charged NV center possesses six electrons, which form an effective  $S=1$  spin triplet state in the ground state with magnetic sublevels  $|m_s = 0, \pm 1\rangle$  as illustrated in Fig. 2.3a. The  $|m_s = \pm 1\rangle$  sublevels are split in energy from the  $|m_s = 0\rangle$  sublevel due to spin-spin interaction by the zero-field splitting  $D_0 = 2.87$  GHz. As we will see in more detail in Sec. 2.1.3, application of a magnetic field  $B_{NV}$  along the NV-axis introduces a Zeeman shift of the  $|m_s = \pm 1\rangle$  sublevels of

$$\Delta\nu_{\text{ESR}} = 2\gamma_{NV}B_{NV}, \quad (2.1)$$

where  $\gamma_{NV} = 28$  MHz/mT is the NV gyromagnetic ratio and the NV-axis passes through both the Nitrogen and vacancy.

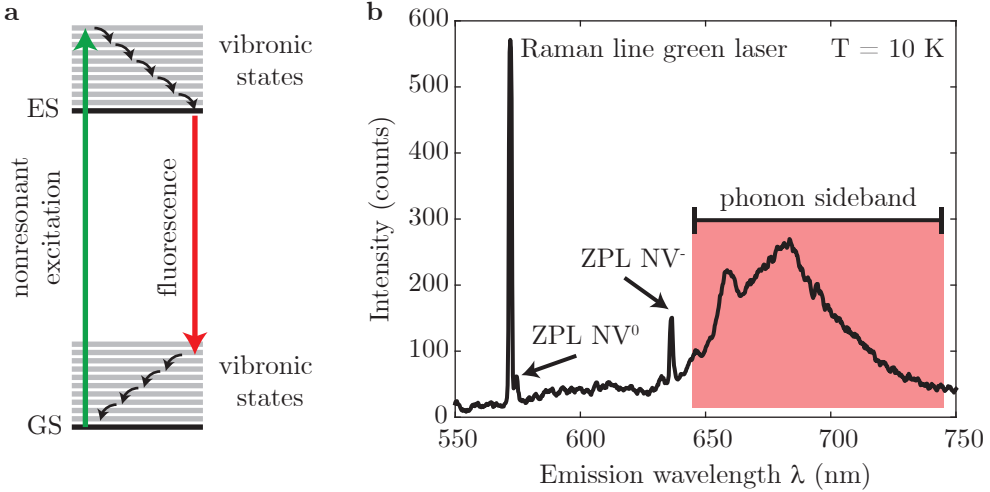


**Figure 2.4.: NV emission under nonresonant excitation.** **a** When exciting the NV center non-resonantly, for example with green light, the system is pumped into vibronic states of the  $S=1$  excited state (ES) and then experiences a radiationless, phonon-mediated decay into the electronic levels. The electronic levels have a radiative lifetime of few tens of ns, after which the system relaxes back into the  $S=1$  ground state (GS). This can either happen in conjunction with the creation of a phonon via the ground state vibronic states or directly without phononic contributions. The first process gives rise to emission into the phonon sideband, while the direct recombination causes emission into the zero-phonon line. **b** Typical NV emission spectrum recorded at 10 K. The zero-phonon line (ZPL) of the negatively charged NV center is located at 637 nm and the phonon sideband extends from the zero-phonon line to about 750 nm. We also observe the ZPL of the neutral NV charge state as well as the Raman line of the green excitation laser. This figure is adapted with permission from [38].

The spin state of the NV center can be optically initialized and read out. To that end, the NV center is optically excited from its ground to its excited state. Nonresonant excitation with green light ( $\lambda = 532$  nm) excites the NV center into a continuum of vibronic states as illustrated in Fig. 2.4a. After fast, phonon-mediated relaxation into the electronic excited state, the NV center relaxes back to its ground state upon the emission of a red photon into the zero-phonon line ( $\lambda = 637$  nm) or the phonon sideband ( $\lambda = 637 - 750$  nm) (see Fig. 2.4b). The excited state lifetime is  $\approx 10$  ns [40]. While all transitions discussed thus far are spin conserving, intersystem crossings [41–43] into a long-lived singlet state (not shown) are not and lead to two key features of the NV center, namely spin-dependent fluorescence and optical initialization. Spin population in the excited state can shelve into the singlet state, which is more likely for the  $|m_s = \pm 1\rangle$  sublevels. There, the NV center is trapped for a few 100 ns [40], before a final radiationless transition brings it back to the  $|m_s = 0\rangle$  or  $|m_s = \pm 1\rangle$  ground state with equal probability [43]. As the relaxation to the ground state via the singlet state is radiationless and more likely to happen for the  $|m_s = \pm 1\rangle$  sublevels, the NV appears darker when being in the  $|m_s = \pm 1\rangle$  sublevels. This is indicated in Fig. 2.3 by the bright and dark circle of the  $|m_s = 0\rangle$  and  $|m_s = \pm 1\rangle$  sublevels, respectively. As the shelving rate into the singlet state is higher for the  $|m_s = \pm 1\rangle$  magnetic sublevels, a continuous optical excitation will eventually lead to the accumulation of population in the  $|m_s = 0\rangle$  spin sublevel, and hence, a spin initialization of roughly 80% into the  $|m_s = 0\rangle$  spin state [42].

### 2.1.2. Optically detected magnetic resonance

Spin dependent fluorescence and optical initialization allows us to map out the relative position of the  $|m_s = \pm 1\rangle$  sublevels with respect to the  $|m_s = 0\rangle$  sublevel. To that end, we continuously excite the NV center with green light, thereby initializing it into its bright  $|m_s = 0\rangle$  sublevel while recording the fluorescence. In addition, we apply a microwave field (MW) and sweep its frequency  $\nu_{\text{MW}}$ . When  $\nu_{\text{MW}}$  is resonant with the transition frequency  $|m_s = 0\rangle \leftrightarrow |m_s = -1\rangle$  or  $|m_s = 0\rangle \leftrightarrow |m_s = +1\rangle$  ( $\nu_{\text{MW}} = \nu_{\text{ESR}}$ ), NV population is transferred to the darker  $|m_s = \pm 1\rangle$  state, which results in a dip in fluorescence. The position of the dip in frequency space corresponds to the relative energy difference between  $|m_s = 0\rangle$  and  $|m_s = \pm 1\rangle$  and the distance in frequency between the dips is proportional to the applied magnetic field along the NV-axis. This measurement is called optically detected magnetic resonance (ODMR). A typical data set is shown in Fig. 2.3b.

The magnetic field sensitivity  $\eta$  indicates the minimum detectable field variation  $\delta B$  in a given measurement time  $\Delta t$

$$\eta = \delta B \sqrt{\Delta t}. \quad (2.2)$$

In the case of ODMR, the change in fluorescence caused by a change in magnetic field is  $\frac{\partial I_0}{\partial B} \delta B \Delta t$ , where  $I_0$  is the NV fluorescence rate. At the point of highest sensitivity it is given by the maximal slope of the ODMR dip. The noise during the readout is dominated by photon shot-noise  $\sqrt{I_0 \Delta t}$ . A common but arbitrary choice to define the field sensitivity is a signal to noise ratio of 1

$$\frac{\text{signal}}{\text{noise}} = 1 = \frac{\frac{\partial I_0}{\partial B} \delta B \Delta t}{\sqrt{I_0 \Delta t}} = \frac{\frac{\partial I_0}{\partial B} \delta B \sqrt{\Delta t}}{\sqrt{I_0}}. \quad (2.3)$$

We can evaluate  $\frac{\partial I_0}{\partial B}$  at the highest slope, combine Eq. (2.2) and Eq. (2.3), and obtain the field sensitivity

$$\eta = \frac{\sqrt{I_0}}{\left. \frac{\partial I_0}{\partial B} \right|_{\max}} \approx \frac{\Delta\nu}{C\sqrt{I_0}}, \quad (2.4)$$

where  $\Delta\nu$  and  $C$  are as defined in Fig. 2.3b. The magnetic field sensitivity can be improved by either reducing the linewidth or increasing the contrast or the count rate. The ODMR contrast is fixed by the NV photophysical properties, i.e. the branching ratio into the singlet state, and cannot be improved. The ODMR linewidth is fundamentally limited by the dephasing time  $T_2^*$ . However, in most cases this limit is not reached as the readout laser and the microwave fields induce power broadening [44]. In order to increase the collected fluorescence and thereby improve the sensitivity, we embed the NV centers in the apex of an all-diamond probe tip (see Fig. 2.1), which acts as an effective waveguide [45]. As the measured magnetic fields from superconductors (see Chap. 3) and 2D magnets (see Chap. 4) did not approach our sensitivity limits, ODMR measurements were taken at moderate laser (40 to 200  $\mu$ W) and microwave powers (−5 to −10 dBm at the insert of the cryostat) leading to power broadening of the ODMR spectra. A typical magnetic field sensitivity for the data set in Fig. 2.3b is 7.5  $\mu$ T/ $\sqrt{\text{Hz}}$  – sufficient to detect a current of 400 nA flowing in a one-dimensional channel at a distance of 10 nm from the NV center.

Measurements we performed on current flow in graphene within this thesis (see Sec. 5.2), were on the edge of our sensitivity. Therefore, we lowered the laser and microwave power to reduce the linewidth, which reveals the structure resulting from the hyperfine interaction between the electronic spin and the  $I = 1$  nuclear spin of the  $^{14}\text{N}$

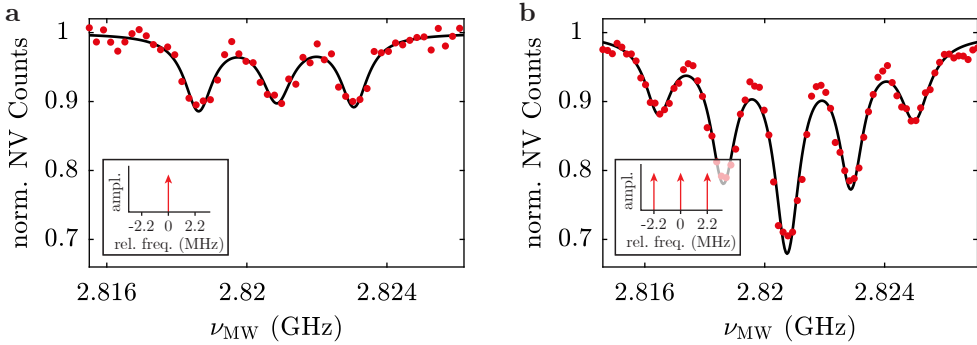


**Figure 2.5.: Hyperfine resolved electron spin resonance of the  $|m_s = 0\rangle \leftrightarrow |m_s = -1\rangle$  transition.** **a** In order to increase the ODMR sensitivity, laser and microwave power needs to be reduced to avoid power broadening of the linewidth. This reveals the underlying  $^{14}\text{N}$  hyperfine structure. The dips correspond to nuclear spin quantum number  $m_I = \{+1, 0, -1\}$  and are separated by 2.2 MHz. The sensitivity in this case is 2.4  $\mu\text{T}/\sqrt{\text{Hz}}$ . The inset shows the amplitude of the microwave tone. There is only one microwave tone, which is swept over the  $|m_s = 0\rangle \leftrightarrow |m_s = -1\rangle$  transition. **b** Same ODMR transitions as in **a** but driven with three microwave tones separated by the hyperfine splitting (inset). The ODMR contrast of the center peak is increased by a factor of three leading to an improved sensitivity of 0.5  $\mu\text{T}/\sqrt{\text{Hz}}$ .



that comprises the NV center. The ODMR spectrum of the  $|m_s = 0\rangle \leftrightarrow |m_s = -1\rangle$  transition features then not only one, but three dips separated by 2.2 MHz [39] (see Fig.2.5a). The sensitivity is improved to  $2.4 \mu\text{T}/\sqrt{\text{Hz}}$ . Unfortunately, the desired reduction in linewidth comes at the cost of reduced fluorescence rate (due to reduced laser power) and a factor three reduction in ODMR contrast as the NV population is now distributed over three spin levels. The latter can be mitigated by driving not only one resonance at a time (see Fig.2.5a inset) but all three resonances (see Fig.2.5b inset). This results in a sensitivity of  $0.5 \mu\text{T}/\sqrt{\text{Hz}}$ . This is the best value measured for this setup and in principle would allow for the detection of a 30 nA current under the same conditions.

### 2.1.3. Response to DC magnetic fields

In Sec.2.1.1 we have already seen that the ESR resonance frequencies are linearly dependent on magnetic field along the NV-axis. In this section we deepen the discussion on the NV's response to DC magnetic fields<sup>2</sup>. The Hamiltonian for the NV's electronic spin in the ground state reads

$$\hat{H}/h = D_0 \hat{S}_z^2 + E(\hat{S}_x^2 - \hat{S}_y^2) + \gamma_{\text{NV}} \mathbf{B} \hat{\mathbf{S}}, \quad (2.5)$$

where  $D_0$  is the zero field splitting, which splits the  $|m_s = \pm 1\rangle$  sublevels from the  $|m_s = 0\rangle$  sublevel by 2.87 GHz.  $E$  is the off-axis zero-field splitting parameter and results from strain in the diamond, which leads to a mixing of the  $m_s$  sublevels thereby creating new eigenstate which are split by  $E$ . Since  $E$  is in general small ( $< 100$  kHz) for CVD-grown<sup>3</sup> samples and we typically apply bias fields  $B_{\text{bias}} \gg hE/g\mu_B$ ,  $E$  can be neglected.  $B_{x,y,z}$  denote the magnetic field amplitudes defined in the NV coordinate system, with the  $z$ -axis being the NV symmetry axis and spin quantization axis, and  $\hat{\mathbf{S}}_{x,y,z}$  are the  $S=1$  spin operators. We can expressing the spin operators in the Zeeman basis as

$$\hat{S}_x = \frac{1}{\sqrt{2}} \begin{pmatrix} 0 & 1 & 0 \\ 1 & 0 & 1 \\ 0 & 1 & 0 \end{pmatrix} \quad \hat{S}_y = \frac{-i}{\sqrt{2}} \begin{pmatrix} 0 & 1 & 0 \\ -1 & 0 & 1 \\ 0 & -1 & 0 \end{pmatrix} \quad \hat{S}_z = \begin{pmatrix} 1 & 0 & 0 \\ 0 & 0 & 0 \\ 0 & 0 & -1 \end{pmatrix}, \quad (2.6)$$

and insert them into Eq. (2.5) to obtain

$$\hat{H}/h = \begin{pmatrix} D_0 + \gamma_{\text{NV}} B_z & \frac{\gamma_{\text{NV}}}{\sqrt{2}} (B_x - iB_y) & 0 \\ \frac{\gamma_{\text{NV}}}{\sqrt{2}} (B_x + iB_y) & 0 & \frac{\gamma_{\text{NV}}}{\sqrt{2}} (B_x - iB_y) \\ 0 & \frac{\gamma_{\text{NV}}}{\sqrt{2}} (B_x + iB_y) & D_0 - \gamma_{\text{NV}} B_z \end{pmatrix}, \quad (2.7)$$

In the case of parallel magnetic fields ( $B_x = B_y = 0$ ), the ESR frequencies shift linearly and the Zeeman splitting of the ODMR resonance dips is given by Eq. (2.1). This scenario is depicted in Fig. 2.6a and b. Transverse magnetic fields cause a quadratic shift of the resonance frequency (see Fig. 2.6c and d). Moreover, transverse fields lead to a mixing of the spin states and  $|m_s = 0, \pm 1\rangle$  are no longer good eigenstates.

<sup>2</sup>As the experiments conducted in this thesis involved only DC magnetic field sensing, we limit the discussion to DC magnetometry and refer the reader to [13, 46, 47] for AC magnetometry.

<sup>3</sup>chemical vapor deposition

This also has implications for the photophysical properties of the NV center. Optical spin polarization becomes inefficient, ODMR contrast decreases as well as the overall fluorescence rate of the NV center, which renders quantitative magnetic field sensing impossible for  $B_{\perp} > 10$  mT, but enables qualitative, all-optical sensing [48]. However, in this thesis the transient fields were well below 10 mT.

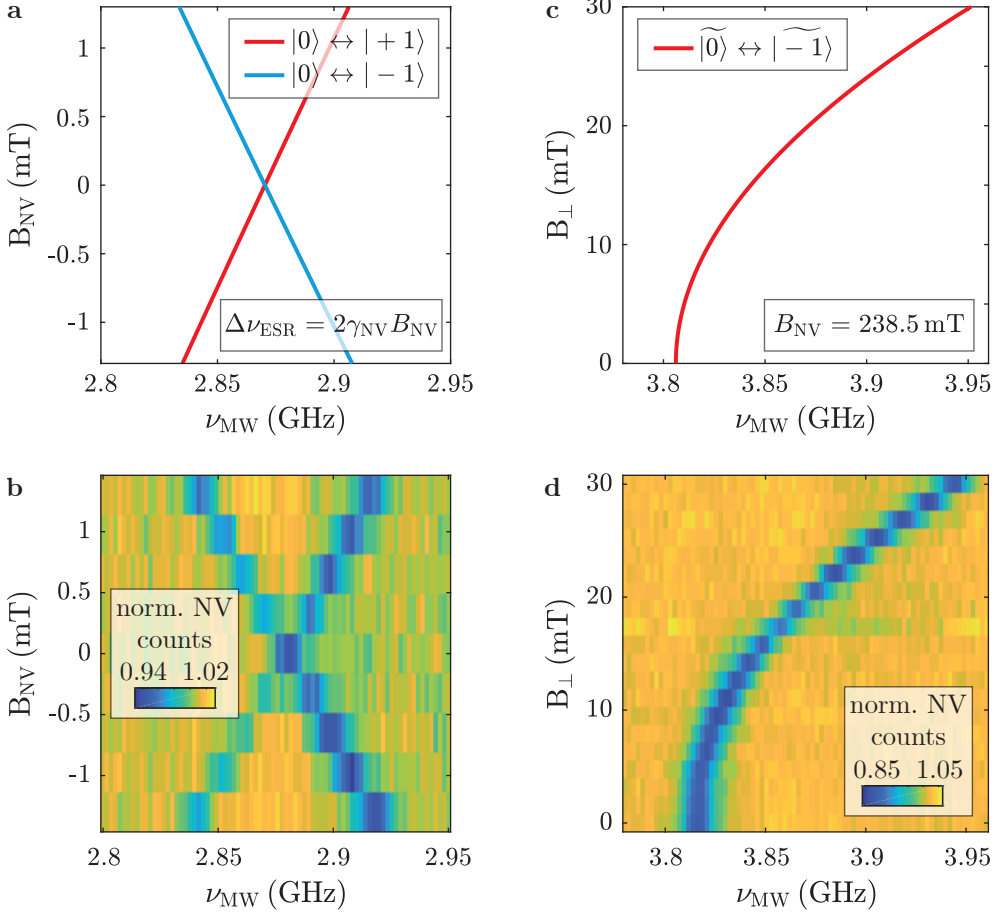


**Figure 2.6.: The NV S=1 ground state response to static external fields.** **a** Longitudinal DC magnetic fields introduce a Zeeman splitting  $\Delta\nu_{\text{ESR}}$  between the  $m_s = \pm 1$  spin sublevels. **b** Experimentally recorded ODMR traces as a function of parallel magnetic field over the same field range as **a** in zero bias field. **c** Transverse DC magnetic fields  $B_{\perp} = \sqrt{B_x^2 + B_y^2}$  mix and split the spin sublevels. This effect is small and can usually be neglected in our experiments for  $B_{\perp} \ll B_{\text{NV}}$ . **d** ODMR traces as a function of perpendicular magnetic field over the same field range as **c** in a bias field of  $B_{\text{NV}} = 238.5$  mT.

### 2.1.4. Full field imaging

The NV center is a highly sensitive magnetometer that detects the magnetic field locally at its position. To obtain stray field information at more than one position, i.e. a 2D field image, large ensembles of NVs can be employed, which are simultaneously interrogated with a CCD camera. The advantage of so-called wide-field magnetometry [49] is a rather simple setup paired with a magnetic field sensitivity that increases with  $1/\sqrt{N}$  where  $N$  is the number of NV centers within the detection volume. Nevertheless, a key motivation for the approach presented by Chernobrod and Berman is a high spatial resolution. In the case of ensemble magnetometry, the spatial resolution is limited by optical diffraction ( $\sim 500$  nm). On the other hand, the spatial extent of the electronic wavefunction of a single NV center is well below 1 nm, allowing in principle for sub-nanometer resolution. A 2D magnetic field image can therefore be generated by scanning a single NV center relative to a magnetic sample and measuring the magnetic field at every position. In such a scan either the full field information or only the location of one field contour can be recorded. These two imaging methods, namely full field imaging and iso-field imaging, are described in the following.

A full field image generates a map with the full quantitative information of the field strength at each pixel. In practice, we scan the NV center and record an ODMR spectrum at every pixel. From the position of the ESR resonance ( $\nu_{\text{ESR}}$ ), we deduce the magnetic field strength projected onto the NV-axis. Figure 2.7a shows a simulated stray field map of  $B_{\text{NV}}$  at the scan height of the NV center. Scanning the NV center over this field distribution in an arbitrarily chosen bias field of  $B_{\text{bias}} = 20$  mT would produce the resonance frequency map depicted in Fig. 2.7b. Given this data,  $B_{\text{NV}}$  can be recovered with

$$B_{\text{NV}} = \frac{D_0 \pm \nu_{\text{ESR}}}{\gamma_{\text{NV}}} - B_{\text{bias}}, \quad (2.8)$$

For illustrative purposes, three ODMR scans at the pixels indicated in **b** are shown in **c**. Since a full ODMR trace needs to be recorded at every pixel, these scans are slow and time-consuming. A speed-up is offered by frequency-locking methods as discussed in [50, 51]. There the MW signal is locked to the ESR resonance in real time using a feedback loop. While this measurement scheme is fast, as soon as the feedback loop loses track of the resonance, erroneous signal is collected.

### 2.1.5. Iso-field imaging

A more robust, but comparably fast method to acquire an overview of the magnetic signal originating from a sample is iso-magnetic (iso) field imaging, in which contours of fixed values  $B_{\text{NV}} = B_{\text{iso}}$  are measured. To that end, the microwave frequency is fixed at  $\nu_{\text{MW}} = \gamma_{\text{NV}}(B_{\text{bias}} + B_{\text{iso}})$ , where  $\gamma_{\text{NV}}B_{\text{bias}}$  corresponds to the NV-ESR frequency in absence of any magnetic sample. The sample is then scanned below the NV center while NV fluorescence is constantly interrogated. Whenever the sample stray field at the position of the NV corresponds to  $B_{\text{iso}}$ , a decrease in fluorescence is observed, leading to magnetic contrast in the iso-field image. Since these field maps do not provide full field information, they are often not straightforward to interpret. However, iso-field imaging is still frequently used for large overview scans as it produced magnetic contrast images in a very short time compared to full field

imaging.

Figure 2.7d shows a 0 mT iso-field image simulated for the stray field map of Fig. 2.7a with  $B_{\text{iso}} = 0$  mT and  $\nu_{\text{MW}} = \gamma_{\text{NV}} B_{\text{bias}}$  (dashed black line in c). Dark features correspond to magnetic fields in the range of  $B_{\text{iso}} \pm \Delta\nu/\gamma_{\text{NV}}$ , where  $\Delta\nu$  is the linewidth of the ODMR resonance. The pixel color of the iso-field map corresponds to the NV counts of the intersection of the corresponding ODMR trace with the dashed line in Fig. 2.7c. In practice, we record not only the NV fluorescence counts at  $\nu_{\text{MW}}$ , but also the counts with the MW tone off. This second data set serves as a normalization reference.

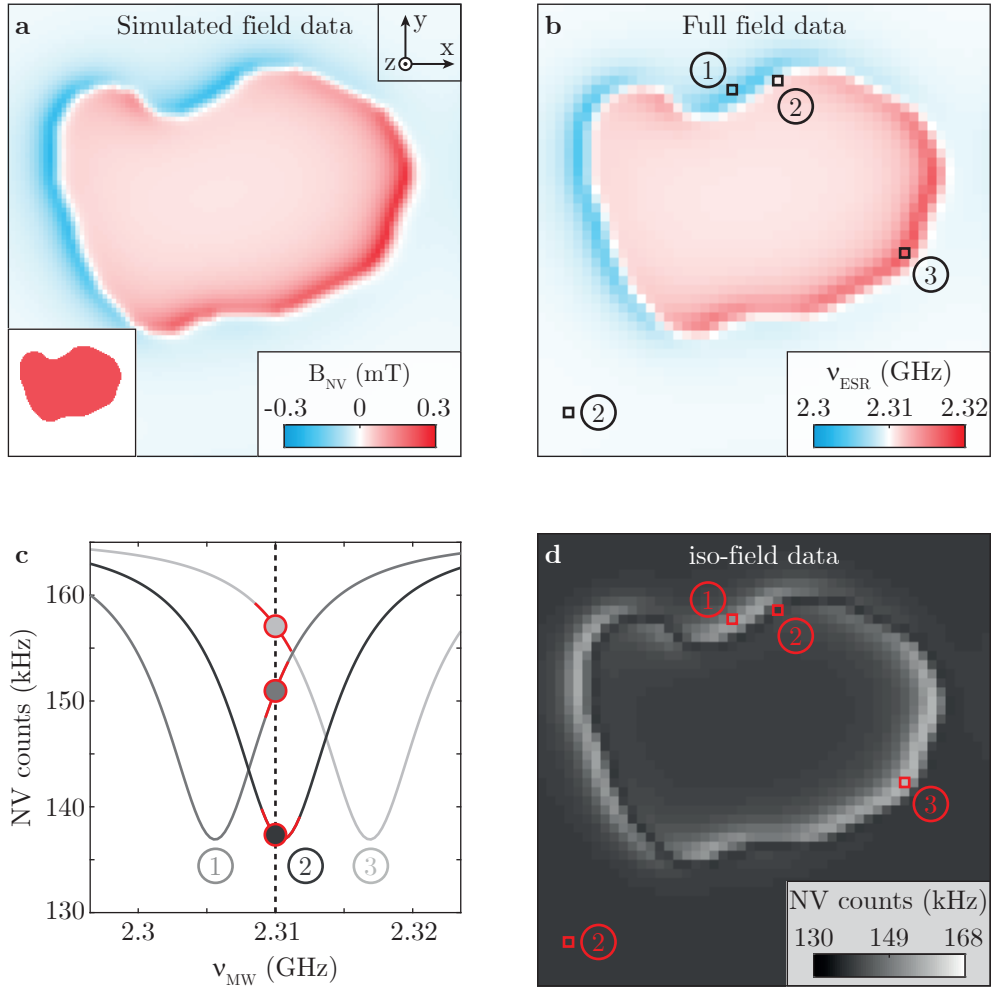


**Figure 2.7.: Principle of full field and iso-field imaging.** **a** Simulated magnetic stray field projection onto the NV axis. The field originates from a uniform out-of-plane magnetized domain (see inset, surface magnetization  $\sigma = 130 \mu A$ ). **b** Simulated full field scan corresponding to **a**. Every pixel value corresponds to the local ESR resonance frequency. Converting the resonance frequency into magnetic field using Eq. (2.8) yields the data set in **a**. **c** Simulated ODMR spectra at three selected positions indicated in **b** and **d**. In the case of the iso-field scan in **d**, the microwave frequency is fixed at  $\nu_{MW} = 2.31$  GHz (dashed black vertical line) yielding the NV counts indicated with red circles for each ODMR trace. The color code for the traces is chosen according to the colorbar in **d** and corresponds to the pixel color of the highlighted pixels in **d**. **d** Iso-field scan of **a** for a fixed microwave frequency at  $\nu_{MW} = 2.31$  GHz. The data set is obtained by mapping the resonance frequency in **b** to NV fluorescence counts using the known ODMR response.

## 2.2. Reverse Propagation

NV based measurements can generate two-dimensional magnetic stray field maps recorded at a given height above the sample. If one is able to write down analytical solutions of the stray field generated by the source, one can fit these field maps and deduce interesting quantities about the system. However, exact knowledge about the system is usually not granted and therefore one cannot fit the recorded stray fields. In these cases, it is a priori difficult to extract useful information out of the measurement data. One very powerful technique that addresses this issue is *reverse propagation*. This technique can be used to reconstruct the magnetic source at  $z = 0$  (for a definition of the coordinate system see Fig. 2.8a) from stray field maps  $\mathbf{B}(x, y)$  (see Fig. 2.8b) at  $z = z_{\text{NV}}$ . The source can either be a 2D spin texture  $\mathbf{M}(x, y)$  (see Fig. 2.8d, left map) or a planar current distribution  $\mathbf{J}(x, y)$  (see Fig. 2.8d, right map). The reverse propagation then combines a continuation along the  $z$ -axis from the height of the field map ( $z = z_{\text{NV}}$ ) to the height of the source ( $z = 0$ ) as well as transformation from  $\mathbf{B}(x, y)$  to either  $\mathbf{M}(x, y)$  or  $\mathbf{J}(x, y)$ . In addition, reverse propagation allows also to infer all other magnetic field components from the measurement of one field component, for instance to infer  $B_z(x, y)$  from  $B_{\text{NV}}(x, y)$  (see Fig. 2.8b).

In the following sections we present detailed derivations of the continuation and transformations, while remarks concerning the practical implementation and general considerations of potential error sources of the technique are discussed in Appendix A.1.4. Reverse propagation is a technique in Fourier space and therefore we will throughout the chapter use the notation of capital letters for real space ( $\mathbf{B}(\mathbf{r})$ ,  $\mathbf{M}(\mathbf{r})$ ,  $\mathbf{J}(\mathbf{r})$ ) and lowercase letters for Fourier space ( $\mathbf{b}(\mathbf{k})$ ,  $\mathbf{m}(\mathbf{k})$ ,  $\mathbf{j}(\mathbf{k})$ ). The position vector in real space is  $\mathbf{r} = (x, y, z)$ , the horizontal wave vector is  $\mathbf{k} = (k_x, k_y)$  and the magnitude of the  $k$ -vector is  $k = \sqrt{k_x^2 + k_y^2}$ . The recorded magnetic field map  $B_{\text{NV}}(x, y)$ , which we aim to transform, is assumed to be a projection onto the NV axis ( $n_x, n_y, n_z$ ) with

$$\begin{aligned} n_x &= \cos(\phi_{\text{NV}}) \cdot \sin(\theta_{\text{NV}}) \\ n_y &= \sin(\phi_{\text{NV}}) \cdot \sin(\theta_{\text{NV}}) \\ n_z &= \cos(\theta_{\text{NV}}), \end{aligned} \tag{2.9}$$

where  $\phi_{\text{NV}}$  is the azimuthal and  $\theta_{\text{NV}}$  the polar angle of the NV axis (see Fig. 2.8a).

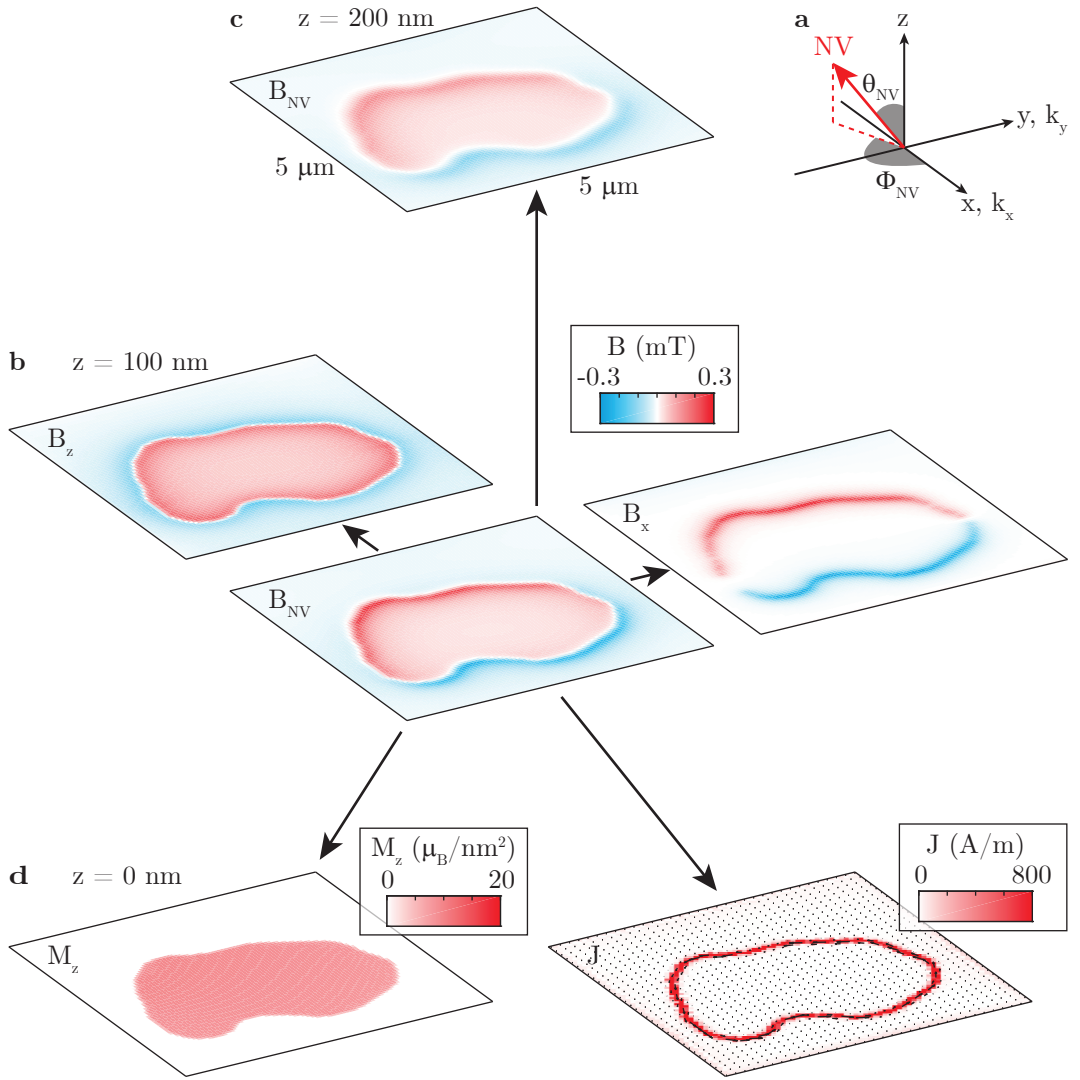


**Figure 2.8.: Illustration of reverse propagation** **a** Definition of the coordinate system with the NV axis (red arrow) given by  $(\phi_{NV}, \theta_{NV})$  in real space  $(x, y, z)$ .  $(k_x, k_y)$  are the horizontal wave vectors. **b** Simulated NV stray field map  $B_{NV}$  (center map) at  $z = 100$  nm.  $B_{NV}$  is transformed to infer the magnetic field along the  $z$ -axis ( $B_z$ , left map) and  $x$ -axis ( $B_x$ , right map) at the same height. The colorbar applies to **b** and **c**. **c**  $B_{NV}$  continued to a height  $z = 200$  nm, which led to smoothing of the image. **d** Reverse propagation of  $B_{NV}$  in **b** yields the magnetic field source at  $z = 0$  nm. In the depicted case, the magnetic field is propagated to a homogeneous out-of-plane magnetization  $M_z$  (left panel) and a 2D current distribution  $J$ .

### 2.2.1. Upward and downward continuation

The NV center images stray magnetic fields at a fixed height  $z = z_{\text{NV}}$  above the field source located at  $z = 0$ . A necessary operation to reveal the nature of the source is to propagate the magnetic field down to the  $z = 0$  plane, where in a subsequent step the magnetic field can be converted to a magnetization or current distribution. This propagation is well known among geophysicists and is used to propagate aeromagnetic data away from or towards the earth surface [52], as both transformations are allowed. Although the transformations do not directly yield the source distributions of the measured stray fields, they provide helpful insights to get a general understanding. We consider the magnetic potential  $\Phi(\mathbf{r})$  with

$$\mathbf{B}(\mathbf{r}) = -\nabla\Phi(\mathbf{r}) \quad (2.10)$$

and the Laplace equation in a source-free region

$$\Delta\Phi = 0. \quad (2.11)$$

We can use the derivative property of the Fourier transform

$$\text{FFT} \left[ \frac{\partial}{\partial x} \Phi(x, y, z) \right] = ik_x \text{FFT} [\Phi(x, y, z)] \quad (2.12)$$

and rewrite the 2D Fourier transform along  $x$  and  $y$  of Eq. (2.11) as

$$\text{FFT} \left[ \left( \frac{\partial^2}{\partial x^2} + \frac{\partial^2}{\partial y^2} + \frac{\partial^2}{\partial z^2} \right) \Phi(x, y, z) \right] = \left( -k_x^2 - k_y^2 + \frac{\partial^2}{\partial z^2} \right) \hat{\Phi}(k_x, k_y, z) = 0. \quad (2.13)$$

It follows that

$$\frac{\partial^2}{\partial z^2} \hat{\Phi}(k_x, k_y, z) = (k_x^2 + k_y^2) \hat{\Phi}(k_x, k_y, z) = k^2 \hat{\Phi}(k_x, k_y, z). \quad (2.14)$$

We can make an Ansatz for the  $z$ -dependency of  $\hat{\Phi}(k_x, k_y, z)$  and write the potential as

$$\hat{\Phi}(k_x, k_y, z) = \hat{\Phi}(k_x, k_y, z = 0) \cdot e^{\pm kz}, \quad (2.15)$$

where only the solution with  $e^{-kz}$  is physically relevant. We insert Eq. (2.15) into the FFT of Eq. (2.10) and obtain

$$\mathbf{b}(k_x, k_y, z = z_0) = -\nabla \left[ \hat{\Phi}(k_x, k_y, z = 0) \cdot e^{-kz_0} \right] = \mathbf{b}(k_x, k_y, z = 0) \cdot e^{-kz_0}. \quad (2.16)$$

Eq. (2.16) describes an *upward continuation*, where the magnetic field data measured at  $z = 0$  is propagated to a plane at  $z = z_0$ . In Fourier space the transformation is essentially a multiplication with

$$T_{\text{up}} = e^{-k\Delta z}, \quad (2.17)$$

where  $\Delta z$  is positive. An upward continuation leads to smoothing as all wavenumbers except  $k = 0$  are attenuated, i.e. the high-frequencies, which are responsible for sharp



features, are attenuated more strongly. The degree of attenuation increases with increasing  $\Delta z$ . This is an important finding because the amplitude of the field generated by a source modulated at a spatial frequency  $k$  on a sample surface at  $z = 0$  decays exponentially. This means that any magnetic features to be imaged by a scanning magnetometer become practically unresolvable for  $\Delta z = z_{\text{NV}} > 2\pi/k$ . Hence, the NV sample distance  $z_{\text{NV}}$  sets the spatial resolution of our scanning magnetometer.

The opposite transformation in the direction towards the source is also legitimate as long as no sources of magnetic field exist in the region of continuation (Eq. (2.11)). This transformation is called *downward continuation* and the transformation matrix in Fourier space is

$$T_{\text{down}} = e^{k\Delta z}, \quad (2.18)$$

where we propagate from a plane at  $z = z_0 + \Delta z$  to a plane at  $z = z_0$ , i.e.  $\Delta z > 0$ . In contrast to the upward continuation, here wavenumbers get exponentially amplified, which leads to a sharpening and can cause large and unrealistic variations. A straightforward and commonly used solution to that problem is the usage of a filter function discussed in Sec. 2.2.5.

### 2.2.2. Reconstruction of vector magnetic field from single field component

The NV center is sensitive to magnetic fields projected along its symmetry axis (Fig. 2.2), which corresponds to one of the four [111] crystal axes. For all diamond sensors discussed in this thesis [111] and thus the NVs have an angle of  $\theta_{\text{NV}} = 54.7^\circ$  with respect to the sample normal ( $z$ -axis). The field map thus contains a  $z$  as well as an  $x$ - or  $y$ -axis contribution. The obtained magnetic field maps are therefore not straightforward to interpret, in contrast to, for instance, SQUID measurements, which measure  $B_z$  only.

Fortunately, the components of a static magnetic field in a source-free region are not independent [53]. This means we can obtain all three components of the field everywhere in the half-space above the sample from a measurement of any single component,  $B_x$ ,  $B_y$  or  $B_z$ , in an infinite horizontal plane above the sample [53]. In a source-free region Gauss's and Ampère's law hold for the magnetic field

$$\nabla \cdot \mathbf{B} = 0 \quad (2.19)$$

$$\nabla \times \mathbf{B} = 0. \quad (2.20)$$

We can rewrite Ampère's law in Cartesian coordinates

$$\frac{\partial B_z}{\partial y} - \frac{\partial B_y}{\partial z} = 0; \quad \frac{\partial B_z}{\partial x} - \frac{\partial B_x}{\partial z} = 0; \quad \frac{\partial B_x}{\partial y} - \frac{\partial B_y}{\partial x} = 0. \quad (2.21)$$

and perform the two-dimensional Fourier transform ( $\frac{\partial}{\partial x} \rightarrow ik_x$ ,  $\frac{\partial}{\partial y} \rightarrow ik_y$ )

$$ik_y b_z - \frac{\partial b_y}{\partial z} = 0 \quad (2.22)$$

$$ik_x b_z - \frac{\partial b_x}{\partial z} = 0 \quad (2.23)$$

$$ik_y b_x - ik_x b_y = 0 \quad (2.24)$$

Equation 2.24 gives a direct connection between  $B_x$  and  $B_y$  via their Fourier transforms and provides an algebraic operation to deduce one of the two from a measurement of the other.

Using partial derivatives, Eq. (2.22) becomes

$$\lim_{\partial z \rightarrow 0} \frac{b_y(z + \partial z) - b_y(z)}{\partial z} = ik_y b_z(z). \quad (2.25)$$

In the source-free region we can use the upward continuation (Eq. (2.18))

$$\lim_{\partial z \rightarrow 0} \frac{b_y(z) e^{-k \partial z} - b_y(z)}{\partial z} = ik_y b_z(z). \quad (2.26)$$

As the limit yields zero in the numerator and denominator, we can apply l'Hôpital's rule and obtain

$$-k b_y = ik_y b_z. \quad (2.27)$$

We can rearrange Eq. (2.27) to get

$$b_y(k_x, k_y, z) = -i(k_y/k) \cdot b_z(k_x, k_y, z) \quad (2.28)$$

and similarly using Eq. (2.23)

$$b_x(k_x, k_y, z) = -i(k_x/k) \cdot b_z(k_x, k_y, z) \quad (2.29)$$

Equations 2.28 and 2.29 allow the computation of both horizontal field components from the knowledge of the vertical component. These two equations together with Eq. (2.24) link all three field components, and we can, for instance, deduce the  $z$ -component of the field from a measurement of  $B_{\text{NV}} = n_x B_x + n_y B_y + n_z B_z$  using the inverse Fourier transform of

$$b_z = \frac{b_{\text{NV}}}{-in_x \frac{k_x}{k} - in_y \frac{k_y}{k} + n_z} \quad (2.30)$$

Appendix A.5.2 shows a MATLAB implementation of this last equation.

### 2.2.3. Reconstruction of two-dimensional magnetization

In the most general case, a two-dimensional magnetization pattern cannot be uniquely determined from the measurement of a magnetic field map, as discussed later. However, if one knows the orientation of magnetization  $\mathbf{M}(\mathbf{r}) = [M_x(\mathbf{r}), M_y(\mathbf{r}), M_z(\mathbf{r})]$ , a unique solution exists [54]. For instance, for a two-dimensional magnetization  $M_z(x', y', z' = 0)$  along the  $z$ -axis the magnetic stray field is given by the sum over out-of-plane oriented magnetic dipoles and reads

$$B_z(\mathbf{r}) = \frac{\mu_0}{4\pi} \int_{-\infty}^{\infty} \int_{-\infty}^{\infty} \left( \frac{3M_z(\mathbf{r}')(z - z')^2}{|\mathbf{r} - \mathbf{r}'|^5} - \frac{M_z(\mathbf{r}')}{|\mathbf{r} - \mathbf{r}'|^3} \right) dx' dy'. \quad (2.31)$$

We can solve this equation by defining the Green's function

$$G_z(\mathbf{r} - \mathbf{r}') = \frac{\mu_0}{4\pi} \left( \frac{3z^2}{|\mathbf{r} - \mathbf{r}'|^5} - \frac{1}{|\mathbf{r} - \mathbf{r}'|^3} \right) \quad (2.32)$$

so that Eq. (2.31) becomes

$$B_z(\mathbf{r}) = \int_{-\infty}^{\infty} \int_{-\infty}^{\infty} M_z(\mathbf{r}') G_z(\mathbf{r} - \mathbf{r}') dx' dy'. \quad (2.33)$$

This convolution is a trivial multiplication in Fourier space of the form

$$b_z(k_x, k_y, z) = g_z(k_x, k_y, z) \cdot m_z(k_x, k_y, 0). \quad (2.34)$$

The analytical expression of the Fourier transform of the Green's function (Eq. (2.32)) is [54]

$$g_z(k_x, k_y, z) = \frac{\mu_0}{4\pi} 2\pi k e^{-kz}. \quad (2.35)$$

The  $z$ -component of the magnetic field is therefore

$$b_z(k_x, k_y, z) = \mu_0 k \frac{e^{-kz}}{2} m_z(k_x, k_y). \quad (2.36)$$

We can also extract  $B_{x,y}$  with the help of Eq. (2.28) and (2.29)

$$b_{x,y}(k_x, k_y, z) = -i\mu_0 k_{x,y} \frac{e^{-kz}}{2} m_z(k_x, k_y). \quad (2.37)$$

Appendix A.5.3 shows a MATLAB implementation of the solution for  $M_z(x, y, z = 0)$  from a measurement of  $B_{\text{NV}}(z = z_{\text{NV}})$ , which is the Fourier transform of

$$m_z(k_x, k_y, z = 0) = \frac{b_{\text{NV}}(z = z_{\text{NV}})}{-i\mu_0 \frac{e^{-kz_{\text{NV}}}}{2} (k_x n_x + k_y n_y) + \mu_0 k \frac{e^{-kz_{\text{NV}}}}{2} n_z} \quad (2.38)$$

An analogous derivation via the magnetic potential can be found in [35, 55].

As long as the magnetization orientation is known, the transformation for any magnetization can be derived using the dipolar tensor  $\mathbf{D}(\mathbf{k}, z)$  [18, 20]

$$\mathbf{D}(\mathbf{k}, z) = \frac{\mu_0}{2} k e^{-kz} \begin{pmatrix} -\left(\frac{k_x}{k}\right)^2 & -\frac{k_x k_y}{k^2} & -i\frac{k_x}{k} \\ -\frac{k_x k_y}{k^2} & -\left(\frac{k_y}{k}\right)^2 & -i\frac{k_y}{k} \\ -i\frac{k_x}{k} & -i\frac{k_y}{k} & 1 \end{pmatrix} \quad (2.39)$$

We can formulate the magnetic field above the sample as

$$\mathbf{b}(\mathbf{k}, z) = \mathbf{D}(\mathbf{k}, z) \cdot \mathbf{m}(\mathbf{k}), \quad (2.40)$$

where  $\mathbf{m}(\mathbf{k}) = [m_x(\mathbf{k}), m_y(\mathbf{k}), m_z(\mathbf{k})]$  is the magnetization. We can easily verify that we reproduce Eq. (2.36) and (2.37) by substituting  $\mathbf{m}(\mathbf{k}) = [0, 0, m_z(\mathbf{k})]$  into Eq. (2.40).

The dipolar tensor is a beautiful construct as it reveals two very nice properties. First, the rows of the dipolar tensor are linearly dependent<sup>4</sup>. A direct consequence is that it is sufficient to know one component of the field to calculate the other unknown components<sup>5</sup>, which we have already seen in Sec. 2.2.2. However, another consequence is that we cannot reconstruct an arbitrary magnetization from the stray field without further information about the magnetization, since the mapping between  $\mathbf{b}$  and  $\mathbf{m}$  is not unique.

Second, the dipolar matrix contains the filter function  $ke^{-z_{\text{NV}}k}$  (with  $z = z_{\text{NV}}$  the NV sensor distance) depicted in Fig. 2.9b. This filter function describes the sensitivity of the sensor to spatial variations ( $k$ -values) of the magnetization. A homogeneous magnetization ( $k = 0$ ) produces no stray field and the filter function is zero, meaning the sensor cannot detect homogeneous magnetization. The product with  $k$  in the filter function reflects that our sensor is only sensitive to gradients of the magnetization because the derivative in  $k$ -space is exactly  $k$ . Hence, a divergence-less magnetization ( $\nabla \cdot \mathbf{M}(\mathbf{r}) = 0$ ) produces no stray field. A given stray field distribution can therefore be generated from an infinite number of magnetization patterns that differ by any number of divergence-free magnetization distribution. In the case of an antiferromagnet with fast alternating spin directions ( $k \gg 1/z_{\text{NV}}$ ), there is a stray field, which, however, decays exponentially due to the upwards continuation. The maximum sensitivity is given for spins that oscillate over a length scale of the NV sample distance ( $k_{\text{max}} \sim 1/z_{\text{NV}}$ ).

---

<sup>4</sup>  $row_1 = row_3 \cdot \left(-i \frac{k_x}{k}\right), \quad row_2 = row_3 \cdot \left(-i \frac{k_y}{k}\right)$

<sup>5</sup>  $b_x = b_z \cdot \left(-i \frac{k_x}{k}\right), \quad b_y = b_z \cdot \left(-i \frac{k_y}{k}\right)$

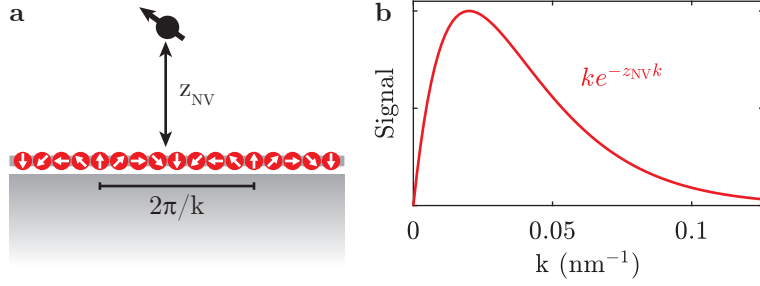


**Figure 2.9.: NV sensitivity to spatial variations of the magnetization.** **a** The NV center is placed a distance  $z_{\text{NV}}$  above a magnetization whose spins have a spatial variation of wavelength  $2\pi/k$ . **b** The NV center is not sensitive to uniform magnetization (with  $k = 0$ ) nor to fast alternating spins (with  $k \gg 1/z_{\text{NV}}$ ). The best sensitivity is achieved for spins that fluctuate at the length scale of the NV sensor distance ( $k_{\text{max}} \sim 1/z_{\text{NV}}$ ). In the graph  $z_{\text{NV}} = 50$  nm and the maximum signal corresponds to  $k_{\text{max}} \sim 1/z_{\text{NV}} = 0.02$ .

#### 2.2.4. Reconstruction of two-dimensional current distribution

The inverse problem of inferring a two-dimensional current distribution from a magnetic stray field can be solved uniquely. This follows directly from Sec. 2.2.3 as a 2D current distribution is equivalent to a uniaxial magnetization along the  $z$ -axis. Similarly to the derivation of the magnetization, we assume a source-free region with static current  $\mathbf{J}$

$$\nabla \cdot \mathbf{J} = 0 \quad (2.41)$$

and can write down the magnetic field produced by a current density using the Biot-Savart law

$$\mathbf{B}(\mathbf{r}) = \frac{\mu_0}{4\pi} \int \frac{\mathbf{J}(\mathbf{r}') \times (\mathbf{r} - \mathbf{r}')}{|\mathbf{r} - \mathbf{r}'|^3} d^3\mathbf{r}'. \quad (2.42)$$

The  $x$ -component of the magnetic field is

$$B_x(x, y, z) = \frac{\mu_0 z}{4\pi} \int_{-\infty}^{\infty} \int_{-\infty}^{\infty} \frac{J_y(x', y')}{[(x - x')^2 + (y - y')^2 + z^2]^{3/2}} dx' dy'. \quad (2.43)$$

This is a convolution with the Green's function

$$G(x - x', y - y', z) = \frac{\mu_0 z}{4\pi} \frac{1}{[(x - x')^2 + (y - y')^2 + z^2]^{3/2}} dx' dy', \quad (2.44)$$

which in Fourier space is [56]

$$g(k_x, k_y, z) = \frac{\mu_0}{2} e^{-kz}. \quad (2.45)$$

Hence, we can write the relationship between  $B_x$  and  $J_y$  in Fourier space as

$$b_x(k_x, k_y, z) = \frac{\mu_0}{2} e^{-kz} j_y(k_x, k_y, z = 0). \quad (2.46)$$

In the same fashion we can obtain

$$b_y = -\frac{\mu_0}{2} e^{-kz} j_x \quad (2.47)$$

$$b_z = i\frac{\mu_0}{2} e^{-kz} \left( \frac{k_y}{k} j_x - \frac{k_x}{k} j_y \right). \quad (2.48)$$

The last equation indicates that the current distribution  $j_x$  and  $j_y$  cannot be obtained individually from a measurement of  $b_z$ . Fortunately, we can also use the equation of continuity (Eq. (2.41)), which in two-dimensions is

$$\frac{\partial J_x}{\partial x} + \frac{\partial J_y}{\partial y} = 0 \quad (2.49)$$

and perform the two-dimensional Fourier transform ( $\frac{\partial}{\partial x} \rightarrow ik_x$ ,  $\frac{\partial}{\partial y} \rightarrow ik_y$ ) to obtain

$$ik_x j_x + ik_y j_y = 0 \quad (2.50)$$

to deduce both  $j_x$  and  $j_y$  independently from  $b_z$ . Finally, we can solve for the current distribution  $j_x$  and  $j_y$  that produces a magnetic field along the NV axis [24, 25]

$$j_x = \frac{k_y b_{\text{NV}}}{\frac{\mu_0}{2} e^{-kz} [n_y k_y - n_x k_x + i n_z k]} \quad (2.51)$$

$$j_y = \frac{k_x b_{\text{NV}}}{\frac{\mu_0}{2} e^{-kz} [n_x k_x - n_y k_y - i n_z k]} \quad (2.52)$$

Appendix A.5.4 shows a MATLAB implementation of the solution for  $\mathbf{J}(x, y, z = 0)$  from a measurement of  $B_{\text{NV}}(z = z_{\text{NV}})$ .

### 2.2.5. Windowing technique

As already discussed, the downward continuation is a critical step in that high-spatial frequencies are exponentially amplified. Next to signal, also noise present at high frequencies is amplified. A possible solution to mitigate this issue is a low pass filter applied in Fourier space. The most trivial low pass filter is a rectangular window that cuts all wave vectors  $k$  above a cutoff vector  $k_{\text{cut}}$ . However, the multiplication of the signal with a rectangular function in Fourier space corresponds to a convolution with a sinc function in reals space causing artifacts. To surmount this difficulty, one can use a Hanning window, which is a common choice [25, 35, 56, 57] but still straightforward to implement. It is given by

$$W(k) = \begin{cases} 0.5 \cdot [1 + \cos(kz_{\text{NV}}/2)], & \text{for } k < k_{\text{cut}} \\ 0, & \text{for } k > k_{\text{cut}}. \end{cases} \quad (2.53)$$

The cutoff frequency  $k_{\text{cut}}$  must be determined experimentally and depends on sensor sample distance  $z_{\text{NV}}$ , the amplitude of sensor noise and the spatial frequency content of the field source. A natural choice is  $k_{\text{cut}} = 2\pi/z_{\text{NV}}$ . This decreases high-frequency

noise and provides a stable reverse propagation at the cost of spatial resolution. In the case of a scanning NV center that is very close to the surface, the propagation distance is small and, hence, amplification of noise is modest, resulting in a conserved high spatial resolution.

A possible implementation of the Hanning window in MATLAB is shown in Appendix A.5.4. Given that the NV is neither particularly sensitive to small and large  $k$ -vectors (see Fig. 2.9b), it might be beneficial to not only use a Hanning window to cut high frequency components but use a bandpass filter with a profile reflecting the NV sensitivity.

### 2.3. Implementation of the cryogenic setup

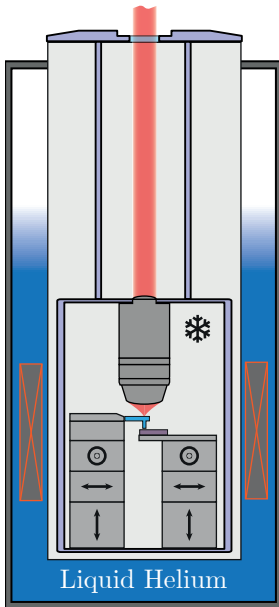


**Figure 2.10.:**  
**Schematic of the 4 K**  
**cryogenic scanning**  
**NV setup.**

Since thermal energy at room temperature exceeds quantization energies in various system, quantum effects are washed out or are completely destroyed. In order to probe these effects, cryogenic experimental conditions are required. Although the combination of atomic force microscopy and optical addressing of NV spins under cryogenic conditions has been demonstrated [58], cryogenic operation of a scanning NV magnetometer has remained an outstanding challenge. A confocal microscope is required to address the electronic spin of the NV center, while the atomic force microscope minimizes the distance between the NV spin and the sample, allowing high resolution and measurement of small magnetic signals [16, 34]. The complexity of such a setup is reflected in the fact, that (at time of writing) only one other experiment demonstrated the experimental realization of it [59, 60].

In this section, we present the first low-temperature scanning NV magnetometry setup. We explain the composition of the setup, demonstrate its potential by imaging magnetic stray fields close to superconductors [59, 61] (see Chap. 3), and employ it to advance the field of two-dimensional ferromagnets [55] (see Chap. 4).

At liquid helium temperatures this setup can be implemented in two ways: as a flow- or bath cryostat. In a flow-cryostat the sample and tip stack are cooled through thermal contact to a cold finger. On the other hand in a bath cryostat the sample, tip stack and objective are cooled via an exchange gas. This approach yields high cooling-power (see Fig. 2.11a), minimal vibrations for AFM operation as it avoids excess vibrations originating from liquid-nitrogen boil-off or closed-cycle cryostat operation, and allows for full, vectorial magnetic field control in the Tesla range. The availability of high magnetic fields is a clear advantage over the flow-cryostat approach, especially when correlated electronic system are to be addressed, which often require substantial fields. Therefore, we decided to employ a  $^4\text{He}$  bath cryostat with a base-temperature of 4.2 K as sketched in Fig. 2.10.

Our experimental setup is based on a low-temperature, tuning-fork based AFM (Attocube, attoLIQUID 1000). The microscope including the sample, the diamond tip and the objective is placed in a  $^4\text{He}$  buffer-gas filled, stainless steel housing, which is directly immersed in a low-vibration, Nitrogen-free, liquid  $^4\text{He}$  bath cryostat for cooling. The cryostat is equipped with a 3D superconducting vector magnet (Janis), which allows for the application of 0.5 T in all directions. The all-diamond cantilever is attached to a tuning fork for force-feedback for AFM [16, 34], which is provided by commercial electronics (Attocube, ASC500). Two separate positioning units (Attocube, ANSxyz50 scanners on top of ANPxyz51 positioners) provide individual high accuracy positioning of both the sample and sensor. This allows for



independent respective alignment of cantilever, optical axis and sample. The coarse horizontal positioning range is 3 mm and the fine scan range is 15  $\mu\text{m}$  at low temperatures. Typical root mean square (RMS) AFM vibration between the tip and the sample in the vertical direction of a linescan with feedback is below 1 nm. Long-term tip-sample drift was not explicitly measured. However, no relevant drifts have been observed in measurements over a period of several days, as a consequence of the cryogenic environment and the temperature stability of the system.

Optical access to the AFM tip is provided by a quartz window on top of the cryostat and an achromatic, low temperature-compatible objective (Attocube LT-APO/VISIR/0.82, 0.82 NA), rigidly attached to the microscope head. A home-built, fiber based confocal microscope is directly mounted on top of the cryostat. Excitation light for NV fluorescence is provided by a solid-state laser at 532 nm (LaserQuantum, GEM532). Red fluorescence photons are coupled into a single-mode fiber guided to an avalanche photo diode for counting (Excelitas, SPCM-ARQH-13). This optical composition allowed for typical 1.3 M counts per second of a single NV center embedded in a diamond cantilever at saturation and low temperature as depicted in Fig. 2.11b.

Data acquisition and scan control is achieved using a digital acquisition card (National Instruments, NI-6602 and NI-6733) and a Matlab-based experiment control software. Microwave signals for spin manipulation are generated by a signal generator (Rohde&Schwarz, SMB100A), amplified (Minicircuit, ZHL-42W+) and delivered to the NV center using a gold wire (diameter, 25  $\mu\text{m}$ ) positioned across the sample. Temperature control of the sample above 4.2 K is provided by a resistive heater (IMS, ND3-1206EW1000G) and a temperature controller (LakeShore, Model 355). So far we applied a highest temperature of 120 K, but have not checked the upper heating limit. The bath cryostat is filled with roughly 60 liters of liquid helium allowing for a continuous measurement time of 5.5 days. Figure 2.12 gives further insight into our scanning NV setup. While all experiments presented in Chap. 3 and 4 are continuous wave experiments based on ODMR, we experienced some issues with pulsed experiments, which are described in Appendix A.1.5.

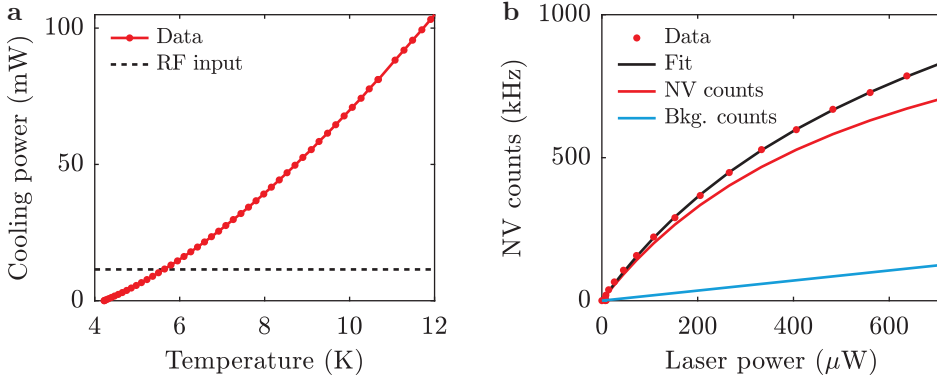


**Figure 2.11.: Cooling power of the setup and saturation curve of a NV center.** **a** We compare the cooling power of our  $^4\text{He}$  bath cryostat with the power input of the microwave field. To that end, we measured the equilibrium temperature as a function of estimated microwave power at the sample location. The microwave power required to drive electron spin resonance on the NV center is indicated by the black dashed line. The temperature dependent cooling power of the cryostat is shown with the red dotted line. Heating due to microwave current leads to a measurement temperature of 6 K for most experiments. **b** Power saturation curve of an NV center in the cryogenic setup. NV counts are recorded as a function of green excitation power. The data is fitted to  $I(P) = I_{\text{sat}}P/(P + P_{\text{sat}}) + PI_{\text{bkg}}$ , where  $P$  is the excitation power in  $\mu\text{W}$ ,  $I_{\text{sat}} = 1290$  kCPS the saturation counts,  $P_{\text{sat}} = 590$   $\mu\text{W}$  the saturation power and  $I_{\text{bkg}} = 176$  CPS/ $\mu\text{W}$  the background counts per  $\mu\text{W}$ . In our experiments we typically use between 30  $\mu\text{W}$  and 200  $\mu\text{W}$  excitation power.

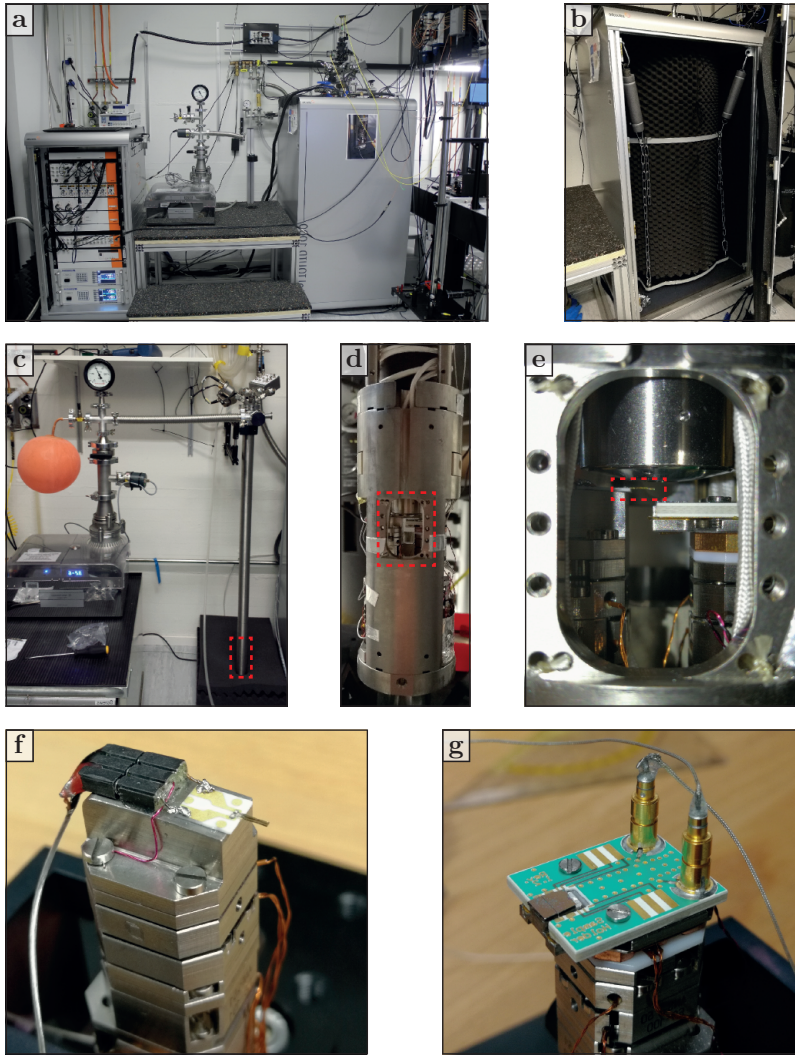


**Figure 2.12.:** **a** Control rack with position controllers, AFM controllers, and magnet power supplies (left) and  $^4\text{He}$  bath cryostat (right). A fiber based confocal microscope is directly mounted on top of the cryostat. **b** The bath cryostat is suspended on springs resulting in low vibrations essential for AFM. **c** The microscope (including a quartz window for optical access, the sample, the diamond tip and the objective) is placed in a long tube filled with  $^4\text{He}$  exchange gas visible on the right side of the image. The setup for evacuating the tube and filling it with  $^4\text{He}$  buffer-gas is shown. **d** A titanium housing containing the objective, the sample and diamond cantilever is at the very bottom of the tube (red dashed box in **c**). **e** Close-up of the housing (red dashed box in **d**) with objective (top), the tip stack (left) and sample stack (right) below the objective. The tuning fork, at which end the diamond cantilever is mounted, is highlighted with a red dashed box. **f** Tip stack with tuning fork and diamond cantilever at its end. The tuning fork is read out electrically. **g** The sample is mounted on the left of a circuit board (green). A gold wire bonded over the sample for NV spin manipulation is faintly visible. The circuit board is fixed on a piezo stack.



### 3. Magnetic imaging of superconductors

After successfully setting up a scanning NV magnetometer at cryogenic temperatures, we wanted to test its performance. The ideal sample for that purpose would feature nanoscale magnetic phenomena present at low temperatures, which are theoretically well understood and have already been observed experimentally. This would enable us to benchmark the performance of our magnetometer against others, to model the imaged stray fields, test the quality of our data and extract important setup parameters like spatial resolution or sensitivity.

Vortices in a high-temperature superconductor are an ideal testbed for the above mentioned criteria. They are highly localized, quantized and exhibit stray fields well within our detection limits. They have been imaged in YBCO by various techniques ranging from MFM [62] to scanning Hall probes [63], scanning tunneling spectroscopy [64], SQUID [65] and ensemble NV magnetometry [66] among others. In addition, vortex stray fields are well understood and can be calculated analytically [67, 68].

In this chapter we demonstrate the applicability of our method by imaging superconducting vortices in yttrium barium copper oxide (YBCO), a prototypical superconductor with a transition temperature of  $T_c = 89$  K, which allows us to unambiguously determine the system's local penetration depth. Further, thanks to our unprecedented spatial resolution, we experimentally show that the widely used monopole model – an approximative description of a vortex stray field – is not valid at close proximity to the sample. Section 3.1 gives an introduction to the underlying theory required to understand the experimental data. We will introduce the London penetration depth, the coherence length and provide the reader with a description of stray fields originating from vortices. In Sec. 3.2 we introduce the examined superconductor YBCO and present full field images of vortices along with quantitative analysis of the data. The presented results have been published in [59, 61].

#### 3.1. Theoretical background

In 1911, Kammerlingh Onnes succeeded in liquifying  $^4\text{He}$  at a temperature of 4.2 K. His motivation was to end an ongoing debate whether the resistance of pure metals will continuously decrease with decreasing temperature, approaching zero, or if electrons will freeze, which would result in a sudden increase of resistance. What he found instead was a sudden drop of resistance in mercury, lead and tin below a critical temperature [69]. This phenomena has been a mystery for a long time and is now well-known as superconductivity. The hallmarks of superconductivity are not only perfect conductivity but also perfect diamagnetism, which was found in 1933 by Meissner and Ochsenfeld [70]. They observed that superconductors expel magnetic fields from

its interior not only when the material is already superconducting but even when they are cooled below its critical temperature  $T_c$  in a magnetic field, the Meissner effect. Electrons in a superconductor pair up to so-called Cooper pairs named after Leon Cooper, one of the inventors of the Bardeen-Cooper-Schrieffer (BCS) theory [71]. Cooper pairs are bosonic, which allows them to condensate into a common, macroscopic quantum ground state, thereby lowering the free energy of the superconductor. The expulsion of magnetic field increases the free energy of the superconductor and a transition to a normal conductor takes place when the increase in free energy due to the magnetic field balances the drop due to condensation. This happens at the critical magnetic field  $H_c$ . Together with the critical current  $J_c$  and the critical temperature  $T_c$  they span the critical surface of superconductivity (see Fig. 3.1), which separates superconductivity from the normal state.

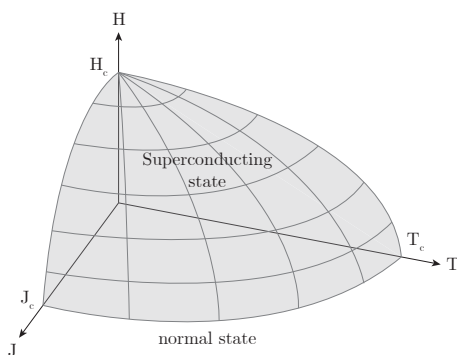


**Figure 3.1.: Critical surface of a superconductor.** The critical surface characterized by the critical magnetic field  $H_c$ , the critical current  $J_c$ , and the critical temperature  $T_c$  separate the superconducting from the normal state. The figure is adapted from [72], World Scientific.

### 3.1.1. London penetration depth and coherence length

In this chapter we introduce two fundamental parameters that define any superconductor. We will see that the lateral extent of the stray field of a vortex is set by the London penetration depth and the width of the normal conducting core by and the coherence length.

In 1935, the London brothers proposed two equations [73] to describe perfect conduction and the Meissner effect in a phenomenological manner

$$\mathbf{E} = \frac{m}{n_s e^2} \frac{\partial \mathbf{J}}{\partial t} \quad (3.1)$$

$$-\frac{n_s e^2}{m} \mathbf{B} = \nabla \times \mathbf{J}, \quad (3.2)$$

where  $\mathbf{E}$  is the electric field,  $\mathbf{J}$  the supercurrent,  $\mathbf{B}$  the magnetic field,  $e$  and  $m$  the charge and effective mass of an electron and  $n_s$  the number density of superconducting electrons. While scattering of electrons with ions limits the acceleration of electrons

due to an external electric field in a normal conductor<sup>1</sup>, Eq. (3.1) describes perfect conductivity with a constant acceleration of the electrons by an electric field<sup>2</sup>. We can rewrite the second equation using Ampère’s law  $\nabla \times \mathbf{B} = \mu_0 \mathbf{J}$  to describe the field expulsion

$$\nabla^2 \mathbf{B} = -\frac{1}{\lambda_L^2} \mathbf{B}, \quad \lambda_L = \sqrt{\frac{m}{\mu_0 e^2 n_s}}. \quad (3.3)$$

The equation describes the decay of the magnetic field inside the superconductor over a characteristic length scale  $\lambda_L$ , the “London penetration depth”.

The “coherence length” is derived in another phenomenological theory proposed by Ginzburg and Landau [74]. Ginzburg and Landau described the superconducting state by a complex order parameter,  $\psi(\mathbf{r}) = |\psi(\mathbf{r})|e^{i\Theta(\mathbf{r})}$ , where  $\Theta$  is the superconducting phase. In the normal state the order parameter is zero, whereas in the superconducting state it is related to the local density of superconducting electrons,  $|\psi(\mathbf{r})|^2 = n_s(\mathbf{r})$ . Ginzburg and Landau described the free energy of the superconductor in terms of the order parameter and minimized the free energy with respect to it to derive the two Ginzburg-Landau equations [75]

$$\alpha\psi + \beta|\psi|^2\psi + \frac{1}{2m^*}(-i\hbar\nabla - 2e\mathbf{A})^2\psi = 0 \quad (3.4)$$

$$\mathbf{J} = \frac{2e}{m^*}|\psi|^2(\hbar\nabla\Theta - 2e\mathbf{A}) = 2e|\psi|^2\mathbf{v}_s, \quad (3.5)$$

where  $\alpha$  and  $\beta$  are phenomenological parameters,  $m^*$  the effective mass of a Cooper pair,  $e$  the electron charge,  $\mathbf{A}$  the magnetic vector potential, and  $\mathbf{v}_s = \frac{1}{m^*}(\hbar\nabla\Theta - 2e\mathbf{A})$  the superfluid velocity. When we neglect the nonlinear term  $\beta|\psi|^2\psi$  in the first Ginzburg-Landau equation (Eq. (3.4)), we can derive a linear differential equation for the Ginzburg-Landau coherence length  $\xi$  in the low field limit

$$\nabla^2\psi + \frac{1}{\xi^2}\psi = 0, \quad \xi(T) = \sqrt{\frac{\hbar^2}{2m^*|\alpha(T)|}}. \quad (3.6)$$

The coherence length  $\xi$  is a characteristic length scale for the spatial variation of the order parameter  $\psi$ .

<sup>1</sup>In Ohm’s law the current density  $\mathbf{J} = nev$  is proportional to the electric field  $\mathbf{E}$ :  $\mathbf{J} = \sigma\mathbf{E}$ , where  $\sigma$  is the conductivity.

<sup>2</sup>According to the first London equation, the acceleration  $\mathbf{a}$  is proportional to the electric field:  $\mathbf{E} = \frac{m}{n_s e^2} \frac{\partial \mathbf{J}}{\partial t} = \frac{m}{n_s e^2} \frac{\partial(n_s e \mathbf{v})}{\partial t} = \frac{m}{e} \mathbf{a}$ .

### 3.1.2. Type-I vs type-II superconductor and vortices

The two characteristic length scales introduced in the previous chapter – the coherence length  $\xi$  and the London penetration depth  $\lambda_L$  – are responsible for the distinction between two classes of superconductors, namely type-I and type-II superconductors. The ratio  $\kappa = \lambda_L/\xi$  is defined as the Ginzburg-Landau parameter and allows for the classification of superconductor in type-I and type-II. In this section we will see that the surface energy, associated with the energy cost of a normal/superconducting interface, is positive and unfavorable for type-I and negative and therefore beneficial for type-II superconductors.

In order to understand this, we want to look at the boundary of a normal conducting and superconducting region in the presence of an external magnetic field as sketched in Fig. 3.2. The normal region expands from  $x = 0$  to negative  $x$  and the superconducting to positive  $x$ . In the superconducting state the superconductor can lower its energy because of the condensation into Cooper pairs. We will call this energy the condensation energy  $E_C$ . If we apply a magnetic field, the superconductor has to pay the expulsion energy  $E_B$  consisting of the energy of the magnetic field and the kinetic energy of the supercurrent. As long as  $E_B < E_C$ , it is energetically favorable for the superconductor to be superconducting. In the normal conducting region we have a Cooper pair density  $n_s$  of zero and no field screening, hence,  $E_B = E_C = 0$ . Within the boundary ( $0 < x < \max(\lambda_L, \xi)$ ),  $n_s$  increases from zero to a finite value over a length scale given by the coherence length  $\xi$ . This is accompanied with the increase of the condensation energy  $E_C$ , which is proportional to  $n_s$ , over the same length scale  $\xi$  (Fig. 3.2, blue line). At the same time the external magnetic field penetrates the superconductor and decays inside the superconductor with the London penetration depth  $\lambda_L$  due to induced supercurrents (Fig. 3.2, red line). Therefore the field is not completely screened within the boundary and the expulsion energy  $E_B$  increases as

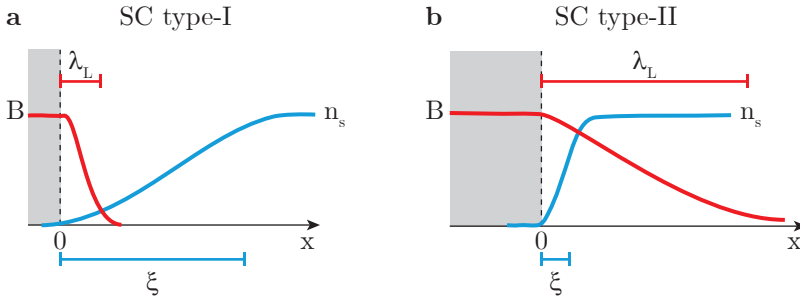


**Figure 3.2.: Interface between normal conducting and superconducting domains.** The normal conducting region is colored in grey and extends from  $x = 0$  towards negative  $x$ -values. The magnetic field (red) is screened inside the superconductor (SC) on a length scale of the London penetration depth  $\lambda_L$ . The Cooper pair density  $n_s$  increases from zero to a non-zero value on the length scale of the coherence length  $\xi$ . **a** In type-I superconductor,  $\lambda_L \ll \xi$  and the surface energy is positive (see text). **b** In type-II superconductor,  $\lambda_L \gg \xi$  and the surface energy is negative (see text).



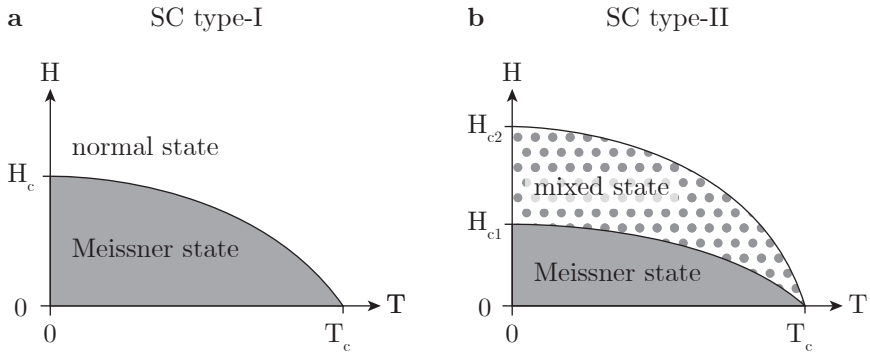


**Figure 3.3.: H-T phase diagrams for type-I and type-II superconductors.**

**a** In a type-I superconductor the magnetic field ( $H$ ) is screened from the inside of the superconductor up to a critical field, where the expulsion energy exceeds the condensation energy. Above the critical field or above the critical temperature  $T_{c0}$ , superconductivity is destroyed and the sample is in the normal state. **b** A type-II SC is in the Meissner state up to a first critical field  $H_{c1}$ . With increasing magnetic field  $H_{c1} < H < H_{c2}$  magnetic flux in form of vortices penetrates the superconductor in the so-called mixed state. The figure is adapted from [72], World Scientific.

we go from the interface at  $x = 0$  towards positive  $x$ -values on the length scale of the London penetration depth  $\lambda_L$ . Inside the superconductor ( $x \geq \lambda_L$ ), the external magnetic field is completely screened and the superconductor pays the full expulsion energy. This means for  $\lambda_L \ll \xi$ , the expulsion energy arrives at its full value before the condensation energy leading to a net cost in energy and a positive surface energy. On the other hand, for  $\lambda_L \gg \xi$  the reduction in energy due to the condensation energy exceeds the energy cost of the field expulsion resulting in a negative surface energy. The surface energy is balanced for a Ginzburg-Landau parameter of  $\kappa = 1/\sqrt{2}$ .

Superconductors with  $\kappa < 1/\sqrt{2}$  ( $\xi > \sqrt{2}\lambda_L$ ) are known as type-I superconductors and their surface energy is positive. As a consequence, type-I superconductors stay in the Meissner phase up to a critical field  $H_c$  characterized by complete flux expulsion. Above the critical field, the whole material turns into a normal conductor. The situation is depicted in the H-T phase diagram in Fig. 3.3a.

Type-II superconductors have a negative surface energy and are characterized by the Ginzburg-Landau parameter  $\kappa > 1/\sqrt{2}$  ( $\xi < \sqrt{2}\lambda_L$ ). Up to a lower critical field  $H_{c1}$ , which is given by [75]

$$H_{c1} = \frac{\Phi_0}{4\pi\lambda^2} \ln(\kappa), \quad (3.7)$$

a type-II superconductor is in the Meissner phase. At this field, the free energy of the superconductor with and without a vortex is the same. Above  $H_{c1}$ , it gets energetically favorable to have bundles of flux with a normal core penetrating the superconductor. The magnetic flux  $\phi$  of these bundles is quantized and has to be an integer multiple of the flux quantum  $\phi_0 = h/2e = 2.07 \text{ mT}\mu\text{m}^2$  (see Appendix A.2.1). As type-II superconductors have a negative surface energy, rather than having few flux bundles carrying multiple flux quanta, they prefer to generate many flux bundles

with the lowest possible flux ( $\phi = \phi_0$ ), so-called vortices. A schematic representation of a vortex is given in Fig. 3.4. It has a normal conducting core, which is surrounded by supercurrents. The size of the core is  $\xi$  and the Cooper pair density  $n_s$  decays to zero in the center of the vortex, where the stray magnetic field  $B$  is at its maximum value. The screening currents  $J$  lead to the decay of the stray fields on the length scale of the London penetration depth  $\lambda_L$ .

The number of vortices in an area is  $n_{\Phi_0} = A \cdot B / \Phi_0$ , where  $A$  is the area and  $B$  is the external magnetic field. With increasing field, the number of vortices increases until the vortex cores overlap at a second critical field  $H_{c2}$

$$H_{c2} = \frac{\Phi_0}{2\pi\xi^2}. \quad (3.8)$$

This critical field is determined by the size of the vortex cores, i.e. the coherence length  $\xi$ . The H-T phase diagram of a type-II superconductor is shown in Fig. 3.3b.

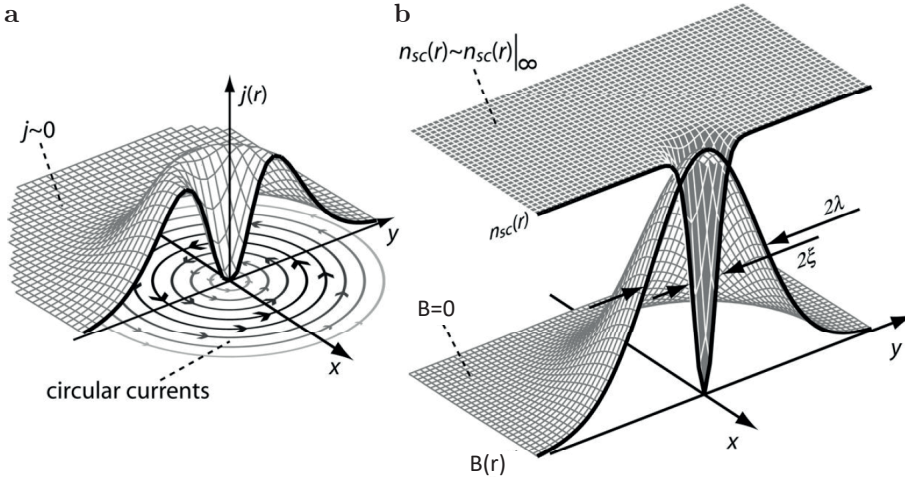


**Figure 3.4.: Schematic of a vortex.** **a** Distribution of the shielding currents around the vortex core inside the superconductor. The currents are zero inside the normal conducting core and decay over a distance given by the London penetration depth  $\lambda_L$ . **b** Radial distribution of the magnetic stray field  $B(r)$  and the density of superconducting electrons  $n_s(r)$ . The size of the core is given by the coherence length  $\xi$ . In the center  $n_s = 0$  and the magnetic field is maximal. The magnetic field decays due to the screening currents on the length scale of  $\lambda_L$ . The figure is adapted from [72], World Scientific.

## 3.2. Experimental Realization

### 3.2.1. Yttrium barium copper oxide fabrication and samples

In 1986, Bednorz and Muller [76] discovered the superconductor  $\text{La}_4\text{Ba}_1\text{Cu}_5\text{O}_5$  with a critical temperature  $T_c = 23$  K above what was theoretically allowed by the BSC theory [71, 77]. One year later the compound  $\text{YBa}_2\text{Cu}_3\text{O}_{7-\delta}$  (YBCO,  $T_c = 89$  K) [78] was found – the first superconductor with a critical temperature above the boiling temperature of liquid nitrogen – marking a breakthrough in the history of high temperature superconductors. YBCO is a layered cuprate material with copper oxide (Cu-O) planes as depicted in Fig. 3.5a. It has an orthorhombic distorted structure with strong superconductivity in the  $a$ - $b$  planes (Cu-O layers) and weak superconductivity along the crystallographic  $c$ -axis. Therefore, supercurrents are larger within the Cu-O planes than perpendicular to the planes, which makes YBCO an anisotropic superconductor. For instance, the penetration depth along the  $c$ -axis,  $\lambda_c$ , is about seven times as large as in the  $a$ - $b$  plane  $\lambda_{ab}$ . Since we only applied magnetic fields long the  $c$ -axis, we are only interested in the latter quantity. Therefore, we will refer to  $\lambda_{ab}^3$  as  $\lambda_L$ . The coherence length in YBCO is in the sub-nanometer range, which

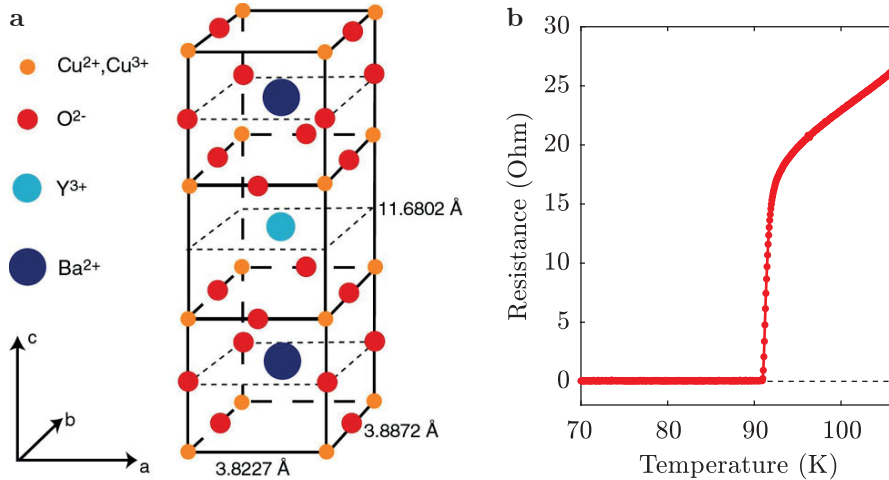


**Figure 3.5.: Crystalline structure of YBCO and critical temperature.** **a** YBCO unit cell. Cu-O sheets in the  $a$ - $b$  plane sandwich alternating a yttrium (Y) and barium (Ba) atoms. Superconductivity is strong in the Cu-O planes and weak perpendicular to them. This renders YBCO a layered, anisotropic superconductor. The dimensions of the unit cell are indicated along the corresponding crystallographic axes. Figure adapted from [79]. **b** Four-point measurement of temperature dependent resistivity in YBCO (sample B, see Fig. 3.6b). The critical temperature is in good agreement with its literature value around  $T_c = 89$  K.

<sup>3</sup>Note that due to strong twinning in our thin film sample, the in-plane London penetration depth is essentially isotropic ( $\lambda_{ab} = \sqrt{\lambda_a \lambda_b} = \lambda_L$ ).

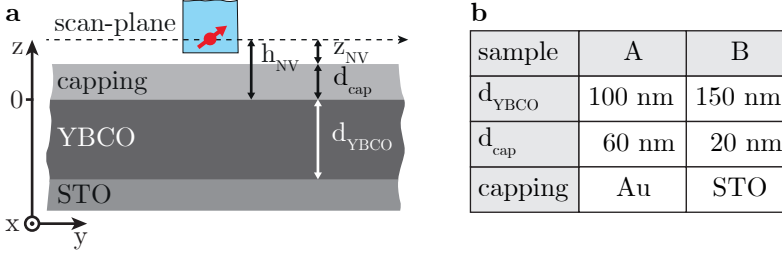


**Figure 3.6.: Sample design and dimensions.** **a** Layout of sample and scanning NV sensor. The red arrow and blue structure indicate the NV spin and diamond nanopillar, respectively, at distance  $z_{\text{NV}}$  from the sample surface, and  $h_{\text{NV}}$  from the superconductor surface. The superconducting YBCO film ( $0 > z > -d_{\text{YBCO}}$ ) was grown on a STO substrate and covered by a protective layer (thickness  $d_{\text{cap}}$ ). **b** Main parameters for samples A and B.

is below our measurement resolution and can be neglected. The lower critical field  $H_{c1}$  is around 15 mT and the upper critical field  $H_{c2} = 140$  T [80].

The studied samples consist of thin, single-crystalline film of YBCO, which was grown by the group of Prof. Kölle and Prof. Kleiner<sup>4</sup>. The layout of the samples and corresponding thicknesses are listed in Fig. 3.6.

Our collaborators fabricated epitaxially grown  $c$ -axis oriented  $\text{YBa}_2\text{Cu}_3\text{O}_{7-\delta}$  thin films on  $\text{SrTiO}_3$  (STO) single crystal (001)-oriented substrates by pulsed laser deposition (PLD), followed either by in-situ electron-beam-evaporation of Au at room temperature (sample A) or by in-situ epitaxial growth of an STO cap layer by PLD (sample B). For details on PLD growth of the YBCO films on STO substrates, and their structural and electric transport properties see [81, 82]. In brief, the YBCO films typically yield  $0.1^\circ$  full width half maximum of the rocking curve at the (005) x-ray diffraction peak, have an inductively measured transition temperature  $T_c = 89$  K and normal state resistivity  $\rho \approx 50 \mu\Omega\text{cm}$  at  $T = 100$  K. The thicknesses of the samples were determined through in-situ reflection high-energy electron diffraction (RHEED) for the YBCO and STO films. With the  $c$ -axis lattice parameters, as measured via x-ray diffraction, they then obtain the thicknesses for the YBCO and STO films quoted in Fig. 3.6b. The Au growth rate was determined via a quartz-crystal monitor. For all layers, the estimated error in the thickness determination is 2 – 3 %.

<sup>4</sup>Kleiner-Kölle Group, University of Tübingen (Germany)

### 3.2.2. Quantitative vortex imaging and analysis

To nucleate vortices at a well-defined density, we field-cooled sample A from a temperature  $T > T_c$  to the system base temperature in an external magnetic field  $B_z^{\text{f.c.}} = 0.4$  mT, which we applied normal to the sample surface. The high pinning in YBCO allowed us to subsequently reduce the external magnetic field to zero while the vortices remained pinned in their original location. To image the resulting vortex distribution, we first performed a large-area iso-magnetic field image using our scanning NV magnetometer. To that end, we fixed the MW driving frequency  $\nu_{\text{MW}}$  to the zero-field NV-ESR frequency of  $\nu_{\text{ESR}} = 2.87$  GHz. Whenever a vortex was scanned below the NV, the vortex stray magnetic field shifted  $\nu_{\text{ESR}}$  away from  $\nu_{\text{MW}}$ , resulting in an increased NV fluorescence rate. Bright spots in Fig. 3.7a therefore signal the presence of individual vortices in the sample. Given our cooling-field of  $B_z^{\text{f.c.}} = 0.4$  mT and the magnetic flux-quantum  $\Phi_0$ , one expects a vortex-density  $B_z^{\text{f.c.}}/\Phi_0 = 0.19\mu\text{m}^{-2}$ , i.e. 43 vortices in our scan-range of  $15\mu\text{m} \times 15\mu\text{m}$  in fair agreement with the 31 vortices observed in Fig. 3.7a. The sample topography of the scan range is depicted in Fig. 3.7b. The position of the vortices in the inset is highlighted with circles to show the proximity to topographic defects.

Figure 3.7c shows a full, quantitative field map (see Sec. 2.1.4) of the section indicated in Fig. 3.7a. Interestingly, two vortices have different appearance in that the field in their center is considerably weaker. The position of these vortices is marked with a red circle in the topography image. The upper left, red encircled vortex sits

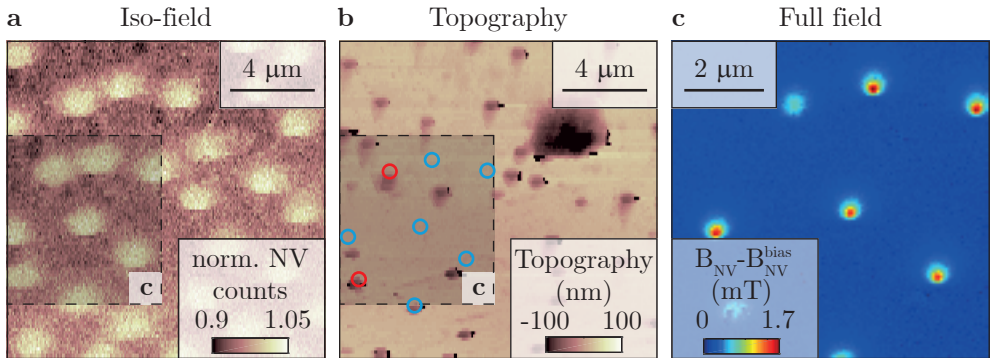


**Figure 3.7.: Ensemble vortex imaging.** **a** Iso-magnetic field image of an ensemble of vortices in sample A imaged at  $B = 0$  after field-cooling in  $B_z^{\text{f.c.}} = 0.4$  mT. The microwave driving frequency  $\nu_{\text{MW}}$  was fixed to the zero-field NV-ESR at 2.87 GHz, and NV fluorescence was monitored while scanning the sample. Bright areas indicate regions where the NV Zeeman shift exceeds the ODMR half linewidth of 6 MHz, that is, where  $B_{\text{NV}} > 0.22$  mT. The scan range of **c** is indicated by the dashed rectangle. **b** In-situ AFM of **a**. The location of the vortices in **c** is indicated with circles. Vortices marked with red circles sit close to some sample roughness which can lead to an increased NV sample distance. **c** Full field scan of the scan range indicated in **a** and **b**. Two vortices (at the upper left and lower left marked with a red circle in **b**) have a different appearance with possible reasons discussed in the text.

partially on some local topography elevation. Its field strength is clearly lower compared to other vortices, which is unexpected given that the magnetic flux for each vortex should be the same. Since we have not further investigated this phenomena at the time, we can only speculate on the cause of it. The most straightforward explanation for the weakened field is a locally elevated NV sample distance due to dirt on the YBCO surface (see topography map). In that case however, the spatial extent of the vortex should be larger than of the others due to upwards continuation (see Sec. 2.2.5). In contrast to that, the obscured vortex appears even smaller than the others.

A naive explanation is that this vortex is a full- $\Phi_0$  vortex that hopped between pinning sites. Then the flux of the vortex is proportional to the fraction of time the full vortex spend at that pinning site resulting in a smaller stray field and vortex size. However, this scenario can immediately be excluded owing to the nature of NV field measurements. Instead of measuring magnetic field directly, an ODMR spectrum at every pixel reveals only the NV-ESR resonance, which are subsequently converted to a magnetic field (see Sec. 2.1.4). For a hopping vortex we would then expect multiple resonance dips corresponding to the case with the vortex present and absent.

Another explanation would be a split vortex line. Instead of straight vortex, there could be a kink or horizontal shift of the vortex penetrating the superconductor. As shown in [83], this leads to the formation of two sub- $\Phi_0$  vortices, whose collective flux is equivalent to  $\Phi_0$ . Reference [83] reports on a maximal kink length of up to 10  $\mu\text{m}$ . In that scenario, there has to exist a second sub- $\Phi_0$  vortex, which could be found by scanning the area in the vicinity of the vortex.

It is also possible that the discussed vortex carries only half a flux quantum. Such half-integer flux vortices were theoretically predicted and experimentally confirmed in multiple cuprate superconductors [84–87]. Due to the  $d$ -wave symmetry of the superconducting order parameter, a vortex located on a tricrystal meeting point can acquire an addition  $\pi$ -shift of the wavefunction thereby satisfying the flux quantization of only  $\Phi_0/2$ . However, this effect has not been reported in a single crystal so far. We analyzed the magnetic flux of each vortex in Fig. 3.7c. Assuming the majority of

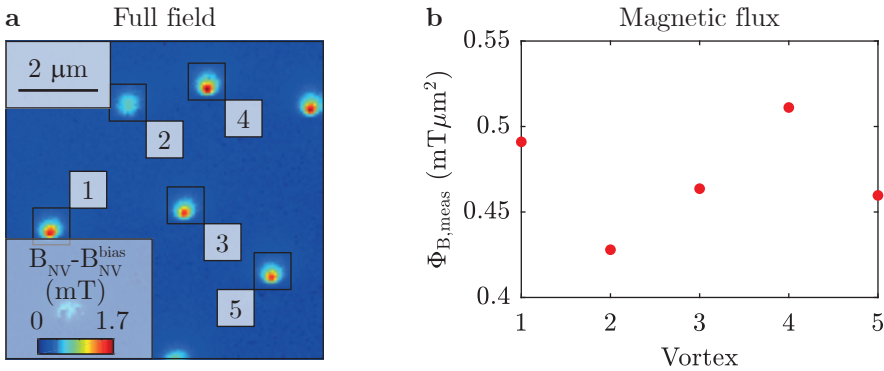


**Figure 3.8.: Magnetic flux.** **a** Full field scan of Fig. 3.7c with numbered vortices. **b** Magnetic flux of the respective rectangles in **a**. The field sum of vortex 2 is well above half the field sum of the  $\Phi_0$  vortices (1, 3-5).

observed vortices carry a flux  $\Phi_0$ , the flux of the upper left vortex has to be half the flux, which we could not confirm (see Fig. 3.8).

The field profile of the lower left vortex (visible below the colorbar panel in Fig. 3.7c) is clearly corrupted. Most likely this is due to a combination of dirt (clearly visible in Fig. 3.7b) and bad AFM performance, which compromised the corresponding ODMR traces and led to meaningless fits of the NV-ESR resonances.

Further insight of a  $\Phi_0$  vortex was gained by a high-resolution scan of an individual vortex. The vortex was nucleated as before and imaging was performed in a bias-field  $B_y^{\text{bias}} = 0.4$  mT, which we applied along the  $y$ -axis<sup>5</sup> to determine the sign of the measured fields (see Appendix A.2.2). We thereby chose  $B_y^{\text{bias}}$  strong enough to induce a sizable ESR splitting and weak enough not to generate in-plane vortices in the superconductor. The resulting image (Fig. 3.9a) yields a map of the projection of the vortex stray-field  $\mathbf{B}_{\text{vortex}}(x, y, z)$  onto the NV spin-quantization axis,  $\mathbf{e}_{\text{NV}} = (0, \sqrt{2}, 1)/\sqrt{3}$ . The outstanding stability of our cryogenic NV magnetometer further allows us to perform a full, three-dimensional mapping of  $\mathbf{e}_{\text{NV}} \cdot \mathbf{B}_{\text{vortex}}(x, y, z) = B_{\text{NV}}(x, y, z)$ . To that end, we released AFM feedback and scanned the sample at well-defined distances of  $z_{\text{tip}} = 50$  nm and 100 nm from the diamond tip. However,

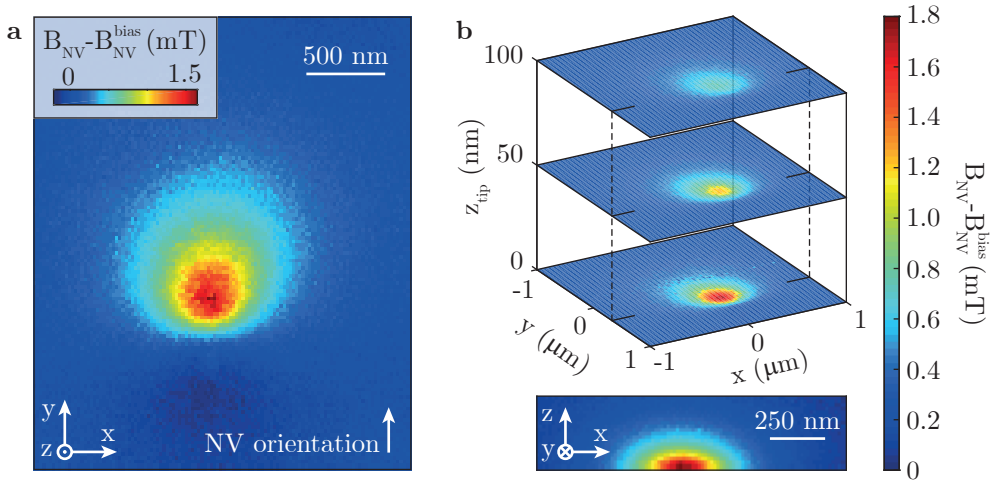


**Figure 3.9.: Quantitative mapping of single-vortex stray magnetic fields.** **a** Image of the magnetic stray field from a single vortex in sample A obtained with the NV magnetometer in AFM contact. The stray-field projection onto the NV axis was obtained by measuring the Zeeman splitting in the optically detected ESR at each of the  $120 \times 120$  pixels of the scan. The width of the observed vortex stray field is set by  $\Lambda$ , which is much bigger than our estimated spatial resolution of 30 nm (see main text). **b** Three-dimensional reconstruction of  $B_{\text{NV}}$  obtained as in **a**, with a different diamond tip. Scans were performed at two out-of-contact heights of 50 and 100 nm, as indicated. **c** Vertical scan through the vortex stray field in the  $x$ - $z$  plane indicated in **b**.

<sup>5</sup>We had to use an in-plane bias-field, as fields perpendicular to the sample are screened due to the Meissner effect.



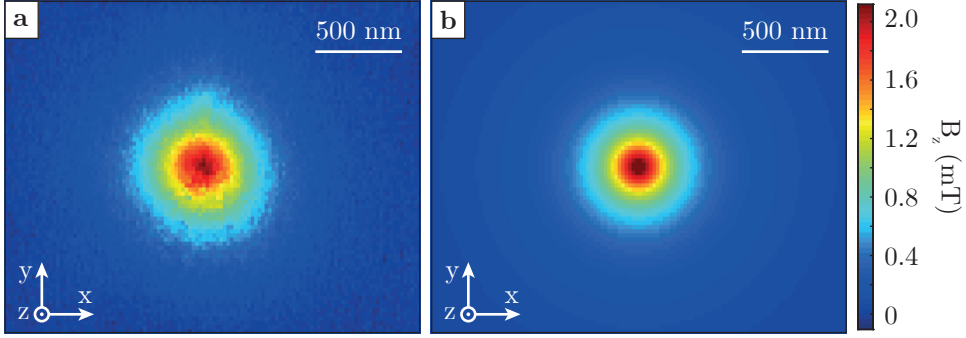


**Figure 3.10.: Vortex stray field maps used for flux estimation.** **a** Reconstruction of  $\mathbf{B}_z$  from  $\mathbf{B}_{\text{NV}}$  shown in Fig. 3.9a. The magnetic flux obtained by spatial integration is  $\Phi_{\text{B,meas}} \approx 1.00 \text{ mT}\mu\text{m}^2$ . **b** Simulation of  $\mathbf{B}_z$  using Eq. (3.13),  $\lambda_L = 249 \text{ nm}$  and  $h_{\text{NV}} = z_{\text{NV}} + d_{\text{cap}} = 30 + 60 \text{ nm} = 90 \text{ nm}$ . The flux enclosed by the scan range is  $\Phi_{\text{B,calc}} = 1.01 \text{ mT}\mu\text{m}^2$ .

the resulting slices of  $\mathbf{B}_{\text{NV}}(x, y, z = z_{\text{tip}})$  (Fig. 3.9b), together with an independently measured map of  $\mathbf{B}_{\text{NV}}(x, y, z)$  along an  $x/z$ -plane (Fig. 3.9c) provide no additional information about the stray magnetic fields, as reverse propagation already allows us to extract it from the data in Fig. 3.9a.

Our quantitative image allows us to directly determine the magnetic flux enclosed by the vortex in the scanning range and thereby test our data for consistency. The flux is given by

$$\Phi_{\text{B,meas}} = \iint B_z dx dy \approx 1.00 \text{ mT}\mu\text{m}^2, \quad (3.9)$$

where we obtained the  $z$ -component of the magnetic field by applying Eq. (2.30) to the data in Fig. 3.9a. Importantly, the measured flux  $\Phi_{\text{B,meas}}$  is  $\sim 2\times$  smaller than  $\Phi_0$ , which can readily be explained by the finite integration area of our data set (Fig. 3.10a). For comparison, we numerically evaluated the integral in Eq. (3.9) also for the Carneiro model Eq. (3.13) of a vortex (see Fig. 3.10b) over the same finite area. We obtained a flux of  $\Phi_{\text{B,calc}} = 1.01 \text{ mT}\mu\text{m}^2$ , which is in very good agreement with our data.

A central distinguishing feature of NV magnetometry is its ability to provide quantitative measures of magnetic fields on the nanoscale. Here, this feature allows us to determine the local properties of our superconducting sample, i.e. the London penetration depth, and to test and discriminate three existing models for vortex stray fields, which are described in the following. We conducted separate, high-resolution line scans of  $\mathbf{B}_{\text{vortex}}(x, y, z)$  along the two symmetry axes of an individual vortex (nucleated by field cooling in  $B_z^{\text{f.c.}} = 0.2 \text{ mT}$ ) in sample B. The resulting measurements of  $\mathbf{B}_{\text{vortex}}(x)$  and  $\mathbf{B}_{\text{vortex}}(y)$  (Fig. 3.11a,b, respectively) form the basis for our subsequent, quantitative analysis.



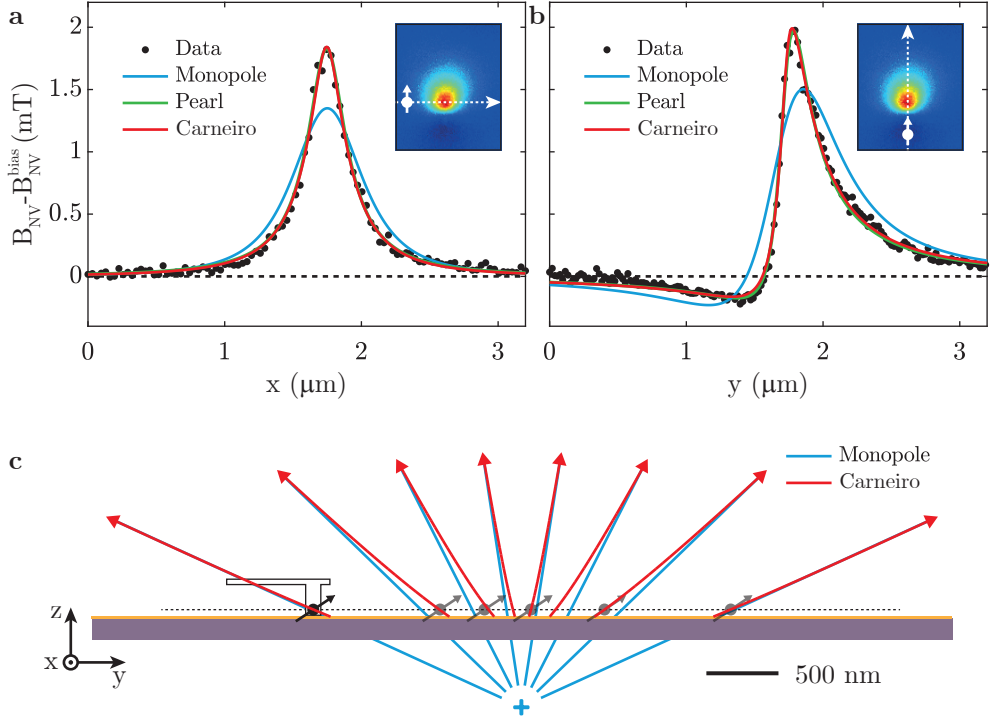


**Figure 3.11.: Quantitative stray-field analysis and determination of London penetration depth.** **a, b** High-resolution measurements of the vortex stray field  $B_{\text{NV}} - B_{\text{NV}}^{\text{bias}}$  recorded in sample B along the horizontal ( $x$ ) and vertical ( $y$ ) symmetry axes of a single vortex, as shown in the insets. Blue, green and red lines represent best fits to the monopole model, Pearl and the Carneiro model, respectively. From the Pearl and Carneiro model fit, we determine  $\lambda_L \approx 250$  nm, the bulk London penetration depth, which cannot be obtained unambiguously using the monopole model. **c** Calculated vortex magnetic field lines close to the superconductor surface with the monopole approximations (blue) and Carneiro model (red), illustrating the strong discrepancy between the two models close to the surface ( $z_{\text{NV}} < \Lambda$ ). The purple (golden) strip indicates the YBCO thin film (capping layer). In all panels, the black/white arrow shows the orientation of the NV with respect to the sample.

For superconductors deep in the type-II limit, the coherence length  $\xi$  is marginal compared to the London penetration depth  $\lambda_L$  and is usually neglected in the calculation of the vortex stray field. Therefore, it is sufficient to solve the London equations for the superconducting currents inside the superconductor in the presence of an external magnetic field and subsequently apply Biot-Savart's law to derive the stray fields. For infinitely large superconductors general solutions of the London theory for the stray field have been given [75] and at large distance from the superconductor ( $z_{\text{NV}} \gg \lambda$ ) resemble the field of a magnetic monopole [67, 68] of strength  $2\phi_0$  located

at  $z = -\lambda$

$$\begin{aligned} B_z(r, z_{\text{NV}}) &= \frac{\phi_0}{2\pi} \frac{\lambda + z_{\text{NV}}}{[r^2 + (\lambda + z_{\text{NV}})^2]^{3/2}}, \\ B_r(r, z_{\text{NV}}) &= \frac{\phi_0}{2\pi} \frac{r}{[r^2 + (\lambda + z_{\text{NV}})^2]^{3/2}}. \end{aligned} \quad (3.10)$$

Although the monopole approximation is widely used in literature [62, 88–90], it has the drawback that it does not allow an independent determination of  $\lambda$  and  $z_{\text{NV}}$  (that is, changes in  $\lambda$  cannot be distinguished from changes in  $z_{\text{NV}}$ ), and that it breaks down for  $z_{\text{NV}} \ll \lambda$ . This can be nicely seen in Fig. 3.11c. We computed field lines of a monopole (blue lines) and field lines of an analytical solution (red lines) of the London equations (described later). For large  $z$ -values the field lines of both models overlap and both will give the same result. However, close to the surface we observe distinct differences between the two. Hence, in our attempts to fit the data (keeping  $\mathbf{e}_{\text{NV}}$  and  $\Phi_0$  fixed and varying the vortex position), the monopole failed to yield a satisfactory fit (Fig. 3.11a,b, blue lines). This discrepancy is a consequence of the close proximity of the NV to the sample and is an opportunity to test the validity of more refined models for vortex stray fields.

Analytical solutions of the stray fields for superconductors in the thin film limit  $d \ll \lambda_L$  was first derived by J. Pearl assuming a homogeneous current distribution along the thickness of the film and applying the London equations. The magnetic field outside the superconductor is given by the rotation of the vector potential  $\mathbf{A}$ , which can be expressed as [67, 91]

$$\mathbf{A}_\varphi(r, z_{\text{NV}}) = \frac{\Phi_0}{2\pi} \int_0^\infty \frac{J_1(qr) e^{-q|z_{\text{NV}}|}}{1 + \Lambda q} dq, \quad (3.11)$$

where  $J_1(x)$  is a Bessel function. Pearl discovered that the London penetration depth increases to an effective London penetration depth  $\Lambda$  due to the restriction of the screening currents to the finite thickness  $d$

$$\Lambda = \frac{\lambda_L^2}{d}. \quad (3.12)$$

Fits to the Pearl vortex<sup>6</sup> (Fig. 3.11a,b, green lines) indeed show good quantitative agreement. Importantly, and in contrast to the monopole approximation, this fit, paired with the high signal-to-noise ratio of our data, allows us to independently determine  $\lambda_L$  and  $h_{\text{NV}}$ , the vertical distance between the NV and the vortex. To our knowledge, this is the first time such an independent determination of these quantities has been done in a vortex imaging experiment [29, 62, 92]. From the fit, we find  $\Lambda = 840 \pm 20$  nm and  $h_{\text{NV}} = 104 \pm 2$  nm. Here,  $h_{\text{NV}}$  is related to the net NV-to-sample standoff distance  $z_{\text{NV}} = h_{\text{NV}} - d_{\text{YBCO}}/2 - d_{\text{cap}} = 9 \pm 3.5$  nm, where we assumed the 2D Pearl vortex in the middle of the thin film. Our measurement of  $\Lambda$  yields a bulk penetration depth of  $\lambda_L = 251 \pm 14$  nm, which is consistent with previously reported values [62, 93] and provides proof of the validity of our model and method.

---

<sup>6</sup>For the numerical implementation of Eq. (3.11) see Appendix A.2.3.1

Although the Pearl model provides a good fit to the data, it cannot be fully appropriate since the condition  $d \ll \Lambda$  required for Pearl's solution is not strictly fulfilled. A better suited model, which does not suffer from this limitation, is the Carneiro model as it describes a vortex in a thin film correctly. This model is an analytical solution of the stray fields for an arbitrarily thick superconducting film filling the space  $-d \leq z \leq 0$  at  $z_{\text{NV}} > 0$ . The vortex stray field is given by [68]

$$\begin{aligned} B_z(r, z_{\text{NV}}) &= \frac{\phi_0}{2\pi\lambda_L^2} \int_0^\infty dk \frac{k J_0(kr)}{k^2 + \lambda_L^{-2}} f(k, z_{\text{NV}}) \\ B_r(r, z_{\text{NV}}) &= \frac{\phi_0}{2\pi\lambda_L^2} \int_0^\infty dk \frac{J_1(kr)}{k^2 + \lambda_L^{-2}} g(k, z_{\text{NV}}), \end{aligned} \quad (3.13)$$

with

$$\begin{aligned} f(k, z) &= c_1 e^{-kz} \\ g(k, z) &= c_1 k e^{-kz}, \end{aligned} \quad (3.14)$$

and

$$\begin{aligned} c_1(k) &= [(k + \tau)e^{\tau d} + (k - \tau)e^{-\tau d} - 2k] \frac{\tau}{c_2} \\ c_2(k) &= (k + \tau)^2 e^{\tau d} - (k - \tau)^2 e^{-\tau d}, \end{aligned} \quad (3.15)$$

where  $r = \sqrt{x^2 + y^2}$ ,  $k = \sqrt{k_x^2 + k_y^2}$ ,  $\tau = \sqrt{k^2 + \lambda_L^{-2}}$  and  $J_0(x)$  and  $J_1(x)$  are Bessel functions. We fitted the data to the Carneiro model<sup>7</sup> (Eq. (3.13)) and again obtained excellent agreement (Fig. 3.11a,b, blue lines). From the fit, we extracted  $\lambda_L = 249.4 \pm 3.1$  nm and  $h_{\text{NV}} = 51.2 \pm 2.4$  nm. Our measurement of  $\lambda_L$  yields an effective penetration depth of  $\Lambda = 829 \pm 31.9$  nm. The NV standoff distance is given by  $z_{\text{NV}} = h_{\text{NV}} - d_{\text{cap}} = 31 \pm 2.5$  nm (see Fig. 3.6a). For samples without a capping layer,  $z_{\text{NV}}$  thus represents the ultimate imaging resolution we can currently achieve with our magnetometer.

---

<sup>7</sup>For the numerical implementation of Eq. (3.13) see Appendix A.2.3.2

### 3.3. Summary and outlook

In this chapter we have presented the first demonstration of a scanning NV magnetometer operating under cryogenic conditions. We have combined nanoscale spatial resolution and quantitative, non-invasive magnetic imaging to map the stray magnetic fields of individual vortices in superconducting thin films of YBCO.

The analysis of our experimental data provides an example of the great potential that the quantitative aspects of NV magnetometry hold for future applications in studying complex condensed matter systems. For instance, the determination of the absolute value of  $\lambda_L$  is notoriously hard to achieve [94], but of high interest due to its direct link to the structure of the superconducting gap [95] and density of superconducting electrons [75]. Various measurement tools like magnetic susceptibility techniques [95–97], transmission and spectroscopy techniques [98, 99] or muon spin resonance [100] have been developed but they mostly only measure relative changes of  $\lambda_L$  or are bulk measurements that do not allow for measurements of spatial inhomogeneities of the penetration depth. Our quantitative fits have allowed us to locally determine the absolute value of  $\lambda_L$  without any assumptions on the sensor sample distance. Furthermore, our analysis has allowed us to draw a clear distinction between alternative models for vortex stray fields and we have for the first time experimentally proven that the monopole approximation fails to predict the vortex stray field at close proximity.

The non-invasiveness of the probe is a key requirement and warrants discussion of the potential unwanted heating effects due to NV laser excitation and microwave driving. For YBCO, we repeated vortex imaging with increasing laser powers (100  $\mu$ W to 1 mW), and even with the highest values of 1 mW (see Fig. 3.12) we were able to image vortices without observing signs of “vortex dragging” [62]. The data presented previously in this chapter was taken at a typical laser excitation of 100  $\mu$ W. The heat load on the sample can be further reduced by one of many strategies. Specifically, resonant optical excitation of the NV center [101] would require no more than a few nW of laser excitation, all-optical spin manipulation [102] could eliminate microwaves and pulsed ODMR driving and detection [44] could lead to laser duty cycles  $< 1\%$ .

While YBCO has very strong vortex pinning and a high critical temperature, prospects for studying more fragile superconductors are excellent. For instance, most type-I superconductors<sup>8</sup> have a critical temperature below 10 K. A simplified phase diagram, in which a type-I superconductor turns normal conducting above a critical field, was shown in Fig. 3.3a. In reality, demagnetization effects can lead to an effective increase of the external magnetic field exceeding the critical field at the edge of a sample. As long as the external field is not greater than critical field, the sample cannot turn completely to a normal conductor. Therefore, superconducting and normal conducting regions coexist in the so-called intermediate state. Due to flux quantization (see Appendix A.2.1), the normal domain can be considered an agglomeration of  $\Phi_0$  vortices. The competition between short-range attractive interaction due to the positive surface energy and the long-range repulsive magnetic interaction due to the stray fields lead to the formation of giant vortices and stripes in the intermediate state [90, 103].

Two-component superconductors like  $\text{MgB}_2$  with a critical temperature of  $T_c =$

---

<sup>8</sup>Lead  $T_c = 7$  K, Niobium  $T_c = 9.2$  K, Technetium  $T_c = 7.5$  K, Vanadium  $T_c = 5.4$  K

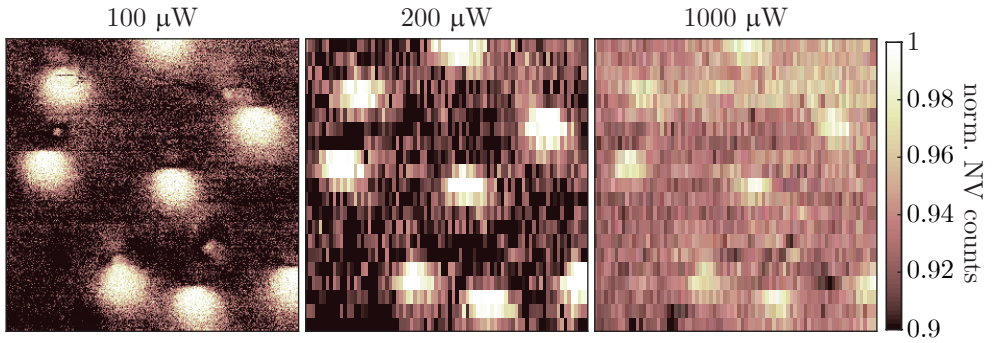


**Figure 3.12.: Non-invasiveness of NV magnetometry.** Iso-magnetic field image taken at increased laser powers (see labels) on an ensemble of vortices in sample A. The vortices were imaged at  $B = 0$  mT after field-cooling in  $B_z^{\text{f.c.}} = 0.4$  mT. No “vortex dragging” was observed up to 1 mW. Imaging contrast deteriorates for increasing laser power due to the reduction of ODMR contrast with excitation power [44].

38.2 K [104] are also very interesting to study. So-called type-1.5 superconductors consist of two condensates each with their own characteristic coherence length  $\xi_{1,2}$  [105]. This can lead to a semi-Meissner state, where vortex clusters and Meissner areas exist at the same time.

At low enough fields, the Meissner state also exist in type-II superconductors and multiple experiments of NV ensembles on YBCO in the Meissner state have been published [66, 106–109]. The disadvantage of ensemble NV magnetometry is its diffraction limited resolution. Therefore in a first attempt, we imaged nanoscale Meissner screening fields above a  $6 \mu\text{m}$  wide disk in YBCO sample B (see Fig. 3.13a) [61]. To that end, we applied an external bias field of  $B_z^{\text{bias}} = 1.7$  mT perpendicular to the sample surface. Using the second London equation (Eq. (3.2)) we numerically calculated the current density  $J$  induced in the disk. We deduced the stray field outside the superconductor using Biot-Savart’s law, which we fitted to our data. From this we could obtain a fitted London penetration depth of  $\lambda_L = 249 \pm 5$  nm in excellent agreement with the vortex fitting. Further we applied the reverse propagation method (Eq. (2.51) and Eq. (2.52)) to reconstruct the screening supercurrents circulating in the sample (see Fig. 3.13b), which are strongest on the edge and decay towards the center on the length scale of the London penetration depth  $\Lambda$ .

A variety of interesting physics is provided by nanostructuring of superconductors to tweak superconducting properties. This allows for the modification of the superconducting order parameter, critical superconducting parameters ( $J_c$ ,  $H_c$ ) and leads to novel vortex phases like the formation of anti-vortices, which preserve the symmetry of a sample in a square or triangular shape [110]. Further, artificially introduced pinning sites are of high relevance for technology as they extend the maximal critical current up to its theoretical limit of the depairing current [111, 112]. Nanostructured superconductors can also be used as toy models for other physical systems like frustrated spin systems. These so-called spin-ices are magnetic systems, in which no minimal energy state exists and the interaction energy between neighboring spins cannot be simultaneously minimized. Spin-ice systems are naturally found in water ice [113]

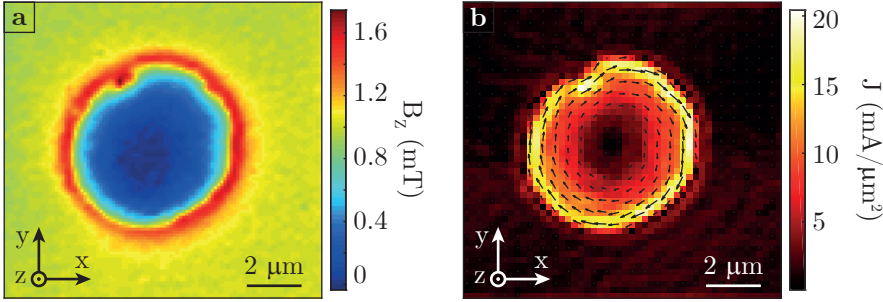


**Figure 3.13.: Meissner screening of a superconducting thin-film disk.**

**a** Quantitative map of the magnetic field  $B_z$ , measured with the scanning NV spin above the YBCO disk in an external magnetic field of 1.7 mT applied perpendicular to the sample. Low magnetic fields are observed in the center of the disk due to Meissner screening in the superconductor and maximal fields at the edges of the disk due to compression of the field lines expelled from the disk. We transformed the measured  $B_{\text{NV}}$  (see Appendix Fig. A.6) to  $B_z$  using Eq. (2.30). The data was acquired with a pixel dwell-time of 12 s, resulting in a scan time of 8 h for the entire scan. **b** Current density  $J$ , reconstructed by magnetic field reverse propagation from the data in **a**. The circular currents generate a magnetic field counteracting the external magnetic field. The current reconstruction reveals the position and shape of a region in the sample where superconductivity is suppressed and the current therefore deviates from the circular shape of the disk. Signatures of this were already visible in **a**, but we now visualise it more directly through the impact it has on the current flow in the superconductor. While further studies are required to assess the origin of this feature in  $J$ , we speculate that it may either constitute a vortex trapped at the edge of the YBCO disk or a defect connected to material impurities introduced during growth or micro-patterning.

but bear also the potential of useful applications in spintronics such as energy and memory storage or logic devices [114–116]. A prototypical implementation of artificial spin-ice are single-domain ferromagnetic islands with four islands meeting in a vertex [117]. However, these materials suffer from relatively weak magnetic interaction, which make a long-range ordered ground state very difficult to realize. Superconducting vortices positioned on double-well pinning sites in a square or kagome lattice with few micrometer lattice constants have been proposed as another very suitable candidate to mimic spin-ice behavior [118]. They exhibit strong, long-range coupling and various geometries of spin-ice lattices can readily be designed and implemented using antidot (holes) arrays with locally suppressed superconductivity. The vortex density can be tuned by magnetic fields and vortex-interaction can be controlled with temperature [119] (see Fig. 3.14a and b), whose analog is not possible in ferromagnetic island systems. While the spin-ice ground state in a square lattice is “two-in, two-out” ( $T_1$  in Fig. 3.14c), 14 higher energetic defect states [120] exist ( $T_2$ ,  $T_3$  and  $T_4$  in Fig. 3.14c), whose abundance can be conveniently investigated in this system. A main difficulty in the study of spin-ice systems arises from probing the spins without altering their interaction and state. Therefore NV magnetometry is particularly

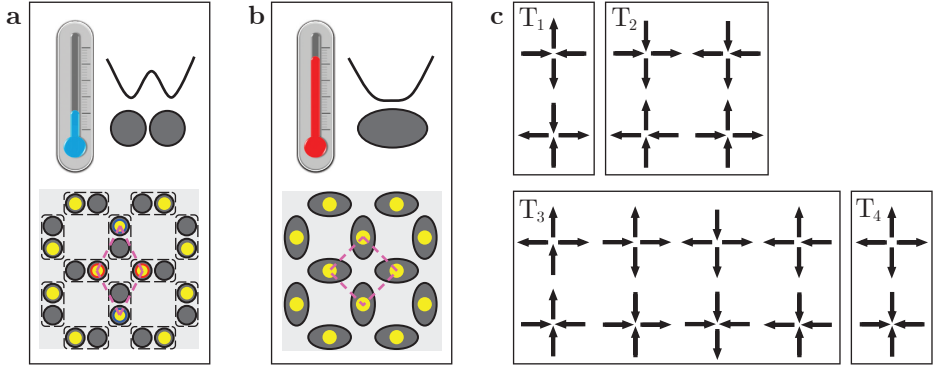


**Figure 3.14.: Vortex-ice system in a square lattice antidot array.** **a** The lower panel shows the square lattice of antidots. Two antidots each (highlighted with the dashed rectangles) serve as a double-well pinning site for vortices. The antidots are arranged in a square lattice with four pinning sites meeting at a vertex. At half matching field every double-well is occupied with a single vortex (yellow circle), which leads to frustration at every vertex. In the schematic the spin-ice follows the ice rule [113] with “two-in, two-out” at every vertex. **b** At elevated temperatures the energy barrier of the double-well is washed out, geometric frustration is thermally switched off and vortices position with constant inter-vortex distances. **c** All 16 possible square ice configurations grouped by increasing energy. The arrows span over the double-well and point from an empty to and an occupied antidot. Figures **a** and **b** are adapted with permission from [119], Springer Nature. Figure **c** is adapted with permission from [120], Springer Nature.

suitable, as it is non-invasive and allows for the investigation over a large temperature range and the observation of freezing and thawing of the artificial spin ice.

In conclusion, scanning NV magnetometry is a new technology that offers a set of unique capabilities that can be readily applied to address open questions in superconductivity and beyond. Nanoscale spatial resolution, vector-magnetometry and especially the wide temperature range from millikelvin to room temperature allows for studying temperature dependent parameters like the coherence length or penetration depth close to the critical temperature, even for high-temperature superconductors. In addition the AC sensing capabilities up to the GHz range through spin relaxometry [22] or dynamical decoupling [121] is another exciting avenue to access dynamical properties like vortex motion [122, 123], which is the dominant source of dissipation and, hence, a major challenge for industrial applications.





## 4. Two-dimensional magnetic systems

In the previous chapter we examined magnetic stray fields generated by superconducting currents. In this chapter we discuss the second source of magnetic stray fields: materials with inherent magnetization. Magnetic materials are of high relevance for application in technology ranging from recording media, motors, actuators, sensors or holding devices to very simple fridge magnets. Research and development of new magnetic materials has led to improvements in device efficiency, as well as a reduction of their sizes crucial for instance for high density magnetic memory media. So far the size of magnetic material was mostly shrunk laterally, while researches recently discovered the first two-dimensional magnetic material. Advancing the understanding and applications of those 2D magnets requires methods to quantitatively probe their magnetic properties on the nanoscale.

In this chapter we present the study of atomically thin crystals of the van der Waals magnet chromium triiodine ( $\text{CrI}_3$ ) down to individual monolayers and demonstrate quantitative, nanoscale imaging of magnetization, localized defects, and magnetic domains. We determine the magnetization of  $\text{CrI}_3$  monolayers to be  $\approx 16 \mu_B/\text{nm}^2$  (with  $\mu_B$  the Bohr magneton) and find comparable values in samples with odd numbers of layers, whereas the magnetization vanishes when the number of layers is even due to an antiferromagnetic interlayer exchange coupling. We also establish that the unexpected even-odd effect is intimately connected to the material structure, and that structural modifications can induce switching between ferro- and antiferromagnetic interlayer ordering. Besides revealing new aspects of magnetism in atomically thin  $\text{CrI}_3$  crystals, these results demonstrate the power of single-spin scanning magnetometry for the study of magnetism in 2D van der Waals magnets. The presented results have been published in [55].

### 4.1. Motivation: 2D magnetic materials

Since the first exfoliation of graphene [124] researchers have witnessed an ever-growing diversity of two-dimensional materials. They range from insulators like h-BN [125–127] or perovskites [128] to semiconductors like  $\text{MoS}_2$  [129, 130], and metals like  $\text{WTe}_2$  [131]. These materials feature high mechanical strength and high electronic quality, and they display interesting electronic ordering phenomena, including superconductivity [132], charge density waves [133], and ferroelectricity [134]. The family of two-dimensional materials is already so numerous that researches have provided a computational database [135] indicating elastic, electronic, magnetic, optical, structural, and thermodynamic properties of over 3000 compounds and structures.

Not only are these materials interesting from a fundamental research aspect because most of them feature completely different properties than their three-dimensional counterparts. For example  $\text{MoS}_2$  is an indirect band gap semiconductor, while its

monolayer equivalent has a direct bandgap [129]. Additionally, one can also stack them on top of each other layer by layer. The atoms within a single layer are covalently bonded to each other, while adjacent layers are held together by van der Waals forces, which is why such stacks are called *van der Waals heterostructures*. Similar to playing with Legos, stacking different 2D materials into heterostructures enables us to create materials almost by design. This led to new applications ranging from field-effect tunneling transistors [136] to optoelectronic devices [137, 138], photodetectors [139], photovoltaic application [140] and light emitting diodes [141].

All of these mentioned applications have one thing in common: Their working principle does not require magnetism and the reason is magnetic layers simply were not discovered until recently. Only two years ago, in 2017, two-dimensional materials with intrinsic ferromagnetism were discovered at low [142, 143] and room temperatures [144]. As we will see later, ferromagnetism in two-dimensional materials is theoretically forbidden by the Mermin-Wagner theorem [145] under certain constraints. It states that in spin rotational invariant systems with short-range order below three dimensions, long-range order in the system are prohibited due to spin fluctuations induced by thermally excited magnons. Luckily, anisotropy can lift the Mermin-Wagner theorem allowing for ferromagnetic ordering in 2D materials with sufficient magnetic anisotropy. Their discovery triggered the development of spintronic devices like spin filters [146, 147], spin-transistors [148], tunneling magnetoresistance devices [149, 150] and magneto electric switches [151–153].

Although magnetic two-dimensional materials continue to produce interesting results, further advances in the field hinge on developing methods for the quantitative study of the magnetic response of these atomically thin crystals at the nanoscale. Despite their central importance, the required experimental methods are still lacking. Indeed in the case of one prominent two-dimensional ferromagnet,  $\text{CrI}_3$ , transport experiments [146–149, 151, 152] probe magnetic properties only indirectly. The only existing, spatially resolved studies rely on optical techniques, such as fluorescence [154, 155] or the magneto-optical Kerr effect (MOKE) [142, 143, 156], and are therefore limited in spatial resolution to the micron-scale. Even more critically, these techniques do not provide quantitative information about the magnetization and are susceptible to interference effects that can obscure magnetic signals in thin samples [142].

The following chapters demonstrate that we overcome these limitations and address the nanoscale magnetic properties of van der Waals magnets. Specifically, we illustrate how an NV sensor can be used to probe magnetism in the aforementioned compound  $\text{CrI}_3$ .

## 4.2. $\text{CrI}_3$ – a ferromagnetic 2D material

Chromium triiodine ( $\text{CrI}_3$ ) is an indirect bandgap semiconductor [157] and belongs to the group of chromium trihalides with compound formula  $\text{CrX}_3$  ( $\text{X} = \text{F}, \text{Cl}, \text{Br}$  and  $\text{I}$ ). While bulk  $\text{CrCl}_3$  is an antiferromagnet with a Néel temperature of 16.8 K [158], both bulk  $\text{CrBr}_3$  and  $\text{CrI}_3$  are ferromagnets with Curie temperatures of 37 K [159] and 68 K [160], respectively. Bulk  $\text{CrI}_3$  is a layered, planar structure and the direction of its magnetic moments is perpendicular to the  $\text{CrI}_3$  planes [161].

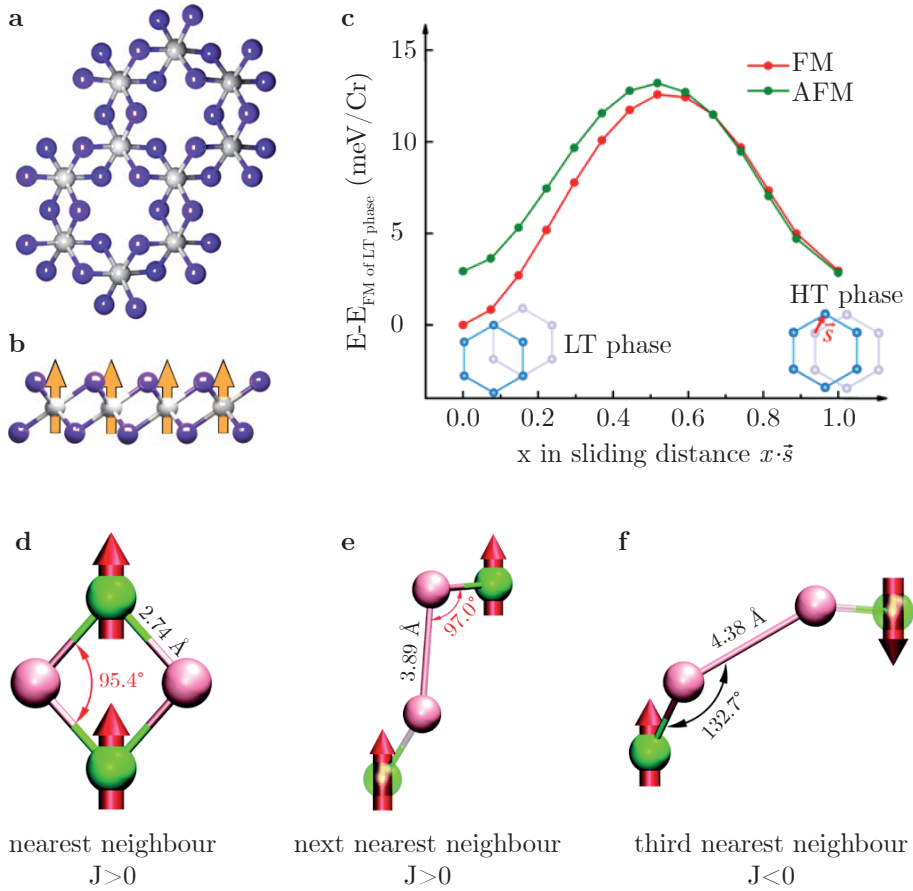


**Figure 4.1.: Structure and exchange interactions of  $\text{CrI}_3$ .** **a** Top-view of a single-layer of  $\text{CrI}_3$ . Chromium ions (gray balls) are arranged in a honeycomb lattice and coordinated by edge-sharing octahedra with six iodine atoms (purple balls). **b** Side-view of  $\text{CrI}_3$  indicating the out-of-plane magnetization of  $3 \mu_B$  located on each chromium ion. **c** Connection between interlayer magnetic coupling as a function of stacking order from the high-temperature (HT) phase of bilayer  $\text{CrI}_3$  to the low-temperature (LT) phase. The insets show the stacking order of the bilayer in the respective phases. In the HT phase, the magnetic ground state is antiferromagnetic (A-FM), while the magnetic ground state at low temperatures is ferromagnetic (FM). **d** Ferromagnetic superexchange interaction of two chromium ions (green balls) via an iodine atom (pink ball). **e** Ferromagnetic superexchange interaction to the next nearest neighbor of a chromium ion. **f** The exchange interaction with the third nearest neighbor chromium is antiferromagnetic.  $J$  is the exchange constant. Figure **a** and **b** are adapted with permission from [142], Springer Nature. Figure **c** is adapted from [162]. Figure **d-f** are adapted from [157].

The structure of a monolayer of  $\text{CrI}_3$  is shown in Fig. 4.1a (top-view) and **b** (side-view). In a single layer of  $\text{CrI}_3$ , the chromium ions form a honeycomb lattice and are sandwiched between two planes of iodine atoms. The chromium ions are surrounded by six iodine atoms arranged in a corner-sharing octahedra. Chromium's neutral electron configuration is  $[\text{Ar}] 4s^1 3d^5$ . In  $\text{CrI}_3$  the oxidation of chromium is +3 yielding  $[\text{Ar}] 4s^0 3d^3$ . The three  $d$ -electrons are filled according to Hund's rule and give an out-of-plane magnetic moment of  $3 \mu_B$  per chromium ion, which results in a 2D magnetization of  $\sigma_z^{\text{mono}} = 14.7 \mu_B/\text{nm}^2$ . Bulk  $\text{CrI}_3$  crystallizes in a monoclinic structure at room temperature and undergoes a crystallographic phase-transition to a rhombohedral structure near 210 – 220 K upon cooling down from room temperature [160]. The structural change corresponds to a different stacking order. As can be seen in the insets of Fig. 4.1c, the low temperature (LT) phase is AB stacked with the Cr ion of the upper layer centered on the hexagon of the lower layer. The high temperature (HT) phase is obtained by shifting the lower layer by the vector  $\vec{s}$ . As we will see later, this stacking order has a severe impact on the magnetic interlayer coupling.

In the following, we will present a theoretical proposal to exfoliate 2D magnets from ferromagnetic  $\text{CrI}_3$  bulk. We will then introduce the Mermin-Wagner theorem that rules out magnetic order in two-dimensional materials under certain constraints. Fortunately, the theoretical proposal addresses this potential issue and shows that anisotropy exists in monolayer  $\text{CrI}_3$  that lifts the Mermin-Wagner theorem and allows for a magnetic ground state. After discussing the microscopic origin of the anisotropy, we review the first experimental evidence of magnetic signal in atomically thin  $\text{CrI}_3$  as well as the surprising finding of antiferromagnetic interlayer coupling. Finally, we give a theoretical explanation for this coupling.

Until the year 2015, little attention has been paid the ferromagnetic bulk material  $\text{CrI}_3$ . Then Zhang *et al.* [157] published a theoretical paper predicting the feasibility of exfoliating bulk  $\text{CrI}_3$  at room temperature to obtain a two-dimensional ferromagnet, which did not exist at that time. They showed that the cleavage energy that the exfoliation process must overcome is only slightly higher than for graphite, as is the in-plane stiffness that is needed for the flake to withstand its own weight and to avoid curling at the edges. Their ab initio molecular dynamics simulation revealed that the flake is thermally stable at room temperature.

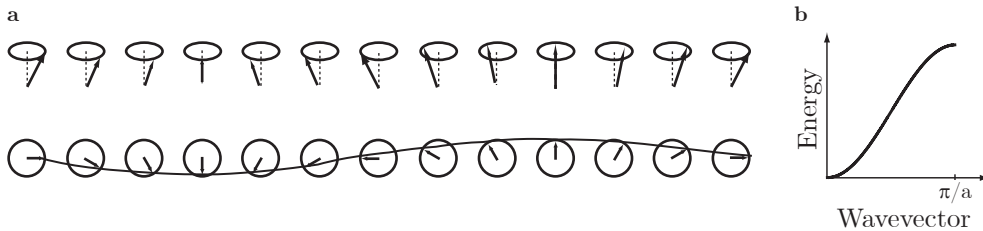


**Figure 4.2.: Spin-wave illustration and typical dispersion relation.** **a** Illustration of a spin-wave. Top panel (bottom panel) is a side view (top view), respectively. **b** Spin-wave dispersion for a chain of atoms. The energetic cost for a long-wavelength spin-wave is extremely low. The figure was adopted from [163].

However, even if one would succeed in exfoliating CrI<sub>3</sub>, the Mermin-Wagner theorem states that “at any nonzero temperature, a one- or two-dimensional isotropic spin-S Heisenberg model with finite-range exchange interaction can be neither ferromagnetic nor antiferromagnetic” [145]. Mermin and Wagner assumed the rotationally symmetric Heisenberg model of the form

$$\hat{\mathcal{H}} = -2 \sum_{ij} \mathcal{J} \hat{\mathbf{S}}_i \cdot \hat{\mathbf{S}}_j, \quad (4.1)$$

where  $\mathcal{J}$  is the exchange constant and  $\hat{\mathbf{S}}$  the dimensionless spin operators. It describes how strongly multiple spins interact with each other. The strength of the interaction is determined by the exchange constant  $\mathcal{J}$  and the angle between the different pairs of spin vectors. In this case, the dispersion relation of spin-waves or magnons – elementary excitations from the ferromagnetic ground state (Fig. 4.2a) – is proportional to the square of the wavevector (see Fig. 4.2b). Therefore in a system with continuous symmetry, there are always gapless excitations possible, and Mermin and Wagner showed that the thermal magnon occupation number in one and two dimensions at finite temperature excited diverges [163], which destroys long-range order. Luckily, anisotropy can break spin-rotational invariance, which adds an initial energy cost to tilt spins out of their equilibrium position. This opens up a gap in the spin-wave spectrum that avoids the divergence. Hence, 2D materials with an anisotropy are theoretically allowed to show long range magnetic order.

The consequence of Mermin’s and Wagner’s prediction required for Zhang *et al.* [157] to look for such an anisotropy of the spin Hamiltonian for single layer CrI<sub>3</sub>. They found a relevant anisotropy term, which renders ferromagnetic intralayer coupling the most stable configuration. To that end, they calculated the nearest, next nearest, and third nearest neighbor exchange interactions as indicated in Fig. 4.1d-f. For the nearest neighbor interaction (Fig. 4.1d) they found a competition between an antiferromagnetic (A-FM) direct exchange and a ferromagnetic (FM)<sup>1</sup> superexchange via the iodine atom. Due to the large Cr-Cr distance of 4.05 Å, the superexchange energy exceeds direct exchange making the nearest neighbor exchange interaction ferromagnetic ( $\mathcal{J} > 0$ ). The cation-anion-anion-cation (Cr-I-I-Cr) superexchange of the next nearest neighbor and third nearest neighbor can be reduced to a cation-anion-cation superexchange [164], where one can apply again the Goodenough–Kanamori–Anderson rule<sup>2</sup>. One finds that the next nearest neighbor interaction is ferromagnetic ( $\mathcal{J} > 0$ ) while the third nearest neighbor interaction is antiferromagnetic ( $\mathcal{J} < 0$ ). In summary, the result of Zhang *et al.* suggested robust long-range order within monolayer CrI<sub>3</sub>.

In 2017, J.L. Lado and J. Fernández-Rossier [165] investigated the microscopic origin of the magnetic anisotropy and confirmed anisotropic symmetric superexchange as the predominant source. They postulated a model Hamiltonian

$$\hat{\mathcal{H}} \approx - \left( \mathcal{J} \sum_{i,j} \hat{\mathbf{S}}_i \cdot \hat{\mathbf{S}}_j + \sum_i D (\hat{S}_i^z)^2 + \lambda \sum_{i,j} \hat{S}_i^z \hat{S}_j^z \right), \quad (4.2)$$

<sup>1</sup>The Goodenough–Kanamori–Anderson rule [164] states that the superexchange interaction is angle dependent. A 180° superexchange is antiferromagnetic, while a 90° superexchange is ferromagnetic in nature.

<sup>2</sup>See footnote 1.

where the first term describes Heisenberg isotropic exchange, the second single ion magnetic anisotropy originating from the interplay of spin-orbit coupling and crystal field and the third anisotropic symmetric superexchange, respectively. Using DFT calculations and spin-wave theory, they concluded that anisotropy due to the anisotropic superexchange gives rise to a spin-wave gap of

$$\Delta_0 = 3D + 9\lambda/2, \quad (4.3)$$

which stabilizes ferromagnetic order, thereby confirming the finding of Zhang *et al* [157]. While the authors find that the single ion anisotropy is negligible ( $D \approx 0$ ), the main contribution to anisotropy comes from anisotropic, symmetric superexchange ( $\lambda = 0.09$  meV). Note that these results are controversial and the correct Hamiltonian describing  $\text{CrI}_3$  is still under debate.

After it was theoretically shown that superexchange provides the required anisotropy to lift the Mermin-Wagner theorem in  $\text{CrI}_3$ , the race was on, and the first group to succeed in exfoliating a monolayer of  $\text{CrI}_3$  and demonstrating the first ever two-dimensional material with intrinsic magnetism was the one of X. Xu in 2017 [142]. The key magneto-optical Kerr effect (MOKE) measurements taken at 15 K from Huang *et al.* [142] are depicted in Fig. 4.3. They employed a MOKE design that was sensitive to out-of-plane magnetization. Reflection of a linearly polarized laser off a magnetic sample would rotate the polarization axis by an angle defined as the Kerr angle  $\theta_K$ . Figure 4.3a shows the Kerr angle as a function of applied perpendicular magnetic field of a monolayer  $\text{CrI}_3$ . The recorded hysteresis curve together with a remanent Kerr angle at zero magnetic field is a clear indication for ferromagnetic ordering with a coercive field  $H_c$  of approximately 50 mT. The authors of [142] measured the critical temperature of their monolayer sample to be 45 K. They observe a similar data set for three layers of  $\text{CrI}_3$  as depicted in Fig. 4.3c. The critical temperature of three layers was measured to be identical to bulk  $\text{CrI}_3$ , i.e. 61 K. Interestingly, when they measured a bilayer, the picture completely changed (Fig. 4.3b). Below a magnetic field of 0.65 T, the Kerr angle was zero with a sharp increase for  $B > 0.65$  T. From these data they concluded that A-FM coupled bilayer  $\text{CrI}_3$  is the magnetic ground state. The A-FM interlayer coupling results in what is commonly called the *odd-even effect*: While an even number of layers exhibit close to zero magnetization, an odd number of layers exhibit the magnetization of one fully polarized  $\text{CrI}_3$  flake i.e.  $14.7 \mu_B/\text{nm}^2$ .

This conclusion remained controversial because it is in conflict with the established fact that bulk  $\text{CrI}_3$  is a ferromagnet [160, 166]. In addition, MOKE measurements are not quantitative and can lead to wrong interpretation for the magnetization, e.g. nonzero signals are observed even for antiferromagnets [167]. Further, assuming the proposed antiferromagnetic interlayer coupling, the trilayer flake should have the same magnetization at low fields as the monolayer. Unfortunately, this information is not apparent from the measured Kerr rotation i.e. the Kerr rotation for the monolayer ( $\theta_K \approx 4$  mrad) does not yield the same value as for three layers ( $\theta_K \approx 70$  mrad). Still, A-FM interlayer coupling for  $\text{CrI}_3$  flakes with more than two layers has been claimed by the authors and was further supported by follow up experiments [142, 146, 153, 155] – however, an explanation for this surprising finding remained elusive.

An explanation of the odd-even effect can be found in the stacking order of  $\text{CrI}_3$ .  $\text{CrI}_3$  assumes the monoclinic structure above 210 K and the rhombohedral below. The

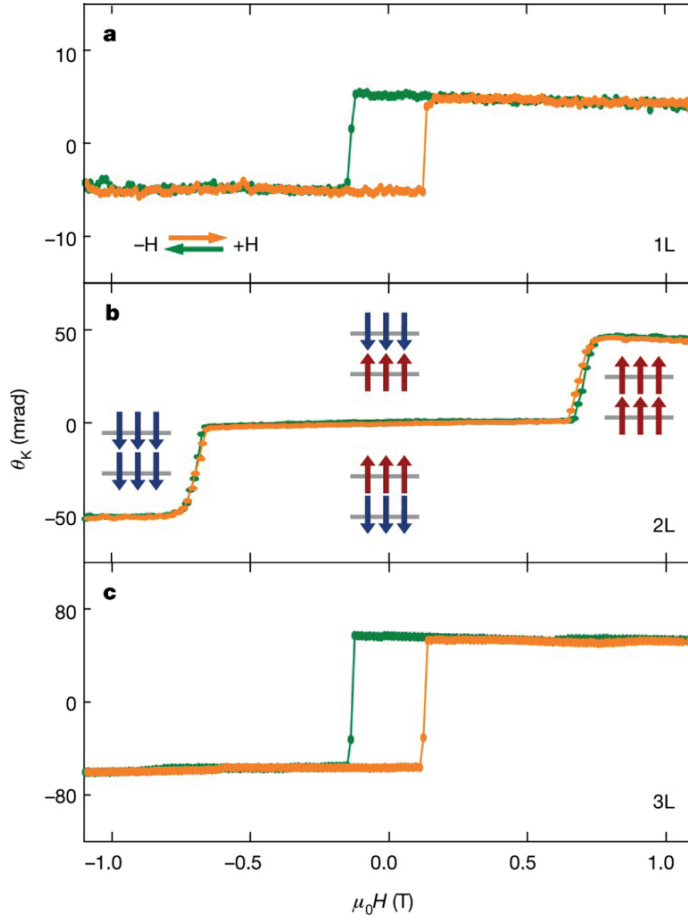


**Figure 4.3.: Layer-dependent ferromagnetism in  $\text{CrI}_3$  at 15 K.** **a** MOKE signal of a single layer (1L)  $\text{CrI}_3$  as a function of perpendicular field. The remanent Kerr signal at zero field and hysteresis are hallmarks of intrinsic magnetism. The magnetization is flipped at an approximate coercive field of 50 mT. **b** MOKE signal of a bilayer (2L)  $\text{CrI}_3$ . Vanishing Kerr angle at zero field suggests A-FM ordering and the magnetization is fully saturated above a field of 0.65 T. **c** MOKE signal of three layers (3L)  $\text{CrI}_3$  again revealing ferromagnetic behavior. However, it is not obvious from the MOKE signal strength if the magnetic signal originates from a magnetization equivalent to one or three ferromagnetically coupled layers of  $\text{CrI}_3$ . The figure is adapted with permission from [142], Springer Nature.

significant change is the different arrangement of the iodine atoms at the interface between two layers, which are mainly responsible for the interlayer coupling. In the LT phase, electron sharing is between two iodine atoms from different layers, leading to an FM interaction. Based on density functional theory (DFT) calculations [162] the FM arrangement of spins for a bilayer is about 3.15 meV/Cr lower in energy than the A-FM state (Fig. 4.1c). This means that the magnetic ground state will show FM

interlayer coupling and cannot be easily changed by strain, electric fields or doping. On the other hand, in the HT phase electron sharing is between a tri-iodine cluster, leading to an A-FM interaction. In the case of a bilayer in the HT phase, the A-FM state is only 0.12 meV/Cr lower than the FM state. The calculations also showed that with increasing number of layers, the A-FM state becomes less favorable even in the HT phase, and the FM state eventually becomes the magnetic ground state, explaining the ferromagnetism in bulk  $\text{CrI}_3$ .

To summarize,  $\text{CrI}_3$  shows two independent phase transitions. One is associated with a structural phase transition around 210 K [160] with a HT and LT stacking order. The other is a magnetic phase transition that occurs at a Curie temperature between 45 K and 61 K [142]. Below the Curie temperature, intralayer magnetic order in a monolayer  $\text{CrI}_3$  is predominately stabilized by an isotropic, symmetric superexchange interaction [157, 165]. In few-layer  $\text{CrI}_3$  interlayer magnetic coupling is predicted to be A-FM (FM) in the HT (LT) phase. As  $\text{CrI}_3$  flakes are cooled down to 4 K, a structural transition from the HT to LT phase is expected along with a magnetic transition from A-FM to FM interlayer coupling. However, as depicted in Fig. 4.1c a 10 meV/Cr transition barrier might keep the  $\text{CrI}_3$  in its HT phase even at low temperatures, resulting in the A-FM interlayer coupling even below the Curie temperature. While the structural phase at low temperature in few-layer  $\text{CrI}_3$  is unknown, the antiferromagnetic order is experimentally observed [142, 146, 153, 155] and theoretically backed up [149, 162, 167–169]. So far non-permanent switching from A-FM to FM interlayer coupling has been shown using electrostatic doping [152], magnetic [142, 146, 155] and electric fields [153]. Still, these switching events are not due to a structural change (from HT to LT phase) and are reversible.

Before we present our data, which quantitatively prove the odd-even effect and give first evidence of permanent switching of the interlayer coupling from A-FM to FM due to a crystallographic transition, we introduce the measured  $\text{CrI}_3$  samples and their fabrication process.



### 4.3. Sample preparation

The crystals we studied were grown, exfoliated, characterized and encapsulated by the Morpurgo group<sup>3</sup> at the University of Geneva, which studies microscopic electronic process in various classes of 2D materials, among them  $\text{CrI}_3$ .

Our collaborators grew  $\text{CrI}_3$  crystals using the chemical vapor transport method [160]. They mixed pure chromium and iodine in a nominal ratio of 1:3 with a total mass of 0.3 g and inserted this material into an evacuated quartz tube that had previously been flushed with argon. They placed the tube inside a furnace, heated it to  $\sim 700^\circ\text{C}$ , and kept it in the furnace for seven days. This process produced shiny, plate-like, dark grayish crystals which they analyzed with X-ray diffraction to confirm the monoclinic crystal structure, as well as with electron dispersive X-ray spectroscopy to confirm the 1:3 atomic ratio.

They micromechanically cleaved the crystals and transferred them onto 90 nm  $\text{SiO}_2/\text{Si}$  wafers inside a  $\text{N}_2$  filled glovebox because exfoliated thin ( $< 20$  nm) single  $\text{CrI}_3$  crystals fully degrade upon exposure to air within minutes. In a following step they encapsulated the crystals in an air-stable material such as thin graphite (3 – 10 nm) or h-BN (5 – 20 nm) via a pick and release technique using a polymer stack [170]. They determined the thickness of the flakes before encapsulation based on the relative optical contrast (RGB values of the optical image) between the  $\text{CrI}_3$  flakes and the 90 nm  $\text{SiO}_2$  layer [142], which was calibrated via the analysis of 80 atomically thin crystals, as shown in Fig. 4.4. In addition the collaborators confirmed the extracted thickness using an atomic force microscope after encapsulation.

Our collaborators produced samples of various  $\text{CrI}_3$  thicknesses in the range of a few ( $< 10$ ) layers to study the effect of thickness on magnetic ordering. Table 4.1 gives an overview of the devices. Four flakes had odd, but different number of layers, i.e.

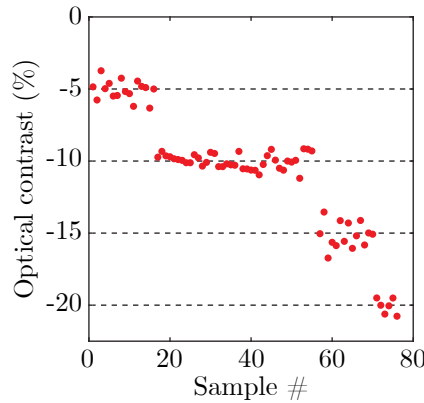


**Figure 4.4.: Relative optical contrast of atomically thin  $\text{CrI}_3$  crystals.** The contrast is calculated as  $C = \frac{I_{\text{flake}} - I_{\text{substrate}}}{I_{\text{flake}} + I_{\text{substrate}}}$  where  $I_{\text{flake}}$  ( $I_{\text{substrate}}$ ) is the reflected red-channel intensity from the flake (substrate). Contrast of around 5%, 10%, 15% and 20% correspond to mono-, bi-, tri- and tetra-layers  $\text{CrI}_3$ , respectively.

<sup>3</sup>Quantum electronics group, University of Geneva (Switzerland)

1-, 3-, 5- and 9-layer, and two flakes were bilayers. Detailed overview of the sample geometries and the relevant characterization data for each device can be found in Appendix A.3.1.

Our collaborators also performed Raman scattering experiments on the  $\text{CrI}_3$  flakes to determine the crystalline structure. Using a Horiba scientific confocal microscope in backscattering geometry, they illuminated the flakes with 532nm laser light and sent the Raman signal to a Czerni-Turner spectrometer equipped with an 1800 grooves/nm grating, which gives a spectral resolution of  $0.3 \text{ cm}^{-1}$ . They detected the light with a thermopower cooled CCD-array. They performed the Raman measurements in a cryostat allowing for the determination of the crystalline structure at room and low temperature ( $< 10 \text{ K}$ ). For further analysis the Raman spectra were fit using Lorentzian lineshapes. The results of these measurements are discussed later in the text.

Device	# layers	Encapsulation material
D1	2	h-BN
	3	
D2	5	thin graphite
	9	
D3	1	h-BN
	2	

**Table 4.1.:  $\text{CrI}_3$  devices measured with our NV magnetometer.** In total, we measured three samples and looked at devices with 1-, 2-, 3-, 5- and 9-layer of  $\text{CrI}_3$ . We also indicate the material the flakes were encapsulated in to avoid degradation.

## 4.4. Quantitative magnetization measurements of $\text{CrI}_3$

In Sec. 4.2 we have seen that MOKE measurements on thin layers of  $\text{CrI}_3$  suggest an odd-even effect for the magnetization. These measurements are not quantitative and cannot exclude a finite magnetization for vanishing Kerr rotation. Hence, these measurements do not prove that a trilayer (or any sample with an odd number of layers) has the magnetization of just one single monolayer with  $\sigma_z^{\text{mono}} = 14.7 \mu_B/\text{nm}^2$  [160], and neither do they prove that samples with even numbers of layers have no magnetization.

In this section, we use NV magnetometry to overcome these limitations and show quantitative magnetization maps with spatial resolutions of few tens of nanometers, which will confirm the odd-even effect. We conducted all experiments with the same NV center, and the NV sample distance for all scans was  $z_{\text{NV}} \approx 60 \text{ nm}$ . We cooled the samples below their Curie temperatures in zero-field to a base temperature of about 7 K. We then performed both iso-field (see Sec. 2.1.5) and full field (see Sec. 2.1.4) scans on all devices listed in Tab. 4.1. Figure 4.5 shows the measurement schematic along with the NV orientation valid for all measurements shown in this section and gives the basic configuration for the subsequent measurements.

Assuming antiferromagnetic interlayer coupling, we expect no net magnetization from an even number of layers and, hence, no stray fields. An odd number of layers yield a uniform magnetization of strength  $\sigma_z^{\text{mono}}$ . As already discussed in Sec. 2.2.3, a homogeneous magnetization produces also no magnetic stray field except on the edges. In an intuitive picture we treat the homogeneously magnetized domain as a current loop with the current flowing along the edge. For a large domain, the size of

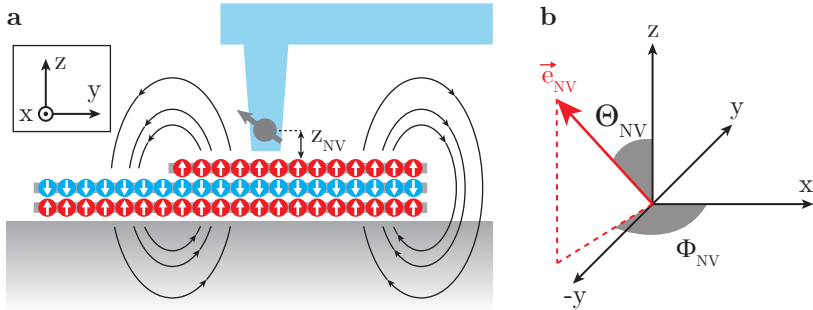


**Figure 4.5.: Setup schematic and NV orientation.** **a** We scan a single Nitrogen-Vacancy electronic spin (gray arrow in blue diamond cantilever) across few layer flakes of encapsulated  $\text{CrI}_3$  (encapsulation not shown). The NV senses stray magnetic fields from the sample by optically detected Zeeman shifts of its spin states and images them with nanoscale resolution (set by the sensor-sample separation  $z_{\text{NV}}$ ) by lateral scanning. Stray fields originate only at the edges of odd numbered layers in the case of antiferromagnetic interlayer coupling. **b** The magnetometer detects magnetic fields along the NV spin quantization axis  $\vec{e}_{\text{NV}}$ , at an angle  $\theta_{\text{NV}} \sim 54^\circ$  from the sample normal and  $\phi_{\text{NV}} \sim 95^\circ$  from the x-axis. In all 2D measurement data sets, the z-axis is the sample normal (see Appendix Fig. A.13b).

the current loop increases and the generated stray field goes towards zero<sup>4</sup>. Only at the edge of the domain itself, the magnetization is non-uniform (see Eq. (2.36) and (2.37)) and, hence, produces magnetic stray fields [171]. The situation is illustrated in Fig. 4.5a.

We first investigated device D1 with our cryogenic magnetometer. It comprised a bilayer and trilayer flake of CrI<sub>3</sub> as indicated in Fig. 4.6a. A typical magnetic field map of device D1 is shown in Fig. 4.6b. We acquired the presented data in a bias field of  $B_{\text{NV}}^{\text{bias}} = 172.5$  mT. The scan took approximatively 39 h of data taking with an acquisition time of  $\approx 2$  s/pixel. As anticipated, we see (almost) no stray fields from the bilayer flake and strong stray fields at the edges of the trilayer flake.

Although the magnetic field map looked very promising, we were mostly interested in the underlying magnetization pattern  $\sigma(x, y, z = 0)$ . In order to quantify the magnetization of the sample, we employed two different methods. First we performed a reverse propagation (as discussed in Sec. 2.2.3) on the magnetic field data set, which is depicted in Fig. 4.6c. The magnetization pattern clearly showed a largely homogeneous magnetization for the trilayer CrI<sub>3</sub> flake, which is typical for most samples we investigated. In addition, sparsely scattered, localized defects, mostly with vanishing magnetization, were visible across the flake. A few irregularities, likely caused by curling and rippling induced during sample preparation, also occurred at the flake edges. On the flake, we found an average magnetization  $\sigma_z \approx 13.0 \pm 2.4 \mu_B/\text{nm}^2$  (Fig. 4.6d), where the error corresponds to the full width at half maximum of a Gaussian fitted to the magnetization histogram. This value is consistent with a single layer of fully polarized Cr<sup>3+</sup> spins. The data thus support the notion of antiferromagnetic interlayer exchange coupling in few-layer CrI<sub>3</sub>, which results in a net magnetization  $\sigma_z^{\text{mono}}$  for the magnetically ordered trilayer sample.

We additionally determined  $\sigma_z$  in an independent way by measuring the magnetic stray field  $B_{\text{NV}}$  along lines crossing the edges of each flake (see white dashed arrow in Fig. 4.6a). Assuming a purely out-of-plane magnetization, the stray field at the sample edge resembles that of half a Bloch wall (see Appendix A.3.3) and analytical fits (see Appendix A.3.2) to these data allow for the quantitative determination of both  $\sigma_z$  and  $z_{\text{NV}}$  (Fig. 4.6e). For the trilayer we then found  $\sigma_z = 15.2 \pm 0.3 \mu_B/\text{nm}^2$ , where the uncertainty denotes the  $2\sigma$  confidence interval of a least squares fitting routine. The general agreement of the fit with the value of  $\sigma_z$  found in Fig. 4.6d further confirmed the validity of the reverse propagation method we employed.

Sample D1 additionally contained a region of bilayer CrI<sub>3</sub>, on which we observed zero bulk moments, again consistent with antiferromagnetic interlayer coupling. However, the bilayer also showed a weak magnetization located at the edge to within our spatial resolution. This was not expected and we can give a lower bound of the magnetization by fitting the magnetic field  $B_{\text{NV}}$  across the bilayer flake edge to an out-of-plane 1D spin chain, which yields  $\approx 177 \mu_B/\text{nm}$  (see Appendix A.3.4). For a one dimensional out-of-plane magnetized CrI<sub>3</sub> spin chain we would expect a magnetization of  $\sqrt{14.7} \mu_B/\text{nm} = 3.83 \mu_B/\text{nm}$  clearly below the fitted value. An upper bound of the magnetization is given by a uniform out-of-plane 2D spin plane and the fit gives  $\approx 1.45 \mu_B/\text{nm}^2$ , which is below  $\sigma_z^{\text{mono}}$ . Since the fitted magnetization is too high for

---

<sup>4</sup>  $\lim_{r \rightarrow \infty} B(r) = \lim_{r \rightarrow \infty} \frac{\mu_0 I}{2r} = 0$ , where  $I$  is the current,  $r$  is the radius of the current loop and  $B(r)$  the field in the center of the loop.

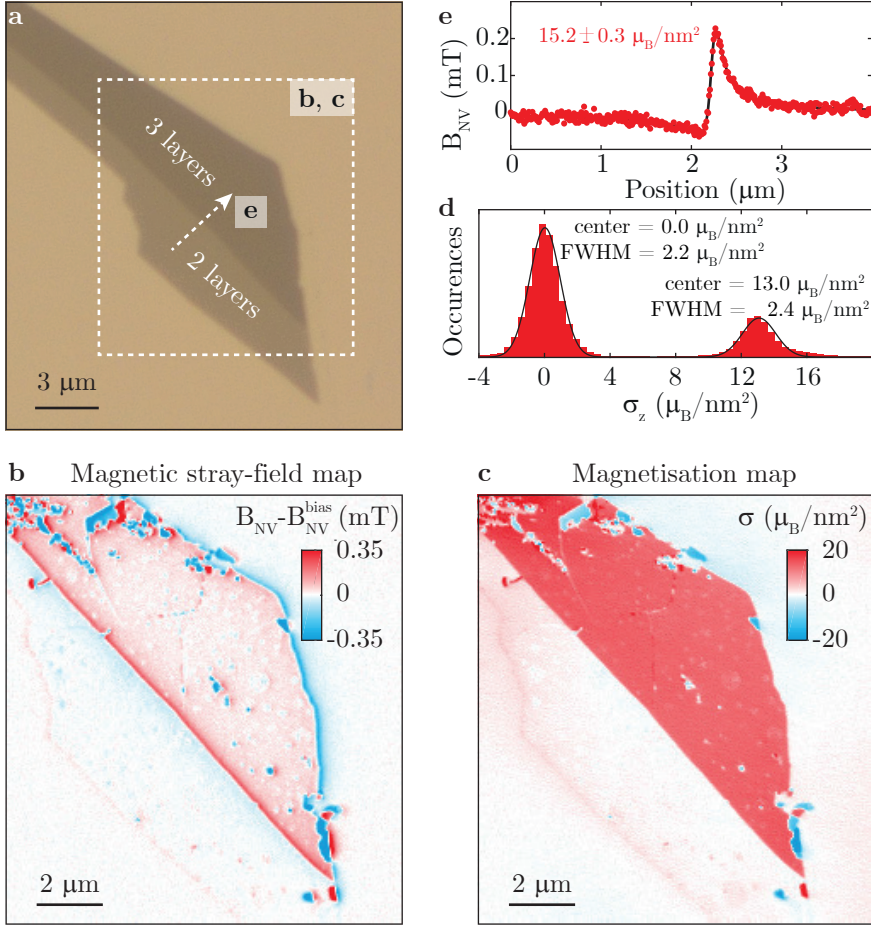


**Figure 4.6.: Nanoscale imaging of magnetism in two-dimensional van der Waals magnets.** **a** Optical micrograph of the  $\text{CrI}_3$  bi- and trilayer flake of sample D1. The scan area of **b** and **c** is illustrated with the white dashed box. The white arrow indicates the line scan in **e**. **b** Magnetic field map of  $B_{\text{NV}}$  across sample D1 recorded in a bias field  $B_{\text{NV}}^{\text{bias}} = 172.5$  mT and at a typical green laser power  $P_{\text{laser}} \approx 40 \mu\text{W}$ . Strong (close to zero) stray fields emerge from the edges of the trilayer (bilayer) flake, respectively. **c** Map of  $\text{CrI}_3$ 's magnetization distribution in sample D1, determined by unique reverse-propagation (see Sec.2.2.3) of the magnetic field map in **b**. **d** Histogram of the magnetization found in **c**. The histogram is fitted to the sum of two Gaussians and suggests a uniform trilayer magnetization of  $13.0 \pm 2.4 \mu_B/\text{nm}^2$ . **e** Independently acquired data of magnetic field  $B_{\text{NV}}$  (red) measured across the border of the trilayer flake along the line indicated **a**. This data allows for an independent determination of magnetization  $\sigma_z$  and sensor-sample separation  $z_{\text{NV}}$  using analytic fits (black) (see A.3.2).

a 1D spin chain and too low for a monolayer of spin-polarized  $\text{CrI}_3$ , a narrow magnetized stripe is very likely to explain the observed magnetization strength. The origin of this magnetization is currently unknown but could be related to magneto-electric effects<sup>5</sup> [149, 152], a narrow region of monolayer  $\text{CrI}_3$  protruding from the bilayer, or to spin canting [172] close to the edge of the flake.

We will now discuss the data we took on sample D2 and D3, which contain a monolayer, a five, and nine layer thick flake. We will only consider the magnetization maps obtained from reverse propagation, while the raw magnetic field images can be found in Appendix A.3.5. The magnetization maps are shown in the top panel of Fig. 4.7a, b and c, respectively. Strikingly, we observed that the number of defects decreases with increasing number of layers from one to two, three, five and nine layers. We attributed this effect to the increased difficulty to homogeneously exfoliate very thin  $\text{CrI}_3$  flakes. As expected for the magnetization, all these flakes exhibited near-uniform magnetization at a magnitude comparable to one layer of  $\text{CrI}_3$ , i.e.  $\sigma_z^{\text{mono}}$ . We also performed line scans over the sample edge on each sample (see black dashed line in Fig. 4.7a, b and c top panel), which are depicted in the bottom panel of Fig. 4.7a, b and c.

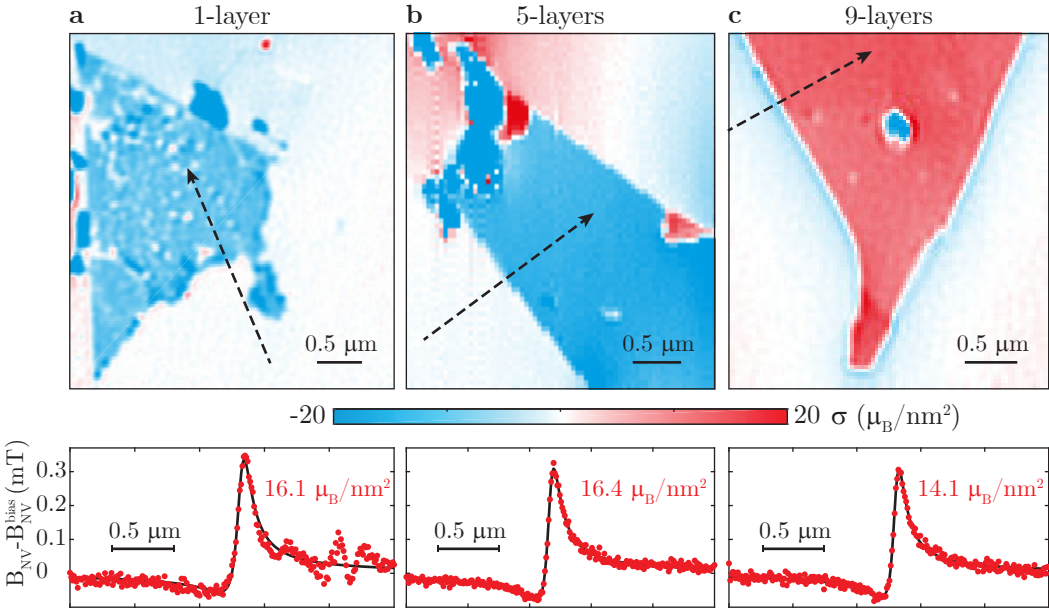


**Figure 4.7.: Magnetization maps of few-layer  $\text{CrI}_3$  flakes.** Magnetization maps were obtained for a monolayer (a), a five (b) and a nine (c) layer thick sample. The colorbar applies to all panels. Lower row: Independently acquired data of magnetic field  $B_{\text{NV}}$  measured across the borders of each flake, along the lines indicated in the maps. These data allow for an independent determination of magnetization  $\sigma_z$  and sensor-sample separation  $z_{\text{NV}}$  using analytic fits (black) [171].

<sup>5</sup>Electrostatic doping modifies the saturation magnetization, coercive field and Curie temperature and can induce a transition from an antiferromagnetic to a ferromagnetic interlayer exchange coupling.

The corresponding analytical fits yield  $\sigma_z = 16.1 \pm 0.6 \mu_B/\text{nm}^2$ ,  $16.4 \pm 0.2 \mu_B/\text{nm}^2$  and  $14.1 \pm 0.2 \mu_B/\text{nm}^2$  for the monolayer, 5-, and 9-layer flakes, respectively, again in good agreement with  $\sigma_z^{\text{mono}}$ . Our observations thus far corroborated previous results on few-layer CrI<sub>3</sub> [146, 153, 155], which all found CrI<sub>3</sub> flakes with odd numbers of layers to exhibit nonzero magnetization and even numbers of layers to exhibit close to zero magnetization as a result of antiferromagnetic interlayer exchange coupling.

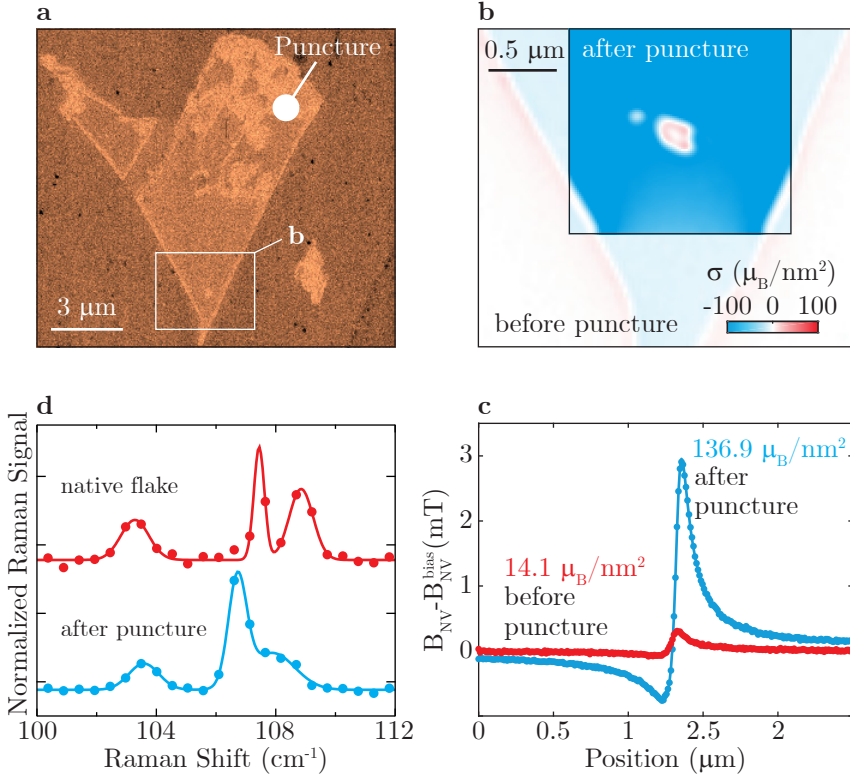


**Figure 4.8.: Interplay of structural and magnetic order in few-layer CrI<sub>3</sub>.** **a** Overview image of sample D2 (see Fig. A.8d), indicating the location of the puncture (see Fig. A.8d), and the representative region sampled in the following. **b** Enhanced magnetization observed in the 9-layer flake of sample D2, after puncturing the CrI<sub>3</sub> encapsulation. Note that the location of the puncture is a few  $\mu\text{m}$  away from the imaged region (see **a**). The faint background shows the (inverted) data from Fig. 4.7c for comparison. The same colorbar applies to all data. **c** Line-cut of  $B_{\text{NV}}$  across a representative edge of the punctured flake (blue), indicating a magnetization  $\sigma_z = 136.9 \pm 0.4 \mu_B/\text{nm}^2$ , close to the expected value for a fully polarised nine-layer sample. For reference, the red data shows the corresponding data from before the puncture (see Fig. 4.7c, lower panel). **d** Raman spectra from the punctured flake and an unpunctured reference taken at 6 K, demonstrating the concurrence of a structural transition together with the magnetic transition.

These observations, however, are in conflict with the established fact that  $\text{CrI}_3$  is a bulk ferromagnet [166] and are therefore addressed by us next.

We shed light on this dichotomy in a subsequent experiment on sample D2, where our diamond scanning probe induced an unintentional local puncture through the encapsulation layer of the  $\text{CrI}_3$  flake (Fig. A.8d and Fig. 4.8a). After this, the whole sample, up to several microns away from the puncture, exhibited a significantly enhanced magnetization, as evidenced by a representative magnetization map (Fig. 4.8b) and  $B_{\text{NV}}$  linescan (Fig. 4.8c) across the flake. The data show a  $\approx 9.7$ -fold increase of magnetization from initially  $14.1 \pm 0.2 \mu_B/\text{nm}^2$  to  $136.9 \pm 0.4 \mu_B/\text{nm}^2$ . For the 9-layer flake under study, this enhancement suggests a transition from antiferromagnetic to ferromagnetic interlayer coupling induced by the puncture.

An explanation for this phenomenon is the dependency of the magnetic coupling to crystallographic structure. As described in Sec. 4.2, we expected such a magnetic transition when the stacking order of  $\text{CrI}_3$  changes from the HT to the LT phase. To investigate if the magnetic transition was accompanied by a structural transition in our punctured sample, we have compared in Fig. 4.8d its low-temperature Raman spectrum with the one of a pristine flake, in a spectral region, where characteristic Raman modes for  $\text{CrI}_3$  exist [173]. The complete set of Raman data can be found in Appendix A.3.6. Although the data did not allow for an unambiguous determination of the crystalline structure of our samples, the markedly different spectra clearly point to a change in structure. We speculate that strain, for instance due to the encapsulation, initially suppresses the structural phase transition at 210 K leading to A-FM interlayer coupling, and that only our induced puncture allowed strain to relax and the sample to assume its structural and magnetic ground state. Even after a temperature cycling process to room temperature and back to cryogenic temperatures, the sample still featured ferromagnetic coupling. Therefore, we reported for the first time on the observation of ferromagnetic intralayer coupling in  $\text{CrI}_3$  induced by a permanent change of crystal structure.

Interestingly, sample D2 not only showed homogeneous magnetization (Fig. 4.7b, c, compare also Fig. A.8c) but also the occurrence of magnetic domains. Domains in  $\text{CrI}_3$  have been reported [142, 154] but never quantitatively measured. Figure 4.9a shows a representative image of such domains on the 9-layer flake (see also Fig. A.8c). The average domain size is around 1  $\mu\text{m}$  and the measured domain magnetizations assume values close to integer multiples of  $\sigma_z^{\text{mono}}$ , i.e.  $\sigma_z = n\sigma_z^{\text{mono}}$ , with  $n \in \mathbb{Z}$ . This is striking as we expected domains with only  $n = 1$  in case of antiferromagnetic or  $n = 9$  in the case of ferromagnetic interlayer coupling, but no  $n$ -values in between. Our observation can be explained by spatial variations (in all three dimensions) of exchange couplings, which may alter the ordering of pairs of  $\text{CrI}_3$  layers from antiferromagnetic to ferromagnetic between adjacent domains, e.g. due to a local change in crystal structure or stacking order. For instance, seven A-FM coupled layers on top of two ferromagnetic coupled layers yield an effective magnetization of  $\sigma_z = 3\sigma_z^{\text{mono}}$ . While this domain formation mechanism would preserve the parity of  $n$ , i.e. for a nine layer flake it is only possible to detect an odd multiple of the monolayer magnetization, we observe well-separated regions on the sample where  $n$  is either even or odd (see outlines in Fig. 4.9a and histogram in Fig. 4.9b). We explain this observation with the removal or addition of a monolayer of  $\text{CrI}_3$  between these areas, which could have occurred during material exfoliation or sample preparation.



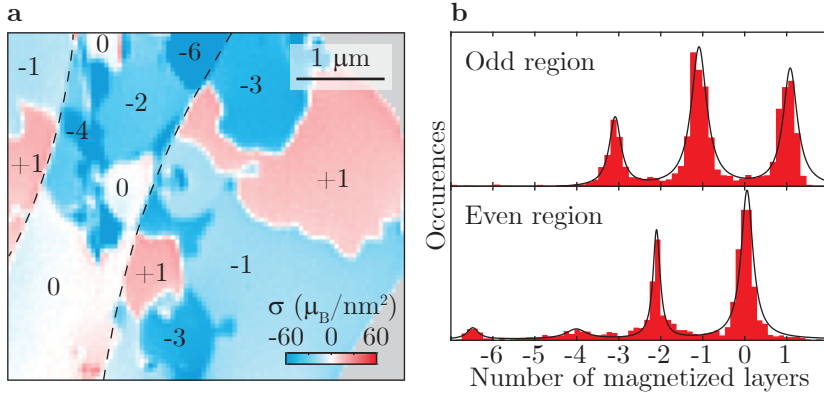


**Figure 4.9.: Magnetic domains in  $\text{CrI}_3$ .** **a** Spontaneously occurring magnetic domains observed in the nine-layer sample D2. The magnetization  $\sigma_z$  was found to be discretized in integer multiples of the monolayer magnetization  $\sigma_z^{\text{mono}}$ . Numbers indicate  $\sigma_z$  in multiples of  $\sigma_z^{\text{mono}}$ , where positive (negative) values denote magnetizations along the  $+z$  ( $-z$ ) direction. A clear separation of the flake into regions of even- and odd-multiples of  $\sigma_z^{\text{mono}}$  is observed. Even-numbered regions are assigned to a missing or added monolayer (see text). Areas where no flake was present were false-color coded in gray. The scan section is indicated in Fig. A.8c. **b** Histograms of magnetization pixel-values obtained in the odd- and even-numbered regions of the data in **a**.

With a last measurement, we confirmed experimentally that for typical experimental parameters we employed, our approach induced little back-action onto the sample, e.g., through heating by laser illumination. To that end, we performed linescans over flake edges on sample D2 at various laser powers from  $30 \mu\text{W}$  to  $350 \mu\text{W}$  (see Fig. 4.10). Laser powers above  $100 \mu\text{W}$  slightly lower the value of measured magnetization compared to the results obtained at lower powers. Working with  $P_{\text{laser}} = 40 \mu\text{W}$  in all data sets ensured that no significant back-action from heating by laser power was induced onto the samples.

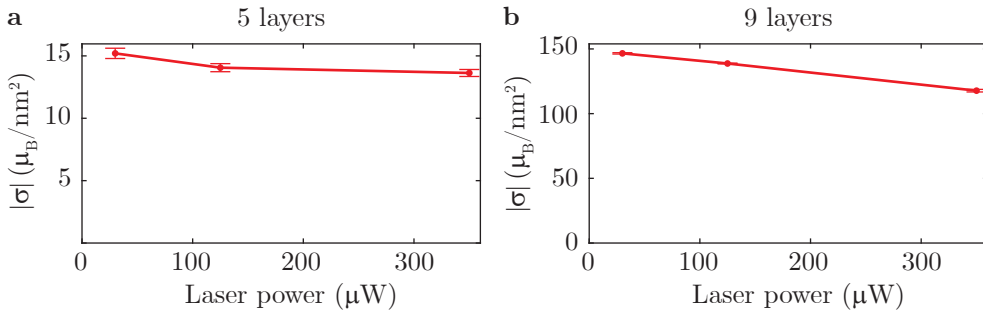


**Figure 4.10.: Impact of laser irradiation.** Influence of 532 nm laser power on the magnetization extracted from linecuts of  $B_{NV}$  across the edges of a flake. The panel in **a** (**b**) shows magnetization of linecuts as indicated in Fig. 4.7**b** (Fig. 4.7**c**). The linecuts over the 9-layers flake edge were performed after the puncture.

## 4.5. Summary

We applied our scanning NV sensor to obtain the first quantitative magnetization data on the prototypical two-dimensional ferromagnet  $\text{CrI}_3$ . We measured the stray magnetic fields of flakes with various thickness, i.e. one, two, three, five and nine layers. Using reverse propagation we deduced the underlying magnetization pattern. The flakes showed mostly a uniform magnetization with localized defects. Strikingly, the number of defects is clearly higher in the mono- and trilayer samples compared to the nine layer sample, reflecting the increasing difficulty in exfoliating very thin samples.

In order to extract a quantitative number for the magnetization from the measured stray fields, we used two independent approaches, namely reverse propagation and analytical fitting of stray fields data across a sample edge. Both approaches are in good agreement and confirm the even-odd effect. For the samples with an even number of layers, we did not see any magnetization, while all samples with an odd number of layers showed magnetization at a magnitude comparable to a fully polarized monolayer of  $\text{CrI}_3$ . A possible explanation for this phenomena is that  $\text{CrI}_3$  is stuck in its high-temperature phase, in which interlayer interactions lead to antiferromagnetic coupling of layers.

Upon puncturing the sample with nine layers the sample showed a ninefold increase in magnetization not only locally around the puncture but across the whole flake. The hole possibly removed strain or introduced some energy so that the sample relaxed into its energetically more favorable low-temperature phase. This phase is predicted to feature ferromagnetic interlayer coupling, which explains the observed change in magnetization. A clear connection of this phenomena to a structural change is established with Raman measurements.

We have also seen native domains in parts of an otherwise homogeneously magnetized flake. Surprisingly, the domains exhibited magnetization greater than one fully polarized monolayer. We assign the origin of the domains to the same effect meaning spatial variations of exchange coupling leading to ferro- and antiferromagnetic coupling of layers within one stack of layers. However, this is a tentative explanation only and requires further investigation.

## 4.6. Outlook

The quantitative nature of NV magnetometry allowed us to put precise numbers on the magnetization and revealed details of the interlayer couplings of  $\text{CrI}_3$ . The high spatial resolution of our technique paved the way to look more closely at domains within that material which would not have been resolvable with other methods. These results therefore advances our understanding of two-dimensional magnets.

Within this thesis, we made preliminary steps towards two follow-up experiments. First, we can study the transition of a material from the thin-film limit to bulk. It is known that bulk  $\text{CrI}_3$  is ferromagnetic[160] and exhibits a monoclinic (LT) structure. In our experiments, we observed antiferromagnetic interlayer coupling and rhombohedral (HT) structure for samples as thick as 9-layer. In addition, theory predicts even for the HT state a ferromagnetic coupling for an infinite number of layers[162]. In an experiment, we can increase the number of layers one by one

and will observe at some point a transition from anti- to ferromagnetic interlayer coupling. The questions that arise are: Is this transition sharp in the number of layers and is it reproducible? Do we observe ferromagnetic coupling paired with the HT phase according to theory or is the ferromagnetic coupling associated with a structural transition to the LT phase as for bulk? How does this magnetic transition depend on temperature, charge carrier density [152], electric fields [153], and crystal structure [162]?

Second, so far there is no reproducible way of transitioning thin-film  $\text{CrI}_3$  from the HT to the LT phase and back. If strain prevents  $\text{CrI}_3$  from relaxing into the energetically more favorable structural phase, annealing the sample could be a possible way to reduce strain. However, as we do not know the right parameters for the temperature and annealing gas, a large parameter space is to be explored, which is under current investigation. Both of these experiments require no more sophisticated NV measurements than shown so far and can be readily conducted, but are very challenging and time-consuming from a nanofabrication aspect.

On the long time scale there are more ambitious experiments to be tackled that appear worthwhile to pursue and are described in the following. At the origin of these experiments are magnetic domains in  $\text{CrI}_3$ . Domains are of high relevance to magnetic switching events and electronic transport measurements but also to the technical area of spintronics as a key ingredient of the racetrack memory [174]. Before we proceed, we would like to distinguish between two sorts of domains – crystalline structure related and induced domains. The data set in Fig. 4.9 shows domains resulting from spatial variations in stacking order that are strongly pinned and cannot be moved by external magnetic fields. In contrast to them are the formation of domains induced by magnetic fields, which have been already reported in literature [142, 154]. The origin of these domains are magnetization reversals nucleated at position of small coercive fields. These domains allow us to study mobility and to learn about symmetric and antisymmetric exchange energy by examining the nature of the domain walls. Further we will see that spin-waves in bulk  $\text{CrI}_3$  are not accessible with NV magnetometry in contrast to confined spin-waves, which allow us to study exchange energies and anisotropy [175].

In a first step we identify how such domains can be controllably induced. To that end, we successfully mapped out a few characteristic points on the hysteresis curve of the magnetization in sample D1 as shown in Fig. 4.11. We clearly see reversal of magnetization as the applied field exceeds a critical field along with the formation of two domains separated by a domain wall. A domain wall can be considered as an elastic interface in a potential landscape that can be driven by magnetic pressure. With domain walls at hand, we can study the dynamics and propagation of this interface. On a simplified level, domain wall motion can be classified in a low field regime and high field regime. At zero temperature we expect the domain wall to be pinned for all magnetic fields smaller than the depinning field. However, at finite temperatures – in the low field regime – the domain wall moves due to thermal activation [176]. In this so-called *creep* regime [177] the domain wall is typically rough due to the presence of local disorder. Analyzing this regime will provide us with information on the disorder-induced pinning energy barrier. As we increase the magnetic field above the depinning field, we enter the *flow* regime [178], in which the velocity is proportional to the wall mobility. A characteristic of this regime is a smooth domain wall. In

order to map out the velocity versus magnetic field, one would image the domain wall at zero field, then apply a series of magnetic field pulses of constant magnetic field but increasing pulse duration. After every pulse one would image the magnetic field again and measure the displacement. The gradient of a linear fit to the displacement data plotted against pulse duration then yields the velocity. The only experimental difficulty is to design a pulse coil to reach the flow regime as the depinning fields for  $\text{CrI}_3$  according to our preliminary measurements are above 100 mT.

In a next experiment, one could study the inner structure of a domain wall and thereby make precise statements on the strength of Dzyaloshinskii-Moriya interaction (DMI) [179]. DMI is an antisymmetric superexchange interaction of the form  $(\mathbf{D} \cdot (\hat{\mathbf{S}}_i \times \hat{\mathbf{S}}_j))$ , where  $D$  is the micromagnetic DMI constant. DMI favors non-collinear ground states and leads to canting of spins. By tuning the DMI strength we can therefore modify the spin texture. However, DMI requires sizable spin-orbit interaction [179] and a broken inversion symmetry. In  $\text{CrI}_3$  center of the hexagon formed by the chromium ions act as inversion center (see Fig.4.1a), but signs of finite DMI has been reported between the next-nearest neighbors [175]. Spin-orbit can be introduced by proximity to heavy-metal substrates [36] and gated devices [146, 148–153] can be the solution to the lacking inversion symmetry. The application of an electric field breaks inversion symmetry and may thereby introduce DMI into the system. A Bloch domain wall would then transition into a Néel wall, which produces a slightly different stray magnetic field [17, 36]. We estimate the difference in maximal stray field between a Bloch and a Néel wall for  $\text{CrI}_3$  under typical conditions of our experiment (see Appendix A.3.3) to be  $\approx 0.1$  mT, which would be readily within our detection range. A recent theoretical paper [180] even claimed that beyond a threshold electric field of 0.14 V/nm the monolayer  $\text{CrI}_3$  ground state is not ferromagnetic but supports topologically protected Néel type skyrmions. Since important work [18] on the highly non-trivial relation between the stray field and the nature of a skyrmion and its detection using NV magnetometry has already been done, it should be reasonable to confirm Néel type skyrmions in  $\text{CrI}_3$  using an NV center.

Finally, our technique could potentially contribute to the emerging field of magnonics [181, 182] in 2D van der Waals magnets. There, the central excitations are spin-waves, which are collectively precessing spins in a magnetically ordered system (see 4.2a) and which lead to the decrease of magnetization in a ferromagnet as the temperature approaches the Curie temperature. Furthermore, spin-waves prevent long-range magnetic order in systems without anisotropy (Mermin-Wagner theorem). Yet they are interesting to study in order to understand the underlying physics of a magnetic system as they reveal information on exchange energies and anisotropy [175]. The magnetic anisotropy in  $\text{CrI}_3$  is around 0.1 meV yielding a gap of  $\approx 90$  GHz in the spin-wave spectrum [165]. To sense spin-wave excitations, the sensors transition energy has to lie above the ferromagnetic resonance frequency of the spin waves, which has a  $k$ -vector of zero and produces no magnetic stray field. Therefore, only spin waves with larger  $k$ -vector at higher frequencies can be detected. Unfortunately, in the case of the NV center, the transition energies are in the single digit GHz regime at low bias-fields. As a consequence, the spin-wave frequency needs to be decreased by applying a field opposing the magnetization thereby reducing the effective anisotropy. At the same time the NV resonance increases (Eq.(2.1)) and the two frequencies match at  $B \approx 1.5$  Tesla, which is inaccessible in our current setup. However, we

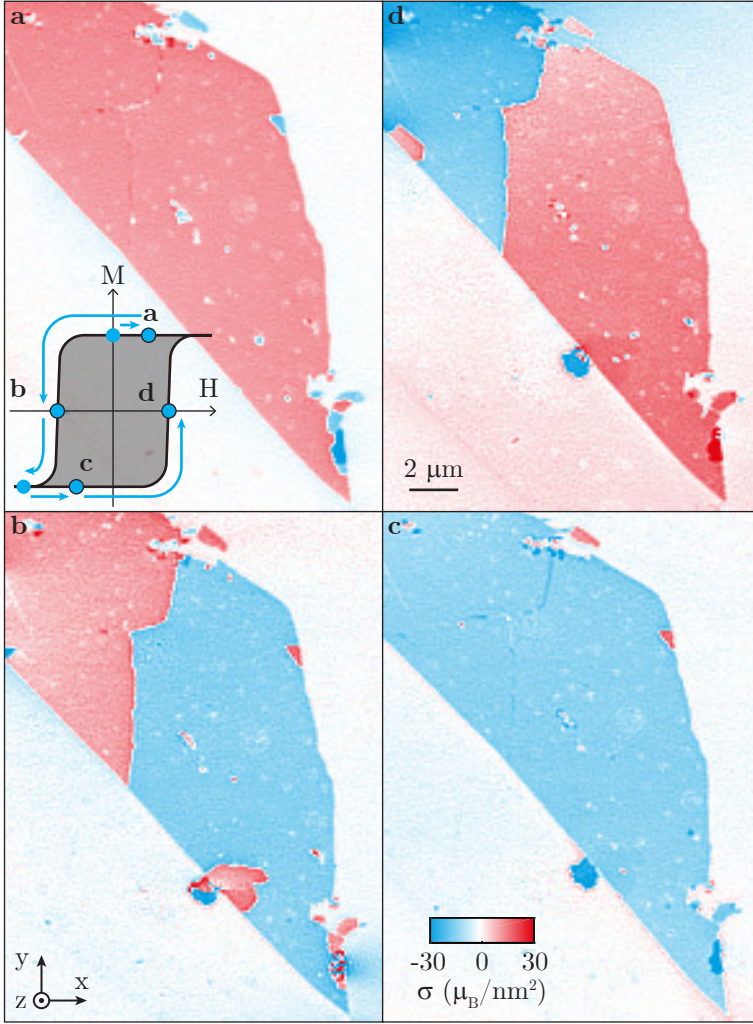


**Figure 4.11.: Hysteresis curve of sample D1.** **a** After a zero field cooling we imaged the magnetization of the trilayer in a field of  $B_z = +90$  mT. The data is the reverse propagation of the field map shown in Appendix A.14. The magnetization is homogeneous over the flake and points out of the imaging plane. The inset shows a schematic for the magnetic field sweeps and the corresponding magnetization of panels **a**, **b**, **c** and **d**. **b** We nucleated a domain by sweeping to a negative field of  $B_z = -120$  mT. **c** We completely inversed the magnetization by sweeping the field to  $B_z = -500$  mT. The colorbar applies to all panels. **d** We swept to a positive field of  $B_z = +120$  mT, which induced a domain again in the lower right of the trilayer. The domain wall was always pinned at the same sites and we did not manage to freeze the domain at some other position. The scale bar applies to all panels.

expect a lower frequency spin-wave for spins that experience little anisotropy. This is the case for horizontally oriented spins within a domain wall, where the magnon gap goes to zero [183]. Such spin-waves are confined to domain walls due to the gapped nature of the bulk and allow us to study the propagation length [184] and the steering around curved domain walls [185, 186]. In order to detect spin-waves we can exploit one of three methods described in [20, 21]. First, thermally excited spin-waves produce magnetic noise that lead to relaxation of the NV spin states that we can measure with  $T_1$ -measurements. Second, we can drive spin-waves that then drive NV spin transitions visible in an electron spin resonance experiment. Third, coherent driving of the spin-waves whose frequency is on resonance with the NV transition frequency leads to an increased Rabi oscillation frequency [187].





## 5. Summary and Outlook

The story of this thesis started with the proposal of a novel, scanning magnetic microscope by means of a photoluminescent nanoprobe. The magnetic stray field was suggested to be measured using optically detected magnetic resonance and a nanoscale lateral resolution was promised. We saw the realization at room temperature using a single spin of the Nitrogen-Vacancy center embedded in an all-diamond scanning probe. At the heart of this work is the expansion of NV magnetometry to cryogenic temperatures that enables the studies of previously inaccessible magnetic phenomena in condensed-matter systems at the nanoscale.

### 5.1. Summary

In Chap. 2 we introduced the NV center, its electronic structure, photo-physics, and magnetic field dependency. We then presented one of the milestones of this thesis – the first implementation of a scanning NV magnetometer at cryogenic temperatures. The setup is based on a functionalized atomic force microscope in a  $^4\text{He}$  bath cryostat combined with a fiber based confocal microscope and equipped with a superconducting vector magnet for high-field application. The setup features single digit  $\mu\text{T}/\sqrt{\text{Hz}}$  field sensitivity, a spatial resolution of 30 nm, and allows for a continuous measurement times of up to six days.

We then described two methods to produce DC magnetic field maps in two dimensions – iso-field and full field imaging. We discussed two different approaches to extract useful information out of these field maps and gain knowledge on the underlying source of the magnetic field. In a first scenario, the source is well known and its stray fields can be theoretically described and readily fitted to the recorded field data. In a second scenario, if detailed field predictions are not available, reverse propagation has been shown to be a powerful technique. We derived how to reconstruct the complete vector magnetic field from the measured field maps, which are generally hard to interpret due to their projection onto the NV axis. We also learned how to extract sample properties like a 2D current or magnetization distribution inside a sample. We provided useful implementation tips as well as MATLAB code of the transformations.

In Chap. 3 we employed our scanning NV setup for the first time by imaging vortices in a type-II superconductor, which allowed us to benchmark our magnetometer against other approaches. After setting the theoretical background, we presented the complete, quantitative information about the stray magnetic field emerging from a vortex. We used this data to discriminate existing models for the stray field and observed that the monopole approximation largely failed to reproduce our data, which highlights the close proximity and, hence, spatial resolution of our sensor. Only a fit of the data to an analytical solution of the London equations gave satisfying agreement and enabled us to independently extract a value for the sensor sample distance and a

characteristic length scale of the superconductor, the London penetration depth. In a second experiment we imaged the field exclusion in a superconducting disk due to the Meissner effect. This represents another direct measurement of the London penetration depth and offered the opportunity to reconstruct the shielding supercurrents in the disk using the reverse propagation method.

In Chap. 4 we dedicated our magnetometer to a magnetic van der Waals material, where theoretical knowledge is only starting to build up.  $\text{CrI}_3$  is the first-ever discovered two-dimensional material that features inherent magnetism. While the intralayer coupling was proven to be ferromagnetic, the interlayer coupling upon stacking of layers is still under debate. First experiments hinted on antiferromagnetic interaction, which is in contrast to theoretical predictions and observations of bulk material. Using the NV center we could not only present the highest resolution magnetization maps available so far, but could also clarify the mystery of the interlayer coupling. We showed that the magnetic interlayer coupling is directly connected to the stacking order of the layers. Additionally, we successfully transferred  $\text{CrI}_3$  to its low temperature structural ground state. This transition was accompanied with a switching from antiferromagnetic to ferromagnetic interlayer coupling in accordance with theory, which has not been experimentally observed so far. We also discovered domains in this material with presumably antiferromagnetic and ferromagnetic coupling.

## 5.2. Outlook

In this thesis we used the NV center to measure position dependent DC magnetic fields and employed reverse propagation to reconstruct a planar current distribution and magnetization patterns uniquely. In this outlook we motivate further routes towards current imaging, i.e. current transport in graphene, and the exploration of static spin textures and dynamic spin-waves in the novel field of van der Waals magnets.

As the reverse propagation of a three-dimensional current distribution from the measurement of the magnetic field is an under-constrained problem, we are restricted to very thin samples with no current variation along the  $z$ -axis or to truly two-dimensional materials. In that regard, graphene forms an ideal electron system exhibiting a variety of physical phenomena [188–190]. Recent advances in fabrication and encapsulation of graphene monolayers improved the electron mobility and led to electron mean free paths of several micrometers [191]. Hence, electrons can travel ballistically over macroscopic distances without scattering and can follow classical trajectories. Direct imaging of these trajectories is known to be a hard problem but can be very informative. One interesting application of our cryogenic magnetometer is transverse magnetic focusing (TMF) of electrons, a phenomenon used to study Andreev reflection [192], spin-orbit interaction [193], and composite fermions [194]. Upon the application of a transverse magnetic field, the Lorentz force will bend the electron trajectory leading to cyclotron orbits. When electrons are injected into graphene from a narrow contact and are focused on a second contact, an integer number of cyclotron diameters away, TMF occurs. The required field for a focusing between two contacts separated by a distance  $L$  is given by [195]

$$B = \frac{2\hbar\sqrt{\pi n}}{eL}p, \quad (5.1)$$

where  $n$  is the carrier density and  $(p - 1)$  the number of reflections between the two contacts. For a realistic density of  $n = 3 \cdot 10^{11} \text{ cm}^{-2}$  and focusing length of  $L = 500 \text{ nm}$ , direct focusing ( $p = 1$ ) occurs at a field of  $B = 250 \text{ mT}$  and one reflection ( $p = 2$ ) at the sample edge at  $B = 500 \text{ mT}$ . These values are well realizable and promise a focus length that should be easily resolvable with the current setup.

The quantization of cyclotron orbits into Landau levels gives also rise to another interesting effect. The quantum Hall effect features insulating bulk together with conducting edge states, which are hard to image. First hints on these edge states are given by scanning tunneling microscopy studies, in which the evolution of Landau levels towards the edge were imaged [197]. Figure 5.1a shows typical transport measurements characterizing the quantum Hall effect at  $B = 14 \text{ T}$ . Changing the charge density  $n$  allowed for sweeping the Fermi energy over the Landau levels (see inset). The Hall conductivity  $\sigma_{xy} = I/V_H$ , defined as the ratio of the longitudinal current and the transverse Hall voltage, increases in steps of  $4e^2/h$ . At every plateau in  $\sigma_{xy}$  the Fermi energy lies in the middle of two Landau levels. The states above the Fermi energy are completely empty, and the ones below completely filled leading to an in-

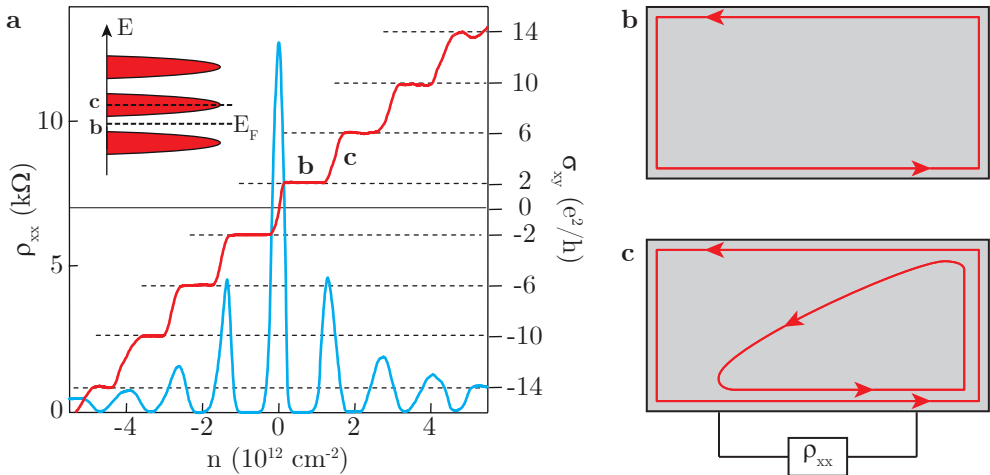


**Figure 5.1.: Quantum Hall effect in graphene monolayer.** **a** Longitudinal resistivity  $\rho_{xx}$  (blue line) and Hall conductivity  $\sigma_{xy}$  (red line) as a function of carrier concentration in a magnetic field of  $B = 14 \text{ T}$ . The label **b** refers to the quantum Hall effect plateaux at  $\sigma_{xy} = 2e^2/h$  and **c** refers to the transition from this plateaux to the next at  $\sigma_{xy} = 6e^2/h$ . The inset displays a simplified sketch of the Landau levels and the position of the Fermi energy in case of **b** (between Landau levels) and **c** (centered on a Landau level). **b, c** Schematic of the edge currents in a graphene device. For  $\sigma_{xy} = 2e^2/h$  (**b**) there are exactly two edge states. The longitudinal resistivity is zero. In **c** the transition to  $\sigma_{xy} = 6e^2/h$  is shown. Free states in the Landau level (see inset in **a**) allow the next edge current to scatter back leading to a finite longitudinal resistivity  $\rho_{xx}$  as indicated in **a**. Figure in **a** is adapted with permission from [196], Springer Nature.

teger number of dissipationless edge channels. When the Fermi energy is positioned in the middle of a Landau level, free states will scatter an edge channel and lead to a non-zero longitudinal resistivity  $\rho_{xx}$  (peaks in  $\rho_{xx}$  in Fig. 5.1a). This means that the application of a magnetic field and correct positioning of the Fermi energy give rise to persistent edge currents. Without an applied bias voltage, there is no net flow of current, and hence these persistent edge channels cannot be probed by transport measurement. In the measurement of Fig. 5.1a the authors applied a bias current and thereby manipulated the ratio of the right- and left-flowing charge carriers. The spatial extent<sup>1</sup> of the edge channels is set by the magnetic length  $\ell_B = \sqrt{\hbar/eB}\sqrt{2n+1}$ , which amounts to  $\sim 7$  nm for the  $n=0$  Landau level at  $B = 14$  T and is therefore challenging to resolve with NV magnetometry.

In order for us to map out quantum Hall edges states at lower magnetic fields (our setup has a maximum field of only 0.5 T in all directions), graphene samples with a low number of impurities and high mobility are required. The Schönenberger group<sup>2</sup> is specialized in transport measurements in graphene and fabricated a monolayer graphene Hall-bar (see Fig. 5.2a) that was sandwiched in h-BN and exhibited a mobility of 170'000 cm<sup>2</sup>/Vs. A particularly thin h-BN top-layer ( $\approx 10$  nm) was used to minimize the NV graphene distance. Figure 5.2b shows two-terminal conductance measurements [198] over the contacts indicated in Fig. 5.2a as a function of magnetic field performed in our setup. Quantum Hall plateaus start to appear around a perpendicular field of  $B_z = 250$  mT (blue curve) at  $\sigma_{xy} = 2e^2/h$ . Due to contact resistance, the plateaus do not fully line up with the expected conductance value of  $\sigma_{xy} = (2 + 4n) \cdot e^2/h$ .

We obtained some preliminary current images at a current of  $I = 750$   $\mu$ A and a field of  $B_z = 131$  mT. This was the highest possible field, which still allowed ODMR measurements, as the corresponding NV-ESR resonance frequency was  $\sim 4$  GHz, which was the highest frequency our microwave electronics could provide. Figure 5.2c shows the in-situ AFM data where we indicate the current flow with black arrows. We measured the stray magnetic field above the sample with the NV center and subsequently converted it to a two-dimensional current distribution as depicted in Fig. 5.2d. We observe the highest current density in the constriction of the graphene contacts. Within the Hall-bar the current density is very low since the current distributes over a large area. A direct result is a very low magnetic stray field and long integration times. We also integrated the current density along three lines (blue dashed lines in Fig. 5.2c and d) to obtain the current flow depicted in Fig. 5.2e. This data reveals only a current of  $I \approx 450$   $\mu$ A instead of the expected  $I \approx 750$   $\mu$ A. As we measured the bias current outside the cryostat (see Fig. 5.2a), one explanation for this reduced current are small leakage currents on the way to the graphene flake.

---

<sup>1</sup>Edge state reconstruction causes the spatial extent of the edge states to be greater than the magnetic length. However, in graphene the confinement potential is atomically sharp and edge state reconstruction is avoided [197].

<sup>2</sup>Nanoelectronics group, University of Basel (Switzerland)

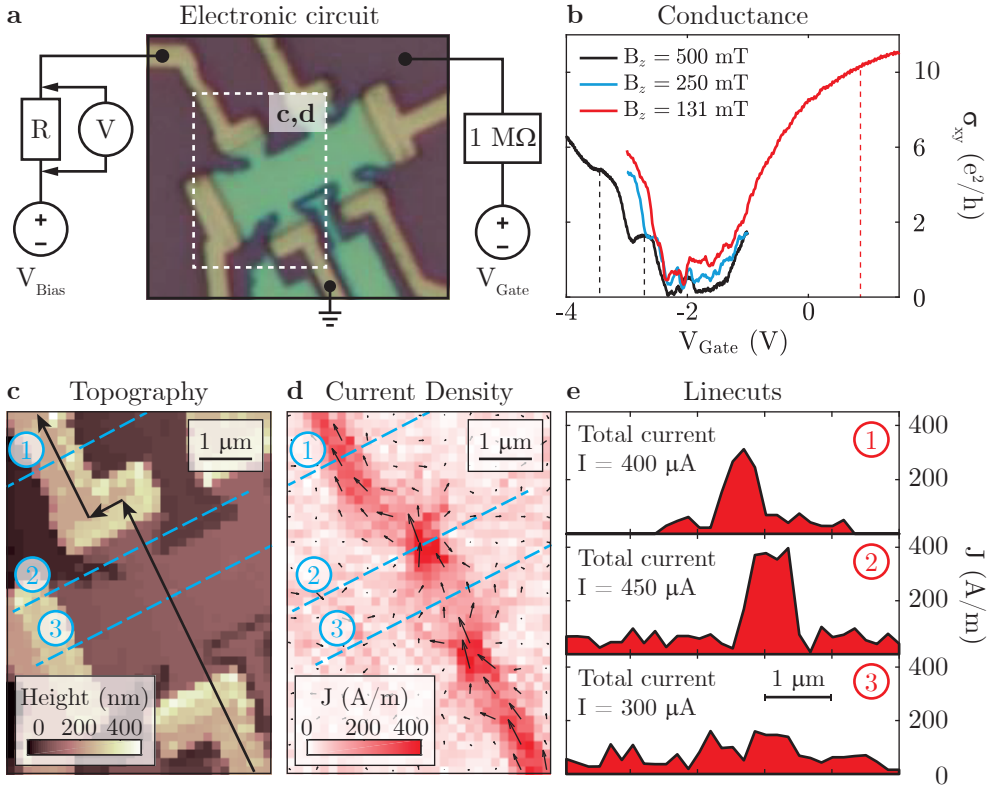


**Figure 5.2.: Current imaging in a graphene Hall-bar.** **a** Electric circuit to apply a constant current to the graphene Hall-bar. We apply a bias voltage  $V_{\text{Bias}}$  to the top left graphene contact and ground the bottom center contact, while all other contacts are floating. Measuring the voltage  $V$  over the resistance  $R$  yields the applied current over the graphene Hall-bar. In addition we apply a gate voltage  $V_{\text{Gate}}$  to tune the Fermi level. The gate voltage is applied via a  $1 \text{ M}\Omega$  resistance to keep leaking currents as small as possible. The dashed, white box indicates the section shown in **c** and **d**. **b** Two-terminal conductance measurements over the same contacts as in **a** at the highest possible field  $B_z = 500 \text{ mT}$  (black),  $B_z = 250 \text{ mT}$  (blue), and  $B_z = 131 \text{ mT}$  (red), which is the field applied in **c** and **d**. We used a bias current of  $I_{\text{Bias}} = 10 \text{ }\mu\text{A}$ . For  $B_z \geq 250 \text{ mT}$  we observed conductance plateaus at voltages indicated by the black, dashed lines, which disappeared at the field applied for the current imaging. The gate voltage used in **c** and **d** was  $V_{\text{Gate}} = 1 \text{ V}$  indicated by the red, dashed line. **c** In-situ AFM data of the graphene Hall-bar. The silicon substrate is the darkest color. On top is the h-BN encapsulated graphene Hall-bar, visible in brown. The current flow is indicated by a black arrow and the position of the current density linecuts with blue, dashed lines. We applied a current of approximately  $750 \text{ }\mu\text{A}$  from the bottom right to the top left contact. **d** Reverse propagated current density  $J$  of the measured field (Appendix A.4) along the NV axis. The measurement was performed in a bias field of  $B_z = 131 \text{ mT}$ . **e** Linecuts of the current density  $J$  along the blue, dashed lines in **c** and **d**. The current density is concentrated on the narrow current line and the contact constriction, while it is very diffuse on the graphene Hall-bar. The integrated current is indicated in the figure.

How feasible is it to image quantum Hall edge currents with NV magnetometry? In the experiment above we applied a huge bias current to get large enough stray fields to detect. These currents lead to strong heating (especially in the ohmic contacts) that will destroy the quantum Hall effect. Luckily, we can drastically decrease them while still maintaining measurable fields if the current density is localized to nanoscale, quasi-1D edge channels. In order to reach this regime, it is vital to verify the existence of edge channels with transport measurements, i.e. verify that the conductance  $\sigma_{xy}$  exhibits plateaus for the given bias current. One edge channel has a resistance of  $h/2e^2 = 12.5 \text{ k}\Omega$ . With the typical best NV sensitivity we can detect a current of  $I = 250 \text{ nA}$ , which then requires a bias voltage of  $V_{\text{Bias}} = 3.1 \text{ mV}$ . This bias voltage corresponds to a temperature  $T = eV_{\text{Bias}}/k = 36 \text{ K}$  (ignoring heating of the contacts), which should not destroy the quantum Hall effect. At a magnetic field of  $B = 500 \text{ mT}$ , the spatial extent of the edge channels is  $\ell_B = 36 \text{ nm}$ . This experiment certainly pushes the limits of the setup in terms of magnetic field strength, sensitivity and spatial resolution. In addition, since transport measurements already proofed the existence of edge channels, only detailed mapping of the spatial profile of the edge currents would reveal new features of the quantum Hall effect, which makes the experiment even more challenging. Still, there is ongoing debate on whether the current flows at the edge of the sample or in the bulk [199]. There is also an alternative experiment, in which highest spatial resolution is not key. As already mentioned, persistent currents in zero bias field cannot be probed by transport measurement and their existence have therefore not been proven. In this scenario measuring magnetic stray fields in presence of the currents is already a strong result. To that end, one records  $\sigma_{xy}$  with a bias current, positions the gate voltage on a plateau to verify edge channels and subsequently floats all contacts. Of course, in this case the magnitude of the current cannot be tuned, but it should be feasible to theoretically estimate it. If it is below our DC sensitivity, one could wiggle the gate voltage and thereby the effective current and detect the fields with a lock-in sequence on the NV center with superior field sensitivity.

A second route to pursue in the future is to look at magnetic stray fields generated by spins and intensify the study of van der Waals magnets. This emerging field has plenty of physics to be discovered, while at the same time a shortage of appropriate sensors exist. In this thesis the quantitative determination of the magnetization of a typical van der Waals magnet was a key achievement. This enables us now to study the dependency of the magnetization on temperature, charge carrier density [152], electric fields [153], and crystal structure [162] and thereby further our understanding of the material. While these measurements do not require the nanoscale resolution of our sensor, it will be essential for the study of localized magnetic structures like domain walls [142, 154] or skyrmions [180] as well as the creation, manipulation, and mobility thereof.

In addition to measurements of static spin textures, we can detect magnetic fluctuations of spins in these novel materials. To that end, we will harness the AC sensing capability of the NV center, which emphasizes its broad application spectrum as a magnetometer – a feature that has not been used in this thesis at all. Different pulsing techniques allow us to cover the dynamic frequencies from MHz to GHz. While it is difficult to sense magnetic signals in the kHz-range, dynamical decoupling sequences applied to the NV center can be used to cover the MHz-range. In these measurements

the NV spin state is initialized in a superposition of  $|m_s = 0\rangle$  and  $|m_s = \pm 1\rangle$ , and free evolution periods are intercepted by microwave  $\pi$ -pulses. The sequence serves as a band-pass filter and is mostly sensitive to fields at the frequency of spin-inversion. The lower frequency bound of this technique is  $\sim 0.1$  MHz given by the spin coherence time of the NV center, which in our devices is around  $T_2 \approx 10$  us. The upper bound is  $\sim 1$  GHz given by the minimum technically achievable pulse length. Magnetic field noise in the GHz-range can be probed by longitudinal relaxometry experiments. To that end, the NV center is initialized and the spin population is monitored as a function of time. This technique is directly sensitive to frequencies at the  $|m_s = 0\rangle$  to  $|m_s = \pm 1\rangle$  spin transition frequencies, which can be tuned using static magnetic fields.

Particularly exciting applications of AC sensing with the NV center was reported in the field of magnonics. While high-frequency spin-waves in the THz-range can be detected using inelastic tunneling spectroscopy [200] or neutron scattering [175], a suitable tool in the GHz-range, which is relevant for 2D magnetic materials, was long missing. NV magnetometry emerged as a promising sensor in this new territory with first demonstrations. T. van der Sar *et al.* measured driven spin excitation in a ferromagnetic microdisk, which led to the amplification of the drive field and, hence, a measurable power broadening of the ODMR lines and speedup of the NV Rabi oscillations [20]. A comparison of the NV relaxation rate with and without driving the spin-waves even allowed the extraction of the spin chemical potential and to gain insight into the magnetic excitation spectrum [21]. This clearly demonstrates the potential to also study spin transport properties via the application of a chemical potential imbalance and renders the NV center more than ever a highly promising quantum sensor. If we succeed to add these features to our NV's portfolio of nanoscale and quantitative field sensitivity at cryogenic temperatures, we can readily establish magnonics in van der Waals magnets.





# A. Appendix

## A.1. NV magnetometry

### A.1.1. Fabrication of NV cantilevers

The fabrication of diamond cantilever is an essential and indispensable part enabling the work presented here. A detailed description of our original recipe to fabricate all-diamond cantilevers out of a 50  $\mu\text{m}$  thin diamond slab is published in [37]. Based on this recipe, we developed a few improvements that facilitate the fabrication and improves the yield of cantilevers. In order to understand them, I will summarize the original recipe in a few words.

1. After the creation of shallow NV centers with an average NV-NV distance of 200 nm, a region at the edge of the diamond is thinned down from 50  $\mu\text{m}$  to about 3  $\mu\text{m}$ . The size of the diamond membrane typically is 600  $\mu\text{m}$   $\times$  300  $\mu\text{m}$ .
2. Cantilevers (3  $\mu\text{m}$   $\times$  10  $\mu\text{m}$ ) are transfered into the diamond from the NV remote side of the diamond.
3. 2  $\mu\text{m}$  tall pillars with a diameter of 200 nm and straight side walls are transfered into the diamond. This step releases the cantilevers from the bulk diamond.

In the following we will highlight the modifications to this recipe. We start with a 50  $\mu\text{m}$  thick diamond with implanted NV centers as in the original recipe.

1. Cantilevers are etched as a first step. The cantilever footprint is increased to 10  $\mu\text{m}$   $\times$  20  $\mu\text{m}$ , which facilitates the break out of the cantilevers and alignment to the scan plane. Due to the use of a conducting protective coating (Electra 92) on top of our etch mask, we could use three times higher aperture in the e-beam step, which results in a 10 times faster writing time.
2. In a subsequent step, we etch pillars into the diamond. As the diamond is still 50  $\mu\text{m}$  thick, it is mechanically more stable (less vibrations) and pillar etch masks adhere better to the diamond resulting in a higher yield. In addition, the pillars are written and etched from the same side as the cantilevers facilitating the alignment of the pillar pattern to the cantilever pattern.  
The writefield for the cantilevers and pillars is usually 1 mm  $\times$  1 mm and, hence, much larger than the diamond membrane in the original recipe which results in more cantilevers per fabrication. In our approach, we can write multiples fields on the diamond and etch them in parallel further increasing the yield.
3. In a last step we define an etching window with four quartz plates and perform a 50  $\mu\text{m}$  deep etch to release the cantilevers.

The following list points out the advantages (+) and disadvantages (-) of the modifications to the original recipe.

- The deep etch is the last step of the process
  - + The handling throughout the nanofabrication process is very easy as the diamond is thick ( $50\text{ }\mu\text{m}$ ).
  - + Pillars are written on thick diamond that is mechanically more stable (less vibrations) and pillars etch mask adhere better to the diamond resulting in a higher yield.
  - + Since the pillars are written first, the NVs in the pillars can be characterized before the critical deep etch.
- The cantilever pattern is written inside the diamond and not on an edge
  - + The thin membrane is well protected from thick diamond from all four sides.
  - + This facilitates the handling of the diamond as one can tweeze the diamond from all sides.
  - + One can have multiple writefields on a single diamond at the same time, whereas before one was restricted to one thin membrane at the edge (parallel process)
  - + The membrane can have a larger size due to higher stability, as it is clamped now by four side walls compared to three before. Therefore, the number of cantilevers per membrane is larger.
  - + In the original recipe, a diamond wall builds up at the edge of the diamond, which needs to be broken away. This poses a potential threat to the thin membrane. In the modified recipe this step is eliminated.
  - + No complicated two-sided alignment.
  - + One has not to spin resist on a membrane inside the diamond.
    - The thickness of the membrane is hard to estimate and is currently done with laser scanning confocal microscope and interference colors during etching.
    - The cantilevers must not be too thick as one has to spin resist on top of them for the pillar process.

One major advantage is certainly that the deep etch is done in a last step and, hence, at no time during the fabrication (that involves way more steps than described here) a thin membrane needs to be handled or spun on. Figure A.1 shows an optical image of a fabricated device. Cantilevers in two write fields have been released with a deep etch while the remaining two can be released at any time. The cantilevers are much better protected in our approach as a  $50\text{ }\mu\text{m}$  thick diamond wall protects them from all four sides in comparison with the original approach.

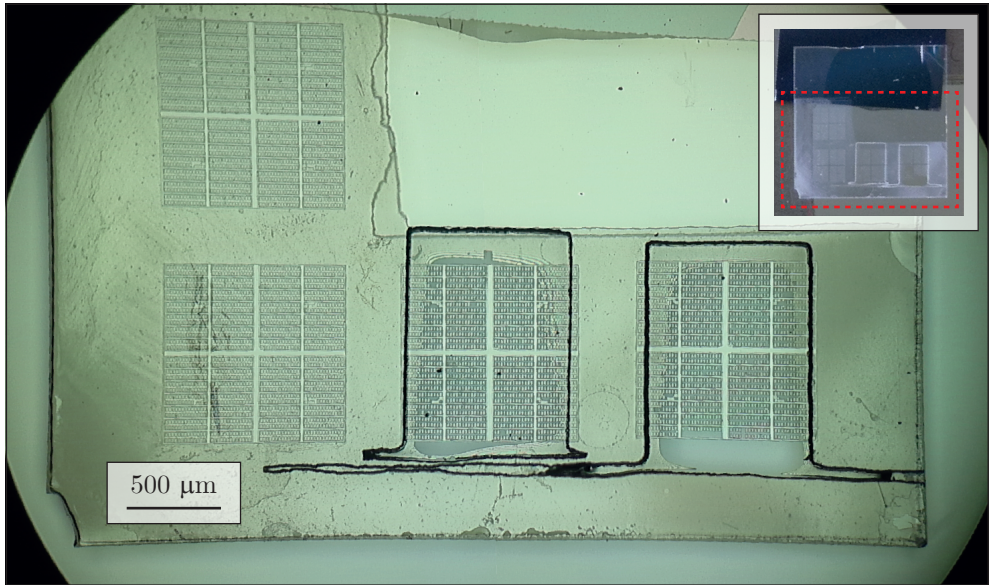


**Figure A.1.: Optical image of fabricated scanning probes in diamond.** Top view of a diamond that was fabricated using the modifications to the original recipe as described in the text. The inset shows the whole square diamond with the section of the main image outlined with the red, dashed box. The two right writefields are deep-etched and the scanning probes are released while the two leftmost patterns are still part of the 50  $\mu\text{m}$  thick diamond slab.

### A.1.2. History of deployed NV cantilevers

This section gives a brief history of the diamond cantilevers<sup>1</sup> used during the thesis. The lifetime in days indicates how long the cantilever approximately had been mounted in the setup. This number does not necessarily corresponds to the number of days the device was actually used for scanning.

#	Diamond batch	Lifetime (days)	Cycles to 4 K	Replacement reason
1	A	14	0	Glue point broke during AFM scan
2	A	20	0	Glue point broke during AFM scan
3	A	4	1	Broke during AFM approach
4	A	3	1	Got replaced by better device
5	A	6	1	Tuning fork broke due to operator failure
6	B	14	1	Pillar broke during AFM scan
7	B	21	1	NV bleached
8	B	13	1	Cantilever gone after warm up
9	B	97	3	Charging effect (?)
10	B	22	1	Pillar broke during AFM scan
11	B	34	2	Pillar broke off
12	B	6	1	Tuning fork broke due to operator failure
13	C	10	1	Blinking NV
14	C	60	2	Cantilever gone, unclear
15	D	11	1	NV bleached
16	E	1	0	Cantilever gone after pumping
17	E	62	1	NV bleached
18	D	9	1	NV <sup>-</sup> turned into NV <sup>0</sup>
19	E	3	0	NV bleached
20	C	10	0	Glue (?) around pillar
21	C	7	?	?
22	C	9	1	NV <sup>-</sup> turned into NV <sup>0</sup>
23	F	50	2	Pillar picked up gold contact
24	F	52	3	Pillar picked up fluorescing material
25	G	60	3	No special reason, NV still alive
26	G	63	1	Replaced by single NV cantilever
27	G	210	7	Pillar broke during AFM scan

<sup>1</sup>The list was composed in all conscience but may not be complete or 100% correct

### A.1.3. SEM images of broken cantilever devices

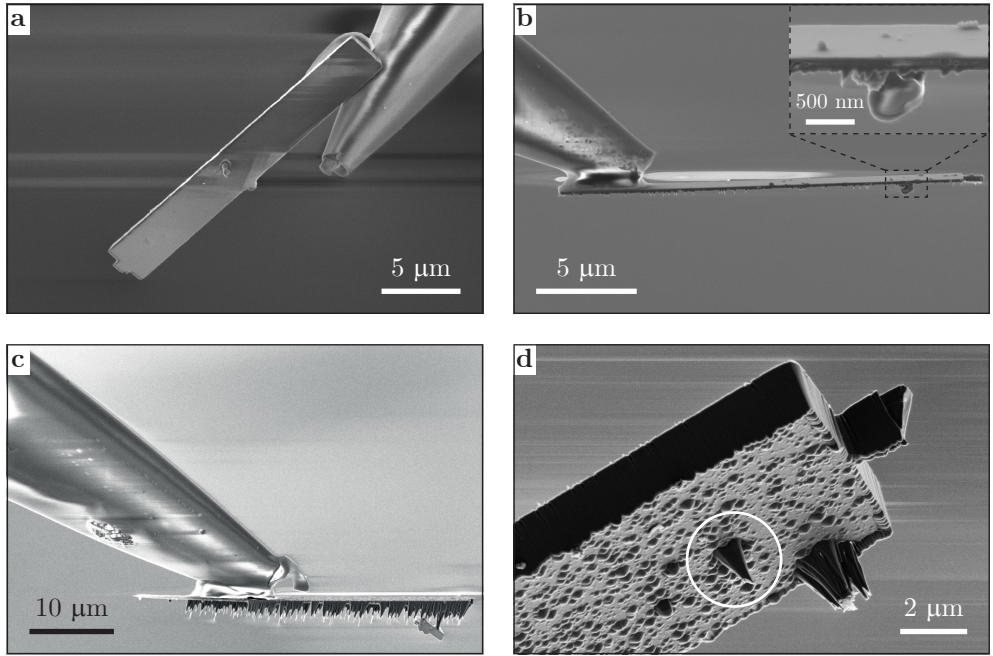


**Figure A.2.: Scanning electron microscope (SEM) images of broken cantilever devices.** **a** Most likely an electrostatic charging effect detached the cantilever and is holding it to the quartz rod. Interestingly, the binding was strong enough to survive multiple days of AFM scanning and a warm-up cycle from 4 K to room temperature. One can see the pillar near side of the cantilever and the gluing point of the quartz top on the far side on the right end. This is cantilever #9 in Tab. A.1.2. **b** An unknown material (likely polymer residues or UV glue) was picked up during scanning over a graphene Hall-bar, which covers the complete pillar. This is cantilever #20 in Tab. A.1.2. **c** A gold ohmic contact was scratched off from a graphene Hall-bar during AFM scanning. After the pick-up, the AFM performance increased as the tip got a sharper ending. This is cantilever #23 in Tab. A.1.2. **d** The pillar (encircled) broke half-way when scanning over a bubble on a  $\text{CrI}_3$  sample. This is cantilever #27 in Tab. A.1.2.

### A.1.4. General remarks on Fourier-space propagation

The transformations discussed above are all performed in Fourier space. An alternative approach emphasizing real space transformation exists and is published in [46]. The advantage of a real space transformation is that we do not need the knowledge of the magnetic field at all points on a surface and we do not impose conditions on the magnetic field spatial distribution, such as assuming the magnetic field is zero at the boundaries of the map. The advantage of the Fourier transformation is that we do

not need to evaluate complicated integrals (convolutions) but simply need to multiply matrices. This is not a computationally intensive task and is therefore much faster and requires less computation power.

In the transformations presented in Sec. 2.2, we can observe a singularity and break down at  $k = 0$ . Hence, any information associated with  $k = 0$ , i.e. DC offsets, cannot be retrieved. This is not surprising, since Eq. (2.19) or (2.20) involve only first-order derivatives of the magnetic field.

All the derivations in Sec. 2.2 are correct if one knows the field in an infinitely extended scan plane. In an experiment, however, the scan range is finite and the field map is discretized. In general, we advise to use scan ranges that are larger than the sensor sample distance and the spatial dimensions of the magnetic field source. If the scan range, however, does not contain all field sources, the measured field is affected by field sources outside the measurement window. Without making assumption on these source, the reverse propagation cannot provide accurate and unique solutions. Mathematically, the recorded field map is a multiplication with a rectangular window function in real space, which leads to a convolution with a sinc function in Fourier space causing erroneous frequency components to appear. To minimize the resulting errors, we smooth the rectangular window function by extending the magnetic field map outwards with a Gaussian function, which leads to a decay of the field at the edge towards zero. More sophisticated methods, i.e. periodic boundary conditions, to circumvent this issue are given in [201].

In the case of discretized field maps, an undersampling can lead to information loss. Ideally one samples the field map as finely as possible, since it is still possible to discard samples in a post-process or average multiple pixels together to a coarser grid. Experimental constraints may limit sampling though, and we therefore recommend to sample the scan with a pixel size smaller than the expected spatial resolution of the sensor. A simple test to check if the sampling frequency is high enough is to check whether the magnitude of the spectrum at the highest spatial frequencies is close to zero.

Most programming languages have already integrated algorithms for Fourier transforms. However, these algorithms usually only return the intensity of the Fourier transform without the corresponding  $k$ -vectors. In order to have the proper weights at each spatial frequency, it is vital that the  $k$ -space is sampled the same way, the FFT algorithm samples the spectrum of the field map, meaning that the  $k$ -space constructed by the user matches the  $k$ -space of the algorithm. A non-negligible imaginary component from an inverse FFT is a good indication that the  $k$ -space is not correct [53]. For Matlab, an example code to calculate the wavenumber coordinates is given in Appendix A.5.1.

Another source of error is under-sampling of the spectrum by the FFT algorithm. This issue can be tackled by zero-padding techniques as illustrated in Fig. A.3. A good strategy for the right amount of zero-padding is doubling the number of zero padding in each dimension and to check if the result has noticeable changes. We keep going only until no significant differences are observed, to avoid excessive computation and high memory requirements. To speed up processing time, we also advise to zero-pad all involved matrices such that the number of entries in each dimension is a power of two.

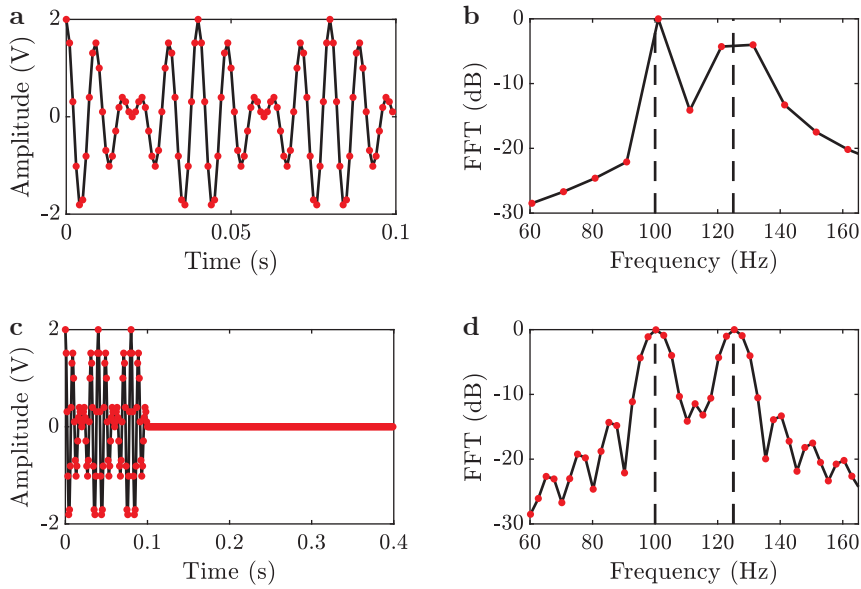


**Figure A.3.: Zero-padding of data for Fourier transform.** **a** Signal of the form  $f(t) = \cos(2\pi\nu_1 t) + \cos(2\pi\nu_2 t)$  with oscillation frequencies  $\nu_1 = 100$  Hz and  $\nu_2 = 125$  Hz, respectively. The sampling rate is 1 kHz and the total duration is  $T = 0.1$  s. **b** FFT of signal in **a**. The frequency resolution and the FFT resolution are both  $1/T = 10$  Hz. Hence, the 100 Hz signal is nicely resolved, whereas the 125 Hz peak is distributed over the 120 Hz and 130 Hz frequency with lower amplitude. **c** Same graph as in **a** with zero-padding of three times the duration time up to a new total duration of  $T_{\text{new}} = 0.4$  s. **d** The frequency resolution is improved to  $1/T_{\text{new}} = 2.5$  Hz. Both, the 100 Hz and 125 Hz signal are now well reproduced displaying the need for zero-padding. It is important to note, that the FFT resolution is still limited by  $1/T = 10$  Hz, which is the FWHM of the resonance peaks.

### A.1.5. Pulsed experiments and field dependent ODMR contrast

The cryogenic NV magnetometry setup has fully met the expectations so far, but one major issue has to be debugged in the near future. While continuous microwave driving, i.e. ODMR, is working, arbitrary spin manipulation is currently not possible. A nice illustration of that fact is given in Fig. A.4a. In red we show Rabi oscillations of the NV center and in blue we show spin inversion via adiabatic fast passage (AFP) [202]. There we optically initialized the NV center in its  $|m_s = 0\rangle$  state and subsequently sweep a microwave frequency over the NV resonance. Since AFP is a quasi-continuous MW experiment, we fully understand this data and read off the normalized fluorescence of the  $|m_s = -1\rangle$  sublevel. In this case,  $|m_s = -1\rangle$  is 23% darker than  $|m_s = 0\rangle$ . On the other side, the pulsed spin inversion experiment, i.e. the Rabi experiment, gives a fluorescence contrast of only 12%. This indicates an incomplete spin inversion and therefore an imperfect  $\pi$ -pulse. The most likely cause for this issue are deformation of the MW pulses as they travel long distances to

the MW antenna through the cryostat. Since proper pulses are a prerequisite for all AC magnetometry applications [13], a careful analysis of the MW setup is required starting with the characterization of transmitted microwave pulses.

Another, not yet understood phenomenon is magnetic field dependent ODMR contrast. While the ODMR contrast is only  $\sim 5\%$  for  $|B_{\text{NV}}| < 100$  mT, it suddenly increases by a factor of three above this threshold. The experimental data is displayed in Fig. A.4b. Since we are not aware of any NV related mechanism that can explain this phenomenon, we are inclined to assign it to hardware specifics of the setup, which are to be investigated.

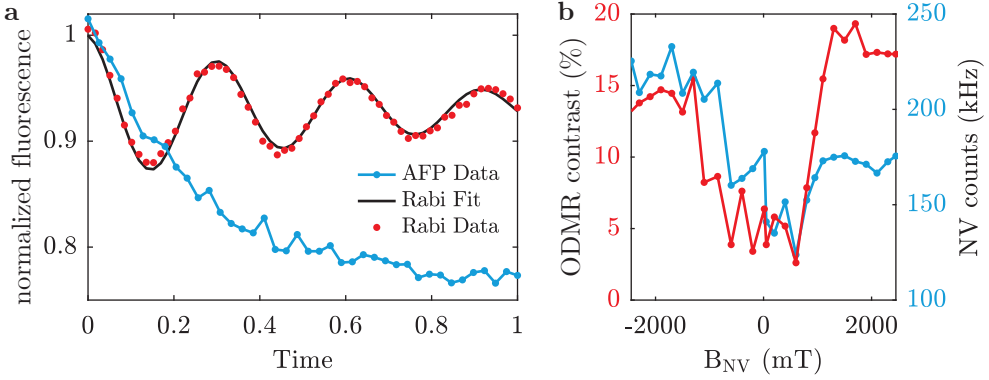


**Figure A.4.: Complication with pulsing experiments and magnetic field dependent ODMR contrast.** **a** While adiabatic fast passage (AFP)(blue) gives an optical contrast of 23% between the  $|m_s = 0\rangle$  and  $|m_s = -1\rangle$  magnetic sublevel, a Rabi experiment (red) only gives a contrast of 12% indicating incomplete Rabi oscillations. The Rabi frequency in the AFP experiment was  $\omega_R = 2$  MHz, the detuning  $\delta(t = 0) = 100$  MHz, and the total pulse duration  $T_p = 20 \mu\text{s}$ . For the Rabi experiment the longest pulse duration was 800 ns. **b** The graph shows ODMR contrast (red) and NV counts (blue) as a function of background field along the NV axis. At high magnetic fields ( $> 100$  mT) the ODMR contrast is three times the contrast at low fields. The origin of this phenomena is unknown.



## A.2. Superconductivity

### A.2.1. Flux quantization

Magnetic flux in superconductors has to be quantized, which is apparent when we consider the second Ginzburg-Landau equation Eq. (3.5). We take the line integral of Eq. (3.5)

$$\oint \mathbf{J} dl = \frac{2e}{m^*} |\psi|^2 \oint (\hbar \nabla \Theta - 2e \mathbf{A}) dl, \quad (\text{A.1})$$

and rearrange it to obtain

$$\frac{m^*}{4e^2 |\psi|^2} \oint \mathbf{J} dl + \oint \mathbf{A} dl = \frac{\hbar}{2e} \oint \nabla \Theta dl, \quad (\text{A.2})$$

where  $\oint \mathbf{A} dl = \Phi$  is the magnetic flux and  $\oint \nabla \Theta dl \stackrel{!}{=} n \cdot 2\pi$  ( $n \in \mathbb{Z}$ ) due to the continuity of the wavefunction of the order parameter. Hence, we obtain with the magnetic flux quantum  $\Phi_0 = h/2e$

$$\frac{m^*}{4e^2 |\psi|^2} \oint \mathbf{J} dl + \Phi = n \Phi_0. \quad (\text{A.3})$$

This equation predicts that flux penetrating the superconductor long distance away from an edge compared to  $\lambda_L$ , where the current  $J = 0$ , must be quantized with the smallest flux possible i.e. the flux quantum  $\Phi_0$ .

### A.2.2. Determination of stray field sign in NV magnetometry

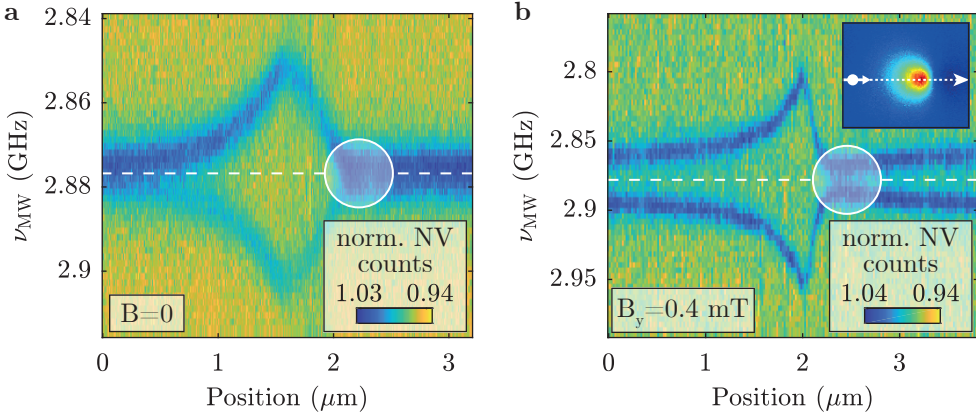


**Figure A.5.: Determination of stray field sign for line scans over a vortex.**

The data shows the ODMR spectrum ( $y$ -axis) at every position ( $x$ -axis) along a line scan over a vortex (see inset in **b**). **a** In zero bias field, the stray field and hence the ODMR splitting goes to zero far from the vortex while it increases at the position of the vortex. The field is extracted by fitting two Lorentzians at every position to the ODMR spectrum. In the region encircled in white, we expect a negative stray field due to the projection of the stray field onto the NV axis and a crossing of the ODMR resonances. However, this is not visible and therefore the sign of the stray field cannot be determined. **a** In a bias field of  $B_y = 0.4$  mT, both ODMR resonances are split even at zero stray field and can be clearly distinguished in the white encircled region allowing for sign determination.

### A.2.3. Numerical implementation of vortex stray fields

This section deals with the numerical implementation of the Pearl and Carneiro model and was mostly executed by my fellow student Dominik Rohner.

#### A.2.3.1. Pearl vortex

The stray field reads [67, 91]

$$\mathbf{B} = \nabla \times \mathbf{A}_\varphi(r, z) = \nabla \times \left( \frac{\Phi_0}{2\pi} \int_0^\infty \frac{J_1(qr)e^{-q|z|}}{1 + \Lambda q} dq \right), \quad (\text{A.4})$$

where we can write the curl of  $A$  in spherical coordinates as

$$\begin{aligned} \nabla \times \mathbf{A}_\varphi &= \left[ \frac{1}{r} \frac{\partial \mathbf{A}_z}{\partial \varphi} - \frac{\partial \mathbf{A}_\varphi}{\partial z} \right] \mathbf{e}_r + \left[ \frac{\partial \mathbf{A}_r}{\partial z} - \frac{\partial \mathbf{A}_z}{\partial r} \right] \mathbf{e}_\varphi + \frac{1}{r} \left[ \frac{\partial}{\partial r}(r \mathbf{A}_\varphi) - \frac{\partial \mathbf{A}_r}{\partial \varphi} \right] \mathbf{e}_z \\ &= \left[ -\frac{\partial \mathbf{A}_\varphi}{\partial z} \right] \mathbf{e}_r + \left[ \frac{1}{r} \frac{\partial}{\partial r}(r \mathbf{A}_\varphi) \right] \mathbf{e}_z \end{aligned} \quad (\text{A.5})$$

with

$$\mathbf{B}_r = -\frac{\partial \mathbf{A}_\varphi}{\partial z} = q \mathbf{A}_\varphi \quad (\text{A.6})$$

$$\mathbf{B}_z = \frac{1}{r} \frac{\partial}{\partial r}(r \mathbf{A}_\varphi) = \frac{\mathbf{A}_\varphi}{r} + \frac{\partial \mathbf{A}_\varphi}{\partial r}. \quad (\text{A.7})$$

Only the Bessel function in Eq. (A.4) depends on  $r$  and its derivative is

$$\frac{\partial J_1(qr)}{\partial r} = q J_0(qr) - \frac{J_1(qr)}{r}. \quad (\text{A.8})$$

If we insert Eq. (A.8) into Eq. (A.7), the term  $\mathbf{A}_\varphi/r$  drops out and we obtain

$$\mathbf{B}_z = \frac{\Phi_0}{2\pi} \int_0^\infty \frac{q J_0(qr)e^{-q|z|}}{1 + \Lambda q} dq. \quad (\text{A.9})$$

The integrals in Eq. (A.6) and Eq. (A.9) were numerically integrated using MATLAB's *integral* function. Instead of integrating to  $\infty$ , we set the upper integration limit to the a value, where the integrand converges. The integrand is proportional to  $(1 + \Lambda q)^{-1}$  and goes to 0 for  $q = n/\Lambda$ , where  $n$  is a large number. As discussed in the main text, the stray field of a vortex decays on the length scale of  $\Lambda$ , which justifies to set the upper limit of the integral to a multiple of the inverse penetration depth. We chose the number of sampling points such that we cover one wavelength of the Bessel functions with at least 4 points.

#### A.2.3.2. Carneiro vortex

The stray field reads [68]

$$\begin{aligned} B_z(r, z_{\text{NV}}) &= \frac{\phi_0}{2\pi\lambda_L^2} \int_0^\infty dk \frac{k J_0(kr)}{k^2 + \lambda_L^{-2}} f(k, z_{\text{NV}}) \\ B_r(r, z_{\text{NV}}) &= \frac{\phi_0}{2\pi\lambda_L^2} \int_0^\infty dk \frac{J_1(kr)}{k^2 + \lambda_L^{-2}} g(k, z_{\text{NV}}), \end{aligned} \quad (\text{A.10})$$

with the functions  $f$  and  $g$  defined in Eq. (3.14). The integrals were numerically evaluated using MATLAB's *integral* function on the interval  $[0, n/\lambda_L]$  with the same argumentation as provided in Sec. A.2.3.1

#### A.2.4. Magnetic field data

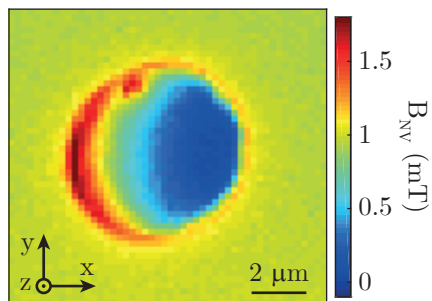


**Figure A.6.:** Data set of measured  $B_{NV}$  map of a superconducting YBCO disk in a perpendicular magnetic field. a Quantitative map of the magnetic field  $B_{NV}$ , measured with the scanning NV spin above the YBCO disk in an external magnetic field of 1.7 mT applied perpendicular to the sample. The observed absence of rotational symmetry of  $B_{NV}$  around the disk center is a result of the NV orientation being away from the sample normal. This data set was transformed to  $B_z$  shown in Fig. 3.13.

## A.3. Two-dimensional magnetic systems

### A.3.1. Characterization of $\text{CrI}_3$ samples

This section gives a detailed overview of the sample geometry and relevant characterization data for each device fabricated. For each sample we present an optical image of the flake before and after encapsulation, a two-dimensional topography map as well as a topography line scan to characterize the sample thickness. As the shape of the flakes got distorted during the encapsulation process and is hard to be recognized in the subsequent optical images, we also show iso-magnetic scans measured with the NV center for clarity.

Device D1 consists of a very large and nicely homogeneous flake of a bi- and trilayer  $\text{CrI}_3$ . In the optical image of the encapsulated sample (see Fig. A.7a) a darker region of four layers is visible. Unfortunately, this region was destroyed after encapsulation during AFM measurements and therefore not accessible any more. This sample allowed us to quantitatively examine the odd-even effect in  $\text{CrI}_3$ .

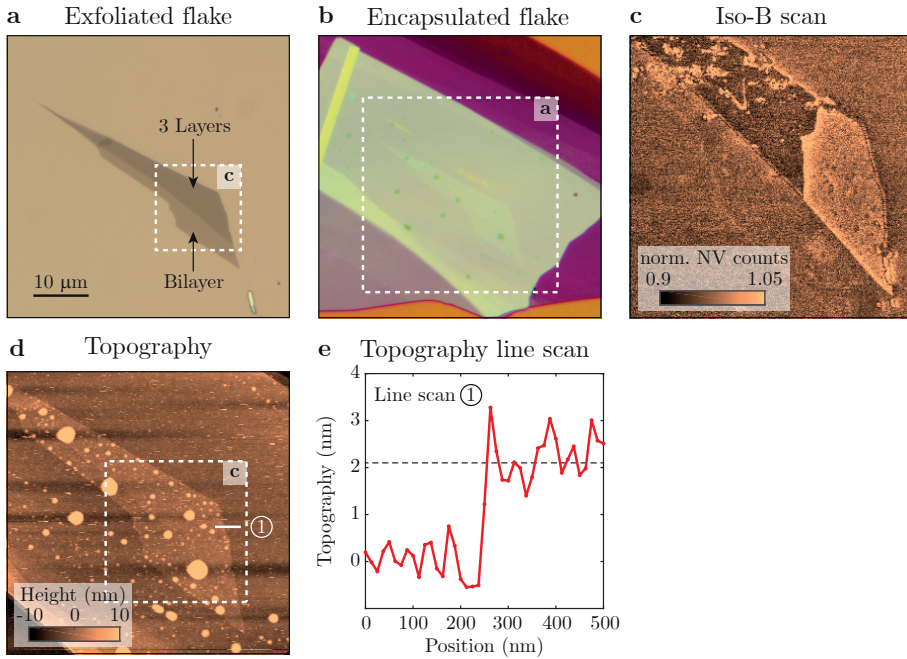


**Figure A.7.: Characterization of sample D1 consisting of a bi- and trilayer of  $\text{CrI}_3$ .** **a** Optical image of the exfoliated flake. **b** Optical image after encapsulation with graphene. **c** Iso-field image ( $B_{\text{iso}} = 0.12$  mT, integration time 0.2 s/pixel) of the section illustrated with the white dashed box in **a** and **d**. Note that the three layer flake features a domain wall, which will be discussed in Sec. 4.6. **d** Ex-situ AFM data of the encapsulated sample. **e** Line scan of the topography over the three layer edge as indicated in **d**. The theoretical height value for a three layer flake (2.1 nm) is displayed as a dashed line.

Device D2 consists of a 5- and 9-layer flake of  $\text{CrI}_3$ . In this sample we observed a clear connection between the stacking order of the individual layers and the magnetic coupling between them (see Sec. 4.4).

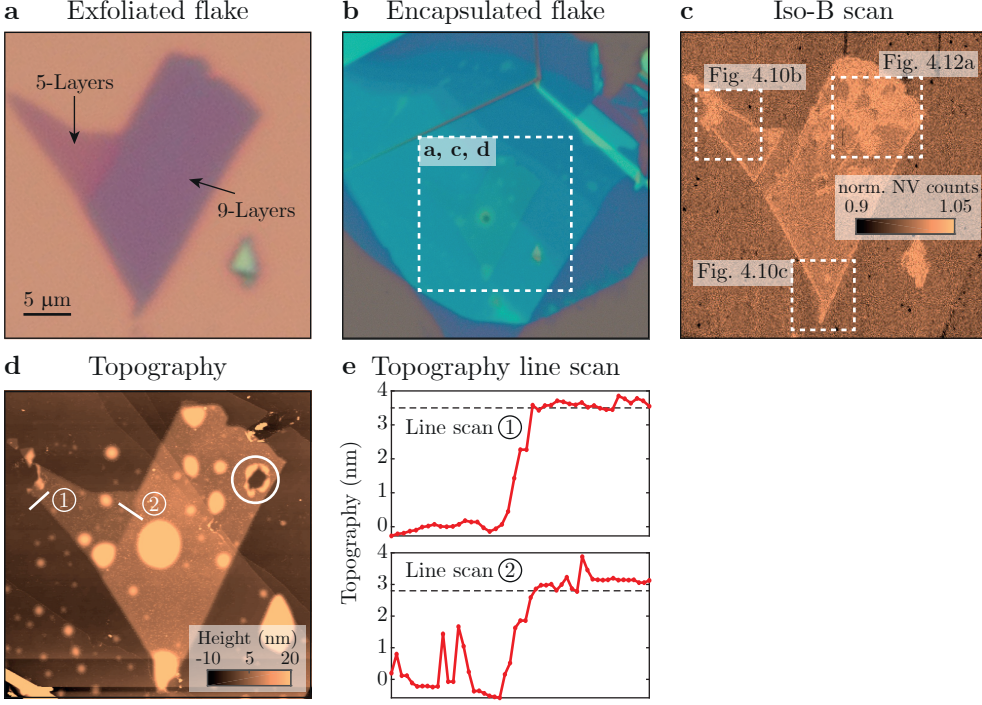


**Figure A.8.:** Characterization of sample D2 consisting of five and nine layers of  $\text{CrI}_3$ . **a** Optical image of the exfoliated flake. **b** Optical image after encapsulation with h-BN. **c** Iso-field image ( $B_{\text{iso}} = 0$ , integration time 0.18 s/pixel) of the section illustrated with the white dashed box in **b**. The scan sections of Fig. 4.7b, Fig. 4.7c and Fig. 4.9a in the text are indicated. **d** Ex-situ AFM data of the encapsulated sample after the puncture of the hole (white circle), which is discussed in Sec. 4.4. **e** The top panel shows the line scan of the topography over the five layer edge as indicated in **d**. The theoretical height value for a five layer flake (3.5 nm) is displayed as a dashed line. The bottom panel shows the line scan of the topography over the five to nine layers edge as indicated in **d**. The theoretical height value for four layer (2.8 nm) is displayed as a dashed line.

Device D3 consists of a mono- and bilayer flake of  $\text{CrI}_3$  next to two very thick flakes. This sample allowed us to proof quantitatively that a single isolated layer of  $\text{CrI}_3$  features inherent magnetism, which is a major finding of this chapter.

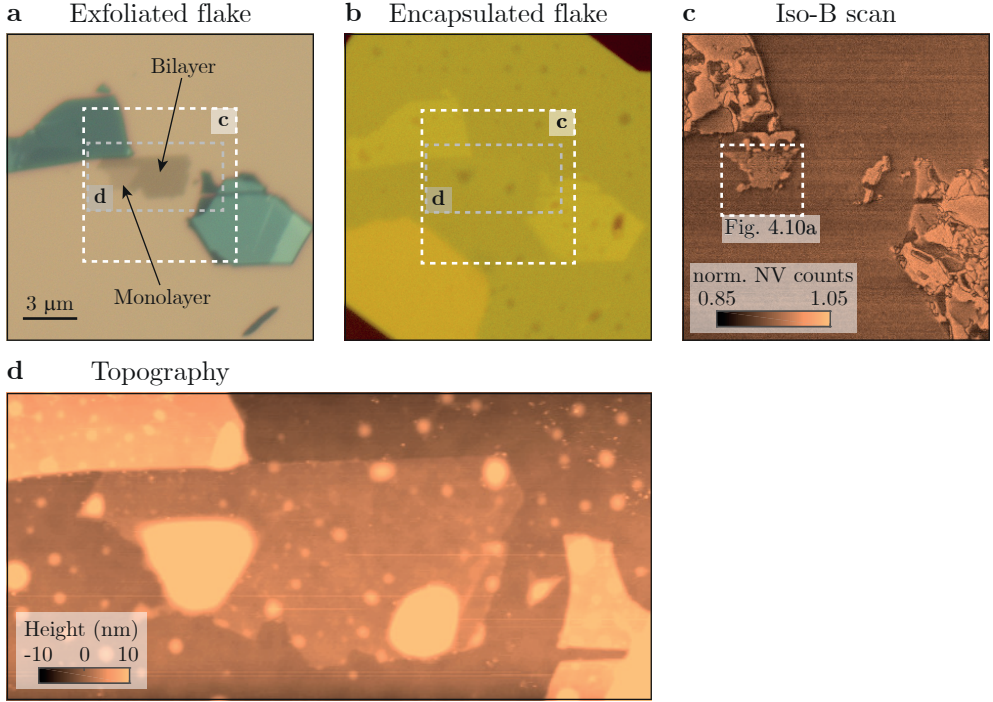


**Figure A.9.: Characterization of sample D3 consisting of a mono- and bilayer of  $\text{CrI}_3$ .** **a** Optical image of the exfoliated flake. **b** Optical image after encapsulation with graphene. The same section of the sample is shown as in **a**. **c** Iso-field image ( $B_{\text{iso}} = 0.27$  mT, integration time 0.8 s/pixel) of the section illustrated with the white dashed box in **a** and **b**. Magnetic signal from the thick flakes as well as the monolayer sample is clearly visible while no magnetic signal emerges from the bilayer. The scan section of Fig. 4.7a is indicated. **d** Ex-situ AFM data of the encapsulated sample of the section illustrated with the gray dashed box in **a** and **b**.

### A.3.2. Direct measurement of the magnetization

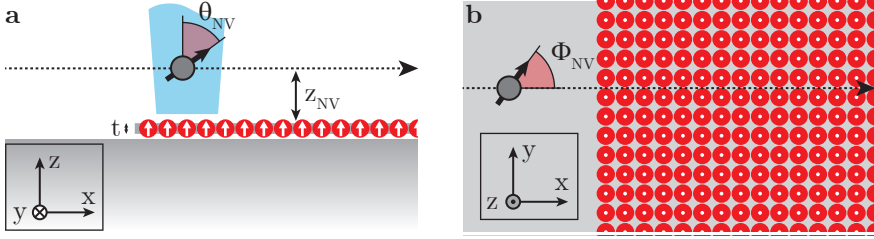


**Figure A.10.: Schematic of the setup for direct measurement of magnetization.** **a** Side view of the schematic. An NV center is scanned at a height  $z_{\text{NV}} \gg t$  over the edge of an uniformly magnetized ferromagnet, where  $t$  is the sample thickness. The NV center lies at an angle  $\theta_{\text{NV}}$  with respect to the  $z$ -axis. **b** Top view of the same situation. The NV center has an angle  $\phi_{\text{NV}}$  with respect to the  $x$ -axis.

An analytical approach to infer the uniform magnetization  $\sigma_z$  in ultra-thin ferromagnetic films with perpendicular anisotropy from NV magnetometry was recently demonstrated [17, 171]. The stray field is measured along a line perpendicular to the sample's edge, as illustrated in Fig. A.10. The stray field is caused by the variation of the out-of-plane magnetization that arises from the edge of an out-of-plane magnetized film. The field contains all relevant information needed to extract the magnetization of the sample (i.e. the stray field amplitude is directly proportional to the magnetization) and its analytical formula is

$$\begin{aligned} B_x(x) &\approx \frac{\mu_0 \sigma_z}{2\pi} \frac{z_{\text{NV}}}{x^2 + z_{\text{NV}}^2} \\ B_z(x) &\approx -\frac{\mu_0 \sigma_z}{2\pi} \frac{x}{x^2 + z_{\text{NV}}^2}, \end{aligned} \quad (\text{A.11})$$

where  $\mu_0$  is the vacuum permeability. Equation A.11 is an approximation and only valid in the thin film limit (film thickness  $t \ll z_{\text{NV}}$ ) for an infinitely long sample edge along the  $y$ -axis and for a purely out-of-plane magnetization. Assuming the stray field component transverse to the NV axis remains small, so that the Zeeman splitting is linear with the longitudinal component ( $g\mu_B B_{\text{NV}} \ll hD$ ), one can extract a value for both the magnetization  $\sigma_z$  and the NV sample distance  $z_{\text{NV}}$  by fitting the measurement data of the line scan to

$$B_{\text{NV}} = \cos(\phi_{\text{NV}}) \sin(\theta_{\text{NV}}) \cdot B_x + \cos(\theta_{\text{NV}}) \cdot B_z \quad (\text{A.12})$$

for known NV angles  $(\phi_{\text{NV}}, \theta_{\text{NV}})$ . The field maximum scales as  $\sigma_z/z_{\text{NV}}$  and the characteristic width is given by  $2z_{\text{NV}}$ . An application of the equation is shown in the lower panel of Fig. 4.7.

As Eq. (A.11) depends on a number of parameters, a discussion of potential uncertainties is indispensable. Measurements with the NV center do not directly yield the magnetic field but rather the experienced Zeeman splitting, which can be converted to a magnetic field (see Eq. (2.1)). Hence, critical parameters are the zero field splitting  $D$ , the transverse zero-field splitting  $E$  and the NV orientation  $(\phi_{\text{NV}}, \theta_{\text{NV}})$ . The



first two parameters can be deduced from an ODMR spectrum in zero field. The NV orientation can be deduced from magnetic field alignment procedures using vector magnets with uncertainties of a few degrees [59].

Further, the fit depends on the topography, i.e. sample thickness  $t$ , which modifies the effective NV sample distance  $z_{\text{NV}}$  as one scans the NV center across the sample border. As we were working with a true 2D system, we ignored the height variations. Also Eq. (A.11) is only valid for ideal infinitely long straight borders.  $\text{CrI}_3$  flakes, however, do not have straight edges, and their edges are obviously not infinitely long. Whenever we extract  $z_{\text{NV}}$  from a fit to data, the calibration of the displacement along the x-axis is an important quantity. The scanners used are calibrated, but their displacement can change over time. A smaller (larger) displacement-to-voltage ratio would lead to an under- (over-) estimation of sensor sample distance.

Finally, potential rotations of the magnetization away from  $z$  in the vicinity of the edge due to, e.g. the Dzyaloshinskii-Moriya interaction [203] also lead to a modified magnetic stray field. However, as shown in [17], these modifications exist but are smaller than all the already mentioned uncertainties and can, hence, be neglected.

### A.3.3. Influence of DMI on a domain wall

Dzyaloshinskii-Moriya interaction (DMI) is an antisymmetric, anisotropic exchange interaction of the form  $(\mathbf{D} \cdot (\hat{\mathbf{S}}_i \times \hat{\mathbf{S}}_j))$ , where  $D$  is the micromagnetic DMI constant. DMI favors canting of spins and converts a Bloch wall into a Néel wall depending on the DMI strength. A schematic of a Bloch and Néel wall is shown in Fig. A.11.

The magnetic stray field of a Bloch wall is identical to the field at the sample edge Eq. (A.11)) but scaled by a factor of two. Bloch walls form in magnetic devices without DMI. The stray field of a Néel wall consists of the sum of the contribution of a Bloch wall Eq. (A.11)) and a term

$$\begin{aligned}\tilde{B}_x(x) &\approx \frac{1}{2}\mu_0\sigma_z\Delta_{\text{DW}}\frac{x^2 - z_{\text{NV}}^2}{(x^2 + z_{\text{NV}}^2)^2} \\ \tilde{B}_z(x) &\approx \mu_0\sigma_z\Delta_{\text{DW}}\frac{xz_{\text{NV}}}{(x^2 + z_{\text{NV}}^2)^2},\end{aligned}\tag{A.13}$$

where  $\Delta_{\text{DW}}$  is the domain wall width. The field projected onto the NV center is then

$$\mathbf{B}_{\text{NV}}(x) = \mathbf{e}_{\text{NV}} \cdot \left( \mathbf{B}(x) + \cos(\Psi) \tilde{\mathbf{B}}(x) \right),\tag{A.14}$$

where  $\Psi$  takes values in the range of  $[0, \pi]$  and depends on the DMI strength [36]. When we tune the DMI strength of  $\text{CrI}_3$  by applying an electric field across the flake, the transition from a Bloch to a Néel wall could be imaged. In the case of a Néel wall ( $\Psi = (0, \pi)$ ) the peak stray field intensity is 0.72 mT for reasonable parameters<sup>2</sup>. The peak field of a Bloch wall is 0.83 mT. The difference therefore is 0.11 mT ( $\approx 3$  MHz Zeeman shift), which should be easily detectable with an NV center.

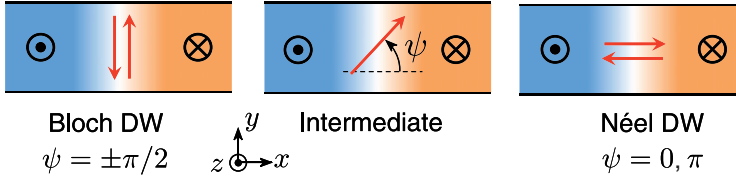


**Figure A.11.: Schematic a Bloch and Néel wall.** Top view of the domain wall structure in an out-of-plane magnetized film. The red arrows indicate the magnetization for a Bloch (left panel) and Néel wall (right panel). An intermediate case is characterized by the angle  $\Psi$ . The figure is adapted with permission from [36], American Physical Society.

<sup>2</sup> $z_{\text{NV}} = 60$  nm,  $\theta_{\text{NV}} = 54.7$  deg,  $\phi_{\text{NV}} = 0$  deg,  $\sigma_z = 136$   $\mu\text{A}$  ( $\equiv 14.7$   $\mu\text{B}/\text{nm}^2$ ),  $\Delta_{\text{DW}} = 5$  nm

### A.3.4. Stray magnetic field of a 1D spin chain

In Sec. 4.4 we gave a value for the magnetization of a 1D spin chain as illustrated in Fig. A.12. We retrieved this value in a similar fashion as for the uniform 2D magnetization described in the previous section. We fitted the magnetic field  $B_{\text{NV}}$  along a line perpendicular to the sample edge to the corresponding stray field.

We derive the stray field of a 1D spin chain along the y-axis by integrating the magnetic field of a 1D spin density  $\sigma = (0, 0, \sigma_z)$  according to

$$\mathbf{B}(\mathbf{r}) = \frac{\mu_0}{4\pi} \int_{-\infty}^{\infty} \frac{3\mathbf{r}(\sigma\mathbf{r}) - \sigma r^2}{r^5} dy \quad (\text{A.15})$$

which yields

$$\begin{aligned} B_x(x, z) &= \frac{\mu_0}{\pi} \frac{\sigma_z x z}{(x^2 + z^2)^2} \\ B_y(x, z) &= 0 \\ B_z(x, z) &= \frac{\mu_0}{2\pi} \frac{2\sigma_z z^2 - \sigma_z(x^2 + z^2)}{(x^2 + z^2)^2} \end{aligned} \quad (\text{A.16})$$

The fitting function then reads

$$\mathbf{B}_{\text{NV}}(\mathbf{r}) = \mathbf{e}_{\text{NV}} \cdot \mathbf{B}(\mathbf{r}) \quad (\text{A.17})$$

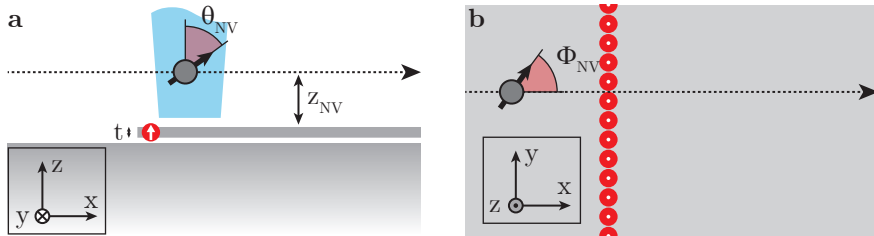


**Figure A.12.: Schematic of the setup for direct measurement of a 1D magnetization.** **a** Side view of the schematic. An NV center is scanned at a height  $z_{\text{NV}} \gg t$  over 1D spin chain along the y-axis. The NV center has an angle  $\theta_{\text{NV}}$  with respect to the z-axis. **b** Top view of the schematic. The NV center has an angle  $\phi_{\text{NV}}$  with respect to the x-axis.

### A.3.5. Magnetic field data

In this section, we present our magnetic field data for all magnetization maps of the figures indicated in the top left of the respective map.

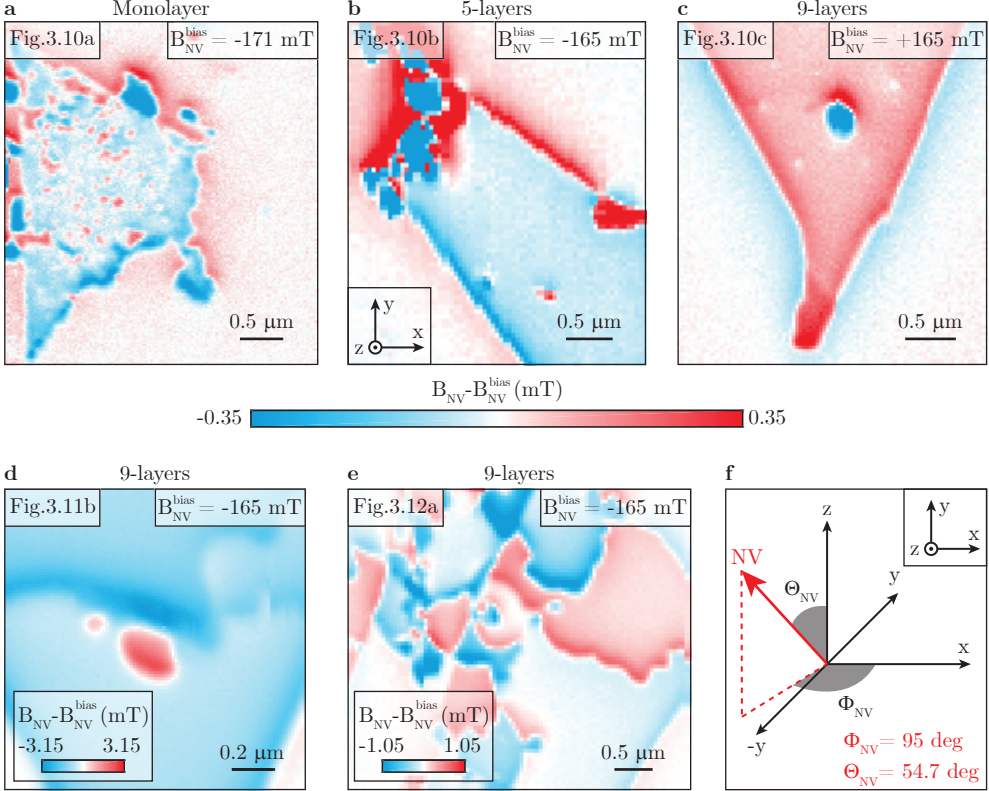


**Figure A.13.: Data set of measured  $B_{NV}$  maps.** **a-e** are maps of the stray magnetic field projected onto the NV-axis. The magnetization maps shown in the main text are based on the magnetic field maps presented here. The corresponding figures in the main text and background magnetic fields  $B_{NV}^{\text{bias}}$  are indicated in the figures themselves. The bias magnetic field perpendicular to the flake can be obtained from  $B_z = B_{NV}^{\text{bias}} \cdot \cos(\Theta_{NV})$  with  $\Theta_{NV} = 54.7^\circ$ . **f** Illustration of the NV axis on which the stray magnetic field is projected for **a-e**. The inset shows the coordination system for the field maps **a-e**. For all magnetization maps shown in the main text,  $\Phi_{NV} = 95^\circ$  and  $\Theta_{NV} = 54.7^\circ$  was used in the reverse propagation, since the same NV center was used in all experiments.

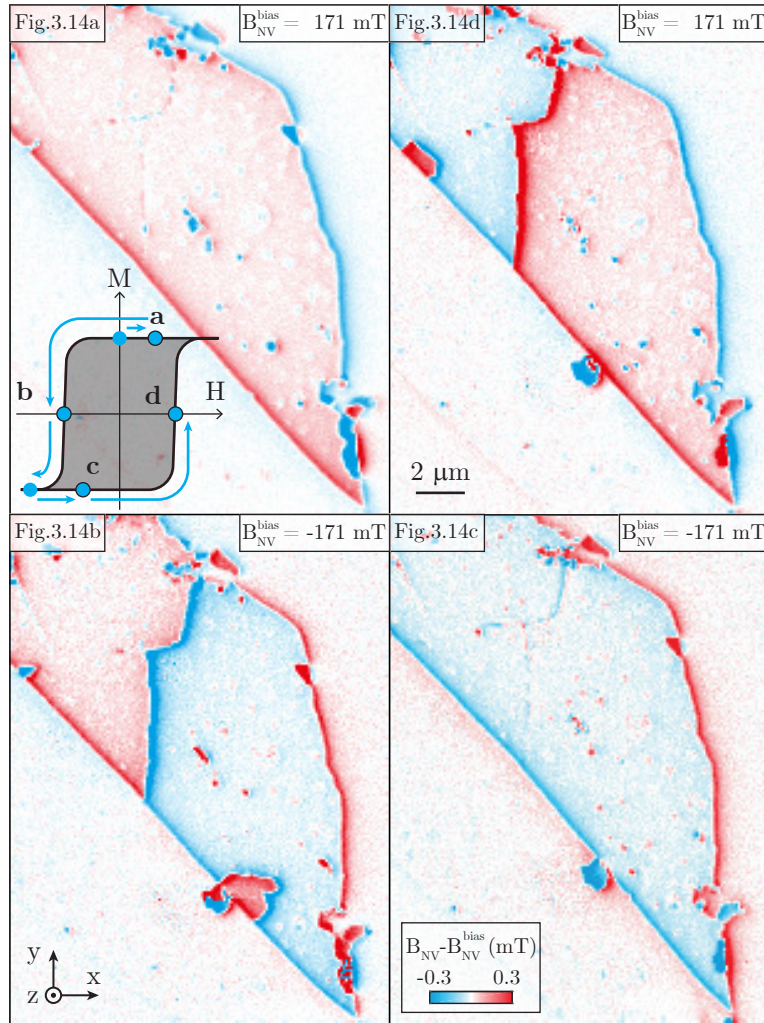


**Figure A.14.: Data set of measured  $B_{NV}$  maps.** Stray field maps of the magnetization as shown in the indicated figures. The scale bar, colorbar and coordinate axis applies to all panels. The inset indicates the applied field along the hysteresis curve for the respective figure.

### A.3.6. Raman spectra

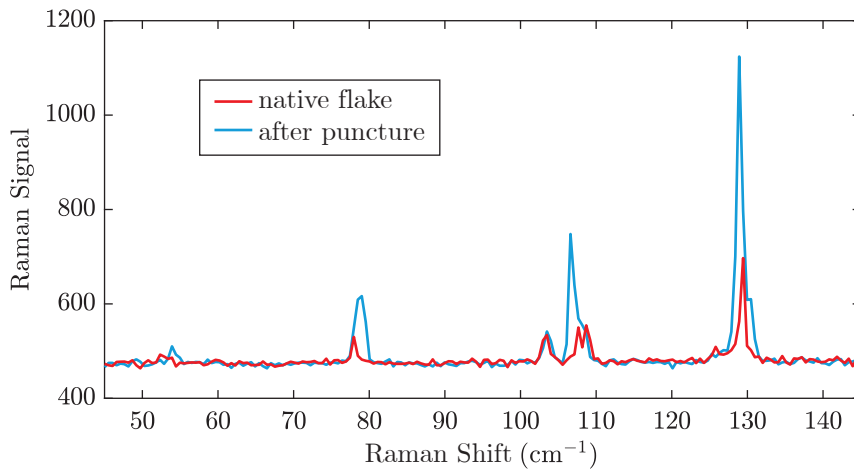


**Figure A.15.: Raman spectra at 6 K.** The Raman spectra of the native flake (red) and after puncture (blue) shows distinct differences for every strong Raman line. This is a clear evidence for the structural change between the two flakes which most likely led to a change in magnetic order.

## A.4. Current Imaging in Graphene

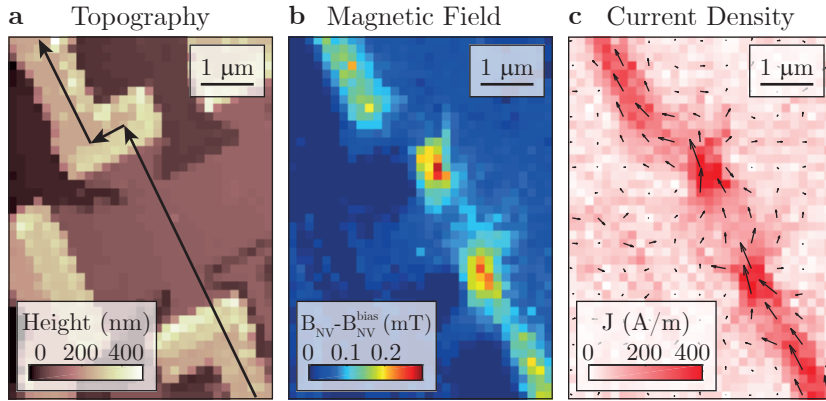


**Figure A.16.: Current imaging in a graphene Hall-bar.** **a** In-situ AFM data of the graphene Hall-bar. The silicon substrate is the darkest color. On top is the h-BN encapsulated graphene Hall-bar, visible in brown. The gold contacts are whitish. The current flow is indicated by a black arrow. We applied a current of approximately  $750 \mu\text{A}$  from the bottom right to the top left contact. **b** Magnetic stray field map. The measurement was performed in a background field of  $B_z = 131 \text{ mT}$ . **c** Reverse propagated current density  $J$  of the measured field (**b**).

## A.5. Code snippets

This section provides listings of useful functions discussed in this thesis. The code was written in MATLAB and tested with MATLAB 2018A.

### A.5.1. Calculation of $k$ values

```

1  function [kx, ky, k] = kvalues(nbX, nbY, dpx, dpy, FFTPaddingFactor)
2  % Find the wavenumber coordinates
3
4  % Input Parameters
5  %   nbX (scalar): dimension of grid in x direction
6  %   nbY (scalar): dimension of grid in y direction
7  %   dpx (in m): real space pixel spacing in x direction
8  %   dpy (in m): real space pixel spacing in y direction
9  %   FFTPaddingFactor (scalar): padding factor of FFT
10
11 % Output Parameters
12 %   kx (meshgrid): k vector in x direction
13 %   ky (meshgrid): k vector in y direction
14 %   k  (meshgrid): k vector
15
16   nbKx = nbX*FFTPaddingFactor;
17   nbKy = nbY*FFTPaddingFactor;
18   dkx = 2*pi/(dpx*nbKx);
19   dky = 2*pi/(dpy*nbKy);
20
21   if mod(nbX,2) == 0
22       % even
23       % DC component is not center pixel
24       kx_array = -dkx*(nbKx/2) : dkx : dkx*(nbKx/2-1);
25   else
26       % odd
27       % DC component is center pixel
28       kx_array = -dkx*(nbKx/2-0.5) : dkx : dkx*(nbKx/2-0.5);
29   end
30   if mod(nbY,2) == 0
31       % even
32       % DC component is not center pixel
33       ky_array = -dky*(nbKy/2) : dky : dky*(nbKy/2-1);
34   else
35       % odd
36       % DC component is center pixel
37       ky_array = -dky*(nbKy/2-0.5) : dky : dky*(nbKy/2-0.5);
38   end
39
40   % A tiny 'epsilon' is added to
41   % each freq. variable so as to avoid division by zero warning.
42   eps = 1e-20;
43   [kx,ky] = meshgrid(kx_array+eps,ky_array+eps);
44
45   k = sqrt(kx.^2 + ky.^2);
46 end

```



### A.5.2. $B_x$ , $B_y$ and $B_z$ from $B_{NV}$

```

1 function [Bx, By, Bz] = BxByBzFromBNV(...
2     dpx, dpy, BNV, thetaNV, phiNV, FFTPaddingFactor)
3 % Retrieves Bx, By, Bz from a planar map of BNV with NV axis ...
4     (thetaNV, phiNV)
5 % FFTPaddingFactor improves the FFT.
6
7 % Input Parameters
8 % dpx (in m): real space pixel spacing in x direction
9 % dpy (in m): real space pixel spacing in y direction
10 % BNV (in Tesla): magnetic field matrix along NV axis
11 % thetaNV (in degree): polar angle from z-axis to NV axis
12 % phiNV (in degree): is azimuthal angle from x-axis to NV axis
13 % FFTPaddingFactor (scalar): padding factor of FFT
14
15 % Output Parameters
16 % Bx (in Tesla): x component of BNV
17 % By (in Tesla): y component of BNV
18 % Bz (in Tesla): z component of BNV
19
20 %%%%%%%%%%%%%%%%%%%%%%%%%%%%%%%%%%%%%%%%%%%%%%%%%%%%%%%%%%%%%%%%%%%%%%%%%
21 % SETUP K-VECTOR
22 %%%%%%%%%%%%%%%%%%%%%%%%%%%%%%%%%%%%%%%%%%%%%%%%%%%%%%%%%%%%%%%%%%%%%%%%%
23 [nbY,nbX] = size(BNV);
24 nbKx = nbX*FFTPaddingFactor;
25 nbKy = nbY*FFTPaddingFactor;
26 [kx, ky, k] = kvalues(nbX, nbY, dpx, dpy, FFTPaddingFactor);
27
28 %%%%%%%%%%%%%%%%%%%%%%%%%%%%%%%%%%%%%%%%%%%%%%%%%%%%%%%%%%%%%%%%%%%%%%%%%
29 % TRANSFORMATION MATRICES
30 %%%%%%%%%%%%%%%%%%%%%%%%%%%%%%%%%%%%%%%%%%%%%%%%%%%%%%%%%%%%%%%%%%%%%%%%%
31
32 nx = sind(thetaNV)*cosd(phiNV);
33 ny = sind(thetaNV)*sind(phiNV);
34 nz = cosd(thetaNV);
35
36 T_BNV2Bx = 1./(nx + ny*ky./kx + 1i*nz*k./kx);
37 T_BNV2By = 1./(nx*kx./ky + ny + 1i*nz*k./ky);
38 T_BNV2Bz = 1./(-1i*nx*kx./k - 1i*ny*ky./k + nz);
39
40 %%%%%%%%%%%%%%%%%%%%%%%%%%%%%%%%%%%%%%%%%%%%%%%%%%%%%%%%%%%%%%%%%%%%%%%%%
41 % CALCULATE MAGNETIC FIELD
42 %%%%%%%%%%%%%%%%%%%%%%%%%%%%%%%%%%%%%%%%%%%%%%%%%%%%%%%%%%%%%%%%%%%%%%%%%
43
44 bnv = fftshift(fft2(BNV, nbKy, nbKx));
45 % get rid of DC component
46 bnv(k<eps) = 0;
47
48 bx = bnv.*T_BNV2Bx;
49 BX = real(ifft2( ifftshift (bx)));
50 Bx = BX(1:nbY , 1:nbX);
51
52 by = bnv.*T_BNV2By;
53 BY = real(ifft2( ifftshift (by)));
54 By = BY(1:nbY , 1:nbX);

```

```
55
56     bz = bnv.*T_BNV2Bz;
57     BZ = real(ifft2( ifftshift (bz)));
58     Bz = BZ(1:nbY , 1:nbX);
59 end
```

[illegible]

```
54      % CALCULATE MAGNETIZATION
55      %%%%%%%%%%%%%%%%%%%%%%%%%%%%%%%%%%%%%%%%%%%%%%%%%%%%%%%%%%%%%%%%%%%%%%%%%
56
57      bnv = fftshift(fft2(BNV, nbKy, nbKx));
58      % get rid of DC component
59      bnv(k<eps) = 0;
60
61      mz = bnv.*Trans.BtoM;
62      Mext = real(ifft2( ifftshift (mz)));
63      Mz = Mext(1:nbY , 1:nbX);
64  end
```

[illegible]

```
55     bnv = fftshift(fft2(BNV, nbKy, nbKx));
56     % get rid of DC component
57     bnv(k<eps) = 0;
58
59     jx = W.*T.BtoJx.*bnv;
60     jy = W.*T.BtoJy.*bnv;
61
62     Jxext = real(ifft2( ifftshift (jx)));
63     Jx = Jxext(1:nbY , 1:nbX);
64     Jyext = real(ifft2( ifftshift (jy)));
65     Jy = Jyext(1:nbY , 1:nbX);
66
67     J = sqrt(Jx.^2+Jy.^2);
68
69 end
```

## B. Bibliography

- [1] V. M. Acosta, E. Bauch, M. P. Ledbetter, A. Waxman, L.-S. Bouchard, and D. Budker, “Temperature Dependence of the Nitrogen-Vacancy Magnetic Resonance in Diamond,” *Physical Review Letters*, vol. 104, no. 7, p. 070801, Feb. 2010. [Online]. Available: <https://link.aps.org/doi/10.1103/PhysRevLett.104.070801>
- [2] G. Kucsko, P. C. Maurer, N. Y. Yao, M. Kubo, H. J. Noh, P. K. Lo, H. Park, and M. D. Lukin, “Nanometre-scale thermometry in a living cell,” *Nature*, vol. 500, p. 54, Jul. 2013. [Online]. Available: <https://doi.org/10.1038/nature12373>
- [3] D. M. Toyli, D. J. Christle, A. Alkauskas, B. B. Buckley, C. G. Van de Walle, and D. D. Awschalom, “Measurement and Control of Single Nitrogen-Vacancy Center Spins above 600 K,” *Physical Review X*, vol. 2, no. 3, p. 031001, Jul. 2012. [Online]. Available: <https://link.aps.org/doi/10.1103/PhysRevX.2.031001>
- [4] P. Neumann, I. Jakobi, F. Dolde, C. Burk, R. Reuter, G. Waldherr, J. Honert, T. Wolf, A. Brunner, J. H. Shim, D. Suter, H. Sumiya, J. Isoya, and J. Wrachtrup, “High-Precision Nanoscale Temperature Sensing Using Single Defects in Diamond,” *Nano Letters*, vol. 13, no. 6, pp. 2738–2742, Jun. 2013. [Online]. Available: <https://doi.org/10.1021/nl401216y>
- [5] F. Dolde, H. Fedder, M. W. Doherty, T. Nöbauer, F. Rempp, G. Balasubramanian, T. Wolf, F. Reinhard, L. C. L. Hollenberg, F. Jelezko, and J. Wrachtrup, “Electric-field sensing using single diamond spins,” *Nature Physics*, vol. 7, p. 459, Apr. 2011. [Online]. Available: <https://doi.org/10.1038/nphys1969>
- [6] M. W. Doherty, V. V. Struzhkin, D. A. Simpson, L. P. McGuinness, Y. Meng, A. Stacey, T. J. Karle, R. J. Hemley, N. B. Manson, L. C. L. Hollenberg, and S. Prawer, “Electronic Properties and Metrology Applications of the Diamond NV<sup>−</sup> Center under Pressure,” *Physical Review Letters*, vol. 112, no. 4, p. 047601, Jan. 2014. [Online]. Available: <https://link.aps.org/doi/10.1103/PhysRevLett.112.047601>
- [7] W. C. P. G. Davies, M. F. Hamer, “Optical studies of the 1.945 eV vibronic band in diamond,” *Proceedings of the Royal Society of London A: Mathematical, Physical and Engineering Sciences*, vol. 348, no. 285, 1976.
- [8] G. Balasubramanian, I. Y. Chan, R. Kolesov, M. Al-Hmoud, J. Tisler, C. Shin, C. Kim, A. Wojcik, P. R. Hemmer, A. Krueger, T. Hanke, A. Leitenstorfer, R. Bratschkitsch, F. Jelezko, and J. Wrachtrup, “Nanoscale imaging magnetometry with diamond spins under ambient conditions,” *Nature*, vol. 455, p. 648, Oct. 2008. [Online]. Available: <https://doi.org/10.1038/nature07278>

- [9] C. L. Degen, “Scanning magnetic field microscope with a diamond single-spin sensor,” *Applied Physics Letters*, vol. 92, no. 24, p. 243111, Dec. 2008. [Online]. Available: <https://doi.org/10.1063/1.2943282>
- [10] J. R. Maze, P. L. Stanwix, J. S. Hodges, S. Hong, J. M. Taylor, P. Cappellaro, L. Jiang, M. V. G. Dutt, E. Togan, A. S. Zibrov, A. Yacoby, R. L. Walsworth, and M. D. Lukin, “Nanoscale magnetic sensing with an individual electronic spin in diamond,” *Nature*, vol. 455, p. 644, Oct. 2008. [Online]. Available: <https://doi.org/10.1038/nature07279>
- [11] J. M. Taylor, P. Cappellaro, L. Childress, L. Jiang, D. Budker, P. R. Hemmer, A. Yacoby, R. Walsworth, and M. D. Lukin, “High-sensitivity diamond magnetometer with nanoscale resolution,” *Nature Physics*, vol. 4, p. 810, Sep. 2008. [Online]. Available: <https://doi.org/10.1038/nphys1075>
- [12] R. Schirhagl, K. Chang, M. Loretz, and C. L. Degen, “Nitrogen-Vacancy Centers in Diamond: Nanoscale Sensors for Physics and Biology,” *Annual Review of Physical Chemistry*, vol. 65, no. 1, pp. 83–105, Jan. 2014. [Online]. Available: <https://doi.org/10.1146/annurev-physchem-040513-103659>
- [13] L. Rondin, J.-P. Tetienne, T. Hingant, J.-F. Roch, P. Maletinsky, and V. Jacques, “Magnetometry with Nitrogen-Vacancy defects in diamond,” *Reports on Progress in Physics*, vol. 77, no. 5, p. 056503, 2014. [Online]. Available: <http://stacks.iop.org/0034-4885/77/i=5/a=056503>
- [14] N. Aslam, M. Pfender, R. Stöhr, P. Neumann, M. Scheffler, H. Sumiya, H. Abe, S. Onoda, T. Ohshima, J. Isoya, and J. Wrachtrup, “Single spin optically detected magnetic resonance with 60-90 GHz (E-band) microwave resonators,” *Review of Scientific Instruments*, vol. 86, no. 6, p. 064704, Jan. 2015. [Online]. Available: <https://doi.org/10.1063/1.4922664>
- [15] V. Stepanov, F. H. Cho, C. Abeywardana, and S. Takahashi, “High-frequency and high-field optically detected magnetic resonance of Nitrogen-Vacancy centers in diamond,” *Applied Physics Letters*, vol. 106, no. 6, p. 063111, Jan. 2015. [Online]. Available: <https://doi.org/10.1063/1.4908528>
- [16] P. Maletinsky, S. Hong, M. S. Grinolds, B. Hausmann, M. D. Lukin, R. L. Walsworth, M. Loncar, and A. Yacoby, “A robust scanning diamond sensor for nanoscale imaging with single nitrogen-vacancy centres,” *Nature Nanotechnology*, vol. 7, p. 320, Apr. 2012. [Online]. Available: <https://doi.org/10.1038/nnano.2012.50>
- [17] J.-P. Tetienne, T. Hingant, L. J. Martínez, S. Rohart, A. Thiaville, L. H. Diez, K. Garcia, J.-P. Adam, J.-V. Kim, J.-F. Roch, I. M. Miron, G. Gaudin, L. Vila, B. Ocker, D. Ravelosona, and V. Jacques, “The nature of domain walls in ultrathin ferromagnets revealed by scanning nanomagnetometry,” *Nature Communications*, vol. 6, p. 6733, Apr. 2015. [Online]. Available: <https://doi.org/10.1038/ncomms7733>



- 
- [18] Y. Dovzhenko, F. Casola, S. Schlotter, T. X. Zhou, F. Büttner, R. L. Walsworth, G. S. D. Beach, and A. Yacoby, “Magnetostatic twists in room-temperature skyrmions explored by Nitrogen-Vacancy center spin texture reconstruction,” *Nature Communications*, vol. 9, no. 1, p. 2712, Jul. 2018. [Online]. Available: <https://doi.org/10.1038/s41467-018-05158-9>
- [19] I. Gross, W. Akhtar, V. Garcia, L. J. Martínez, S. Chouaieb, K. Garcia, C. Carrétéro, A. Barthélémy, P. Appel, P. Maletinsky, J.-V. Kim, J. Y. Chauleau, N. Jaouen, M. Viret, M. Bibes, S. Fusil, and V. Jacques, “Real-space imaging of non-collinear antiferromagnetic order with a single-spin magnetometer,” *Nature*, vol. 549, p. 252, Sep. 2017. [Online]. Available: <https://doi.org/10.1038/nature23656>
- [20] T. van der Sar, F. Casola, R. Walsworth, and A. Yacoby, “Nanometre-scale probing of spin waves using single electron spins,” *Nature Communications*, vol. 6, p. 7886, Aug. 2015. [Online]. Available: <https://doi.org/10.1038/ncomms8886>
- [21] C. Du, T. van der Sar, T. X. Zhou, P. Upadhyaya, F. Casola, H. Zhang, M. C. Onbasli, C. A. Ross, R. L. Walsworth, Y. Tserkovnyak, and A. Yacoby, “Control and local measurement of the spin chemical potential in a magnetic insulator,” *Science*, vol. 357, no. 6347, p. 195, Jul. 2017. [Online]. Available: <http://science.sciencemag.org/content/357/6347/195.abstract>
- [22] S. Kolkowitz, A. Safra, A. A. High, R. C. Devlin, S. Choi, Q. P. Unterreithmeier, D. Patterson, A. S. Zibrov, V. E. Manucharyan, H. Park, and M. D. Lukin, “Probing johnson noise and ballistic transport in normal metals with a single-spin qubit,” *Science*, vol. 347, no. 6226, p. 1129, Mar. 2015. [Online]. Available: <http://science.sciencemag.org/content/347/6226/1129.abstract>
- [23] K. Agarwal, R. Schmidt, B. Halperin, V. Oganessian, G. Zaránd, M. D. Lukin, and E. Demler, “Magnetic noise spectroscopy as a probe of local electronic correlations in two-dimensional systems,” *Physical Review B*, vol. 95, no. 15, p. 155107, Apr. 2017. [Online]. Available: <https://link.aps.org/doi/10.1103/PhysRevB.95.155107>
- [24] J.-P. Tetienne, N. Dotschuk, D. A. Broadway, A. Stacey, D. A. Simpson, and L. C. L. Hollenberg, “Quantum imaging of current flow in graphene,” *Science Advances*, vol. 3, no. 4, 2017. [Online]. Available: <http://advances.sciencemag.org/content/3/4/e1602429>
- [25] K. Chang, A. Eichler, J. Rhensius, L. Lorenzelli, and C. L. Degen, “Nanoscale Imaging of Current Density with a Single-Spin Magnetometer,” *Nano Letters*, vol. 17, no. 4, pp. 2367–2373, Apr. 2017. [Online]. Available: <https://doi.org/10.1021/acs.nanolett.6b05304>
- [26] A. Nowodziniski, M. Chipaux, L. Toraille, V. Jacques, J.-F. Roch, and T. Debuisschert, “Nitrogen-Vacancy centers in diamond for current imaging at the redistributive layer level of Integrated Circuits,” *Microelectronics Reliability*, vol. 55, no. 9, pp. 1549–1553, Aug. 2015. [Online]. Available: <http://www.sciencedirect.com/science/article/pii/S0026271415001614>

- [27] Y. Martin and H. K. Wickramasinghe, “Magnetic imaging by “force microscopy” with 1000 Å resolution,” *Applied Physics Letters*, vol. 50, no. 20, pp. 1455–1457, Dec. 1987. [Online]. Available: <https://doi.org/10.1063/1.97800>
- [28] D. Rugar, R. Budakian, H. J. Mamin, and B. W. Chui, “Single spin detection by magnetic resonance force microscopy,” *Nature*, vol. 430, p. 329, Jul. 2004. [Online]. Available: <https://doi.org/10.1038/nature02658>
- [29] D. Vasyukov, Y. Anahory, L. Embon, D. Halbertal, J. Cuppens, L. Neeman, A. Finkler, Y. Segev, Y. Myasoedov, M. L. Rappaport, M. E. Huber, and E. Zeldov, “A scanning superconducting quantum interference device with single electron spin sensitivity,” *Nature Nanotechnology*, vol. 8, p. 639, Sep. 2013. [Online]. Available: <https://doi.org/10.1038/nnano.2013.169>
- [30] J. R. Kirtley, “Fundamental studies of superconductors using scanning magnetic imaging,” *Reports on Progress in Physics*, vol. 73, no. 12, p. 126501, 2010. [Online]. Available: <http://stacks.iop.org/0034-4885/73/i=12/a=126501>
- [31] B. M. Chernobrod and G. P. Berman, “Spin microscope based on optically detected magnetic resonance,” *Journal of Applied Physics*, vol. 97, no. 1, p. 014903, Dec. 2005. [Online]. Available: <https://doi.org/10.1063/1.1829373>
- [32] M. S. Grinolds, S. Hong, P. Maletinsky, L. Luan, M. D. Lukin, R. L. Walsworth, and A. Yacoby, “Nanoscale magnetic imaging of a single electron spin under ambient conditions,” *Nature Physics*, vol. 9, p. 215, Feb. 2013. [Online]. Available: <https://doi.org/10.1038/nphys2543>
- [33] J.-P. Tetienne, T. Hingant, J.-V. Kim, L. H. Diez, J.-P. Adam, K. Garcia, J.-F. Roch, S. Rohart, A. Thiaville, D. Ravelosona, and V. Jacques, “Nanoscale imaging and control of domain-wall hopping with a Nitrogen-Vacancy center microscope,” *Science*, vol. 344, no. 6190, p. 1366, Jun. 2014. [Online]. Available: <http://science.sciencemag.org/content/344/6190/1366.abstract>
- [34] P. Appel, M. Ganzhorn, E. Neu, and P. Maletinsky, “Nanoscale microwave imaging with a single electron spin in diamond,” *New Journal of Physics*, vol. 17, no. 11, p. 112001, 2015. [Online]. Available: <http://stacks.iop.org/1367-2630/17/i=11/a=112001>
- [35] P. Appel, B. J. Shields, T. Kosub, N. Hedrich, R. Hübner, J. Fassbender, D. Makarov, and P. Maletinsky, “Nanomagnetism of magnetoelectric granular thin-film antiferromagnets,” *Nano Letters*, Jan. 2019. [Online]. Available: <https://doi.org/10.1021/acs.nanolett.8b04681>
- [36] I. Gross, L. J. Martínez, J.-P. Tetienne, T. Hingant, J.-F. Roch, K. Garcia, R. Soucaille, J. P. Adam, J.-V. Kim, S. Rohart, A. Thiaville, J. Torrejon, M. Hayashi, and V. Jacques, “Direct measurement of interfacial Dzyaloshinskii-Moriya interaction in X|CoFeB|MgO heterostructures with a scanning NV magnetometer ( $X = \text{Ta, TaN, and W}$ ),” *Physical Review B*, vol. 94, no. 6, p. 064413, Aug. 2016. [Online]. Available: <https://link.aps.org/doi/10.1103/PhysRevB.94.064413>

- 
- [37] P. Appel, E. Neu, M. Ganzhorn, A. Barfuss, M. Batzer, M. Gratz, A. Tschöpe, and P. Maletinsky, “Fabrication of all diamond scanning probes for nanoscale magnetometry,” *Review of Scientific Instruments*, vol. 87, no. 6, p. 063703, Dec. 2016. [Online]. Available: <https://doi.org/10.1063/1.4952953>
- [38] A. Barfuss, “Hybrid spin-nanomechanics with single spins in diamond mechanical oscillators,” PhD thesis, University of Basel, Faculty of Science, 2017. [Online]. Available: [http://edoc.unibas.ch/diss/DissB\\_12469](http://edoc.unibas.ch/diss/DissB_12469)
- [39] M. W. Doherty, N. B. Manson, P. Delaney, F. Jelezko, J. Wrachtrup, and L. C. L. Hollenberg, “The Nitrogen-Vacancy colour centre in diamond,” *Physics Reports*, vol. 528, no. 1, pp. 1–45, Jul. 2013. [Online]. Available: <http://www.sciencedirect.com/science/article/pii/S0370157313000562>
- [40] L. Robledo, H. Bernien, T. v. d. Sar, and R. Hanson, “Spin dynamics in the optical cycle of single Nitrogen-Vacancy centres in diamond,” *New Journal of Physics*, vol. 13, no. 2, p. 025013, Feb. 2011. [Online]. Available: <http://dx.doi.org/10.1088/1367-2630/13/2/025013>
- [41] N. B. Manson, J. P. Harrison, and M. J. Sellars, “Nitrogen-vacancy center in diamond: Model of the electronic structure and associated dynamics,” *Physical Review B*, vol. 74, no. 10, p. 104303, Sep. 2006. [Online]. Available: <https://link.aps.org/doi/10.1103/PhysRevB.74.104303>
- [42] L. Robledo, H. Bernien, T. van der Sar, and R. Hanson, “Spin dynamics in the optical cycle of single Nitrogen-Vacancy centres in diamond,” *New Journal of Physics*, vol. 13, no. 2, p. 025013, 2011. [Online]. Available: <http://stacks.iop.org/1367-2630/13/i=2/a=025013>
- [43] M. L. Goldman, A. Sipahigil, M. W. Doherty, N. Y. Yao, S. D. Bennett, M. Markham, D. J. Twitchen, N. B. Manson, A. Kubanek, and M. D. Lukin, “Phonon-Induced Population Dynamics and Intersystem Crossing in Nitrogen-Vacancy Centers,” *Physical Review Letters*, vol. 114, no. 14, p. 145502, Apr. 2015. [Online]. Available: <https://link.aps.org/doi/10.1103/PhysRevLett.114.145502>
- [44] A. Dréau, M. Lesik, L. Rondin, P. Spinicelli, O. Arcizet, J.-F. Roch, and V. Jacques, “Avoiding power broadening in optically detected magnetic resonance of single NV defects for enhanced DC magnetic field sensitivity,” *Physical Review B*, vol. 84, no. 19, p. 195204, Nov. 2011. [Online]. Available: <https://link.aps.org/doi/10.1103/PhysRevB.84.195204>
- [45] B. J. M. Hausmann, M. Khan, Y. Zhang, T. M. Babinec, K. Martinick, M. McCutcheon, P. R. Hemmer, and M. Loncar, “Fabrication of diamond nanowires for quantum information processing applications,” *Diamond and Related Materials*, vol. 19, no. 5, pp. 621–629, May 2010. [Online]. Available: <http://www.sciencedirect.com/science/article/pii/S0925963510000312>
- [46] F. Casola, T. van der Sar, and A. Yacoby, “Probing condensed matter physics with magnetometry based on nitrogen-vacancy centres in diamond,”

- Nature Reviews Materials*, vol. 3, p. 17088, Jan. 2018. [Online]. Available: <https://doi.org/10.1038/natrevmats.2017.88>
- [47] C. L. Degen, F. Reinhard, and P. Cappellaro, “Quantum sensing,” *Review of Modern Physics*, vol. 89, no. 3, p. 035002, Jul. 2017. [Online]. Available: <https://link.aps.org/doi/10.1103/RevModPhys.89.035002>
- [48] J.-P. Tetienne, L. Rondin, P. Spinicelli, M. Chipaux, T. Debuisschert, J.-F. Roch, and V. Jacques, “Magnetic-field-dependent photodynamics of single NV defects in diamond: an application to qualitative all-optical magnetic imaging,” *New Journal of Physics*, vol. 14, no. 10, p. 103033, 2012. [Online]. Available: <http://stacks.iop.org/1367-2630/14/i=10/a=103033>
- [49] S. Steinert, F. Dolde, P. Neumann, A. Aird, B. Naydenov, G. Balasubramanian, F. Jelezko, and J. Wrachtrup, “High sensitivity magnetic imaging using an array of spins in diamond,” *Review of Scientific Instruments*, vol. 81, no. 4, p. 043705, Dec. 2010. [Online]. Available: <https://doi.org/10.1063/1.3385689>
- [50] R. S. Schoenfeld and W. Harneit, “Real Time Magnetic Field Sensing and Imaging Using a Single Spin in Diamond,” *Physical Review Letters*, vol. 106, no. 3, p. 030802, Jan. 2011. [Online]. Available: <https://link.aps.org/doi/10.1103/PhysRevLett.106.030802>
- [51] M. S. Grinolds, M. Warner, K. De Greve, Y. Dovzhenko, L. Thiel, R. L. Walsworth, S. Hong, P. Maletinsky, and A. Yacoby, “Subnanometre resolution in three-dimensional magnetic resonance imaging of individual dark spins,” *Nature Nanotechnology*, vol. 9, p. 279, Mar. 2014. [Online]. Available: <https://doi.org/10.1038/nnano.2014.30>
- [52] R. J. Blakely, *Potential Theory in Gravity and Magnetic Applications*. Cambridge: Cambridge University Press, 1995. [Online]. Available: <https://www.cambridge.org/core/books/potential-theory-in-gravity-and-magnetic-applications/348880F23008E16E663D6AD14A41D8DE>
- [53] E. A. Lima and B. P. Weiss, “Obtaining vector magnetic field maps from single-component measurements of geological samples,” *Journal of Geophysical Research*, vol. 114, no. B6, Dec. 2009. [Online]. Available: <https://doi.org/10.1029/2008JB006006>
- [54] S. Tan, Y. P. Ma, I. M. Thomas, and J. P. Wikswo, “Reconstruction of two-dimensional magnetization and susceptibility distributions from the magnetic field of soft magnetic materials,” *IEEE Transactions on Magnetics*, vol. 32, no. 1, pp. 230–234, 1996. [Online]. Available: <https://ieeexplore.ieee.org/document/477575>
- [55] L. Thiel, Z. Wang, M. A. Tschudin, D. Rohner, I. Gutiérrez-Lezama, N. Ubrig, M. Gibertini, E. Giannini, A. F. Morpurgo, and P. Maletinsky, “Probing magnetism in 2D materials at the nanoscale with single spin microscopy,” *arXiv e-prints, accepted in Science*, p. arXiv:1902.01406, Feb. 2019. [Online]. Available: <https://arxiv.org/abs/1902.01406>

- 
- [56] B. J. Roth, N. G. Sepulveda, and J. P. Wikswo, “Using a magnetometer to image a two-dimensional current distribution,” *Journal of Applied Physics*, vol. 65, no. 1, pp. 361–372, Dec. 1988. [Online]. Available: <https://doi.org/10.1063/1.342549>
- [57] A. I. B. E. John Clarke (Editor), *The SQUID Handbook: Applications of SQUIDS and SQUID Systems, Volume II*, G. Wiley-VCH, Weinheim, Ed. Wiley-VCH, Weinheim, Germany, 2006.
- [58] E. Schäfer-Nolte, F. Reinhard, M. Ternes, J. Wrachtrup, and K. Kern, “A diamond-based scanning probe spin sensor operating at low temperature in ultra-high vacuum,” *Review of Scientific Instruments*, vol. 85, no. 1, p. 013701, Jan. 2014. [Online]. Available: <https://doi.org/10.1063/1.4858835>
- [59] L. Thiel, D. Rohner, M. Ganzhorn, P. Appel, E. Neu, B. Müller, R. Kleiner, D. Kölle, and P. Maletinsky, “Quantitative nanoscale vortex imaging using a cryogenic quantum magnetometer,” *Nature Nanotechnology*, vol. 11, p. 677, May 2016. [Online]. Available: <https://doi.org/10.1038/nnano.2016.63>
- [60] M. Pelliccione, A. Jenkins, P. Ovartchaiyapong, C. Reetz, E. Emmanouilidou, N. Ni, and A. C. Bleszynski Jayich, “Scanned probe imaging of nanoscale magnetism at cryogenic temperatures with a single-spin quantum sensor,” *Nature Nanotechnology*, vol. 11, p. 700, May 2016. [Online]. Available: <https://doi.org/10.1038/nnano.2016.68>
- [61] D. Rohner, L. Thiel, B. Müller, M. Kasperczyk, R. Kleiner, D. Kölle, and P. Maletinsky, “Real-Space Probing of the Local Magnetic Response of Thin-Film Superconductors Using Single Spin Magnetometry,” *Sensors*, vol. 18, no. 11, 2018. [Online]. Available: <http://www.mdpi.com/1424-8220/18/11/3790>
- [62] O. M. Auslaender, L. Luan, E. W. J. Straver, J. E. Hoffman, N. C. Koshnick, E. Zeldov, D. A. Bonn, R. Liang, W. N. Hardy, and K. A. Moler, “Mechanics of individual isolated vortices in a cuprate superconductor,” *Nature Physics*, vol. 5, p. 35, Nov. 2008. [Online]. Available: <https://doi.org/10.1038/nphys1127>
- [63] A. Oral, S. J. Bending, and M. Henini, “Scanning Hall probe microscopy of superconductors and magnetic materials,” *Journal of Vacuum Science & Technology B: Microelectronics and Nanometer Structures Processing, Measurement, and Phenomena*, vol. 14, no. 2, pp. 1202–1205, Jan. 1996. [Online]. Available: <https://avs.scitation.org/doi/abs/10.1116/1.588514>
- [64] Ø. Fischer, M. Kugler, I. Maggio-Aprile, C. Berthod, and C. Renner, “Scanning tunneling spectroscopy of high-temperature superconductors,” *Review of Modern Physics*, vol. 79, no. 1, pp. 353–419, Mar. 2007. [Online]. Available: <https://link.aps.org/doi/10.1103/RevModPhys.79.353>
- [65] B. W. Gardner, J. C. Wynn, D. A. Bonn, R. Liang, W. N. Hardy, J. R. Kirtley, V. G. Kogan, and K. A. Moler, “Manipulation of single vortices in  $\text{YBa}_2\text{Cu}_3\text{O}_{6.354}$  with a locally applied magnetic field,” *Applied*

- Physics Letters*, vol. 80, no. 6, pp. 1010–1012, Jan. 2002. [Online]. Available: <https://doi.org/10.1063/1.1445468>
- [66] Y. Schlussel, T. Lenz, D. Rohner, Y. Bar-Haim, L. Bougas, D. Groswasser, M. Kieschnick, E. Rozenberg, L. Thiel, A. Waxman, J. Meijer, P. Maletinsky, D. Budker, and R. Folman, “Wide-Field Imaging of Superconductor Vortices with Electron Spins in Diamond,” *Physical Review Applied*, vol. 10, no. 3, p. 034032, Sep. 2018. [Online]. Available: <https://link.aps.org/doi/10.1103/PhysRevApplied.10.034032>
- [67] G. Blatter, M. V. Feigel’man, V. B. Geshkenbein, A. I. Larkin, and V. M. Vinokur, “Vortices in high-temperature superconductors,” *Review of Modern Physics*, vol. 66, no. 4, pp. 1125–1388, Oct. 1994. [Online]. Available: <https://link.aps.org/doi/10.1103/RevModPhys.66.1125>
- [68] G. Carneiro and E. H. Brandt, “Vortex lines in films: Fields and interactions,” *Physical Review B*, vol. 61, no. 9, pp. 6370–6376, Mar. 2000. [Online]. Available: <https://link.aps.org/doi/10.1103/PhysRevB.61.6370>
- [69] H. K. Onnes, “On the sudden change in the rate at which the resistance of mercury disappears,” *Comm. Phys. Lab. Univ. Leiden*, 1911.
- [70] W. Meissner and R. Ochsenfeld, “Ein neuer Effekt bei Eintritt der Supraleitfähigkeit,” *Naturwissenschaften*, vol. 21, pp. 787–788, 1933.
- [71] J. Bardeen, L. N. Cooper, and J. R. Schrieffer, “Microscopic theory of superconductivity,” *Physical Review*, vol. 106, no. 1, pp. 162–164, Apr. 1957. [Online]. Available: <https://link.aps.org/doi/10.1103/PhysRev.106.162>
- [72] V. V. Moshchalkov and J. Fritzsche, *Nanostructured Superconductors*. World Scientific, Dec. 2011. [Online]. Available: <https://doi.org/10.1142/8132>
- [73] F. London, H. London, and L. F. Alexander, “The electromagnetic equations of the supraconductor,” *Proceedings of the Royal Society of London. Series A - Mathematical and Physical Sciences*, vol. 149, no. 866, pp. 71–88, Dec. 1935. [Online]. Available: <https://doi.org/10.1098/rspa.1935.0048>
- [74] V. L. Ginzburg and L. D. Landau, “On the Theory of superconductivity,” *Zhur-nal Eksperimentalnoi i Teoreticheskoi Fiziki*, vol. 20, pp. 1064–1082, 1950.
- [75] M. Tinkham, *Introduction to Superconductivity*. Dover Publications, INC., 2004.
- [76] J. G. Bednorz and K. A. Müller, “Possible high  $T_c$  superconductivity in the Ba-La-Cu-O system,” *Zeitschrift für Physik B Condensed Matter*, vol. B64, pp. 189–193, 1986.
- [77] W. L. McMillan, “Transition Temperature of Strong-Coupled Superconductors,” *Physical Review*, vol. 167, no. 2, pp. 331–344, Mar. 1968. [Online]. Available: <https://link.aps.org/doi/10.1103/PhysRev.167.331>

- 
- [78] M. K. Wu, J. R. Ashburn, C. J. Torng, P. H. Hor, R. L. Meng, L. Gao, Z. J. Huang, Y. Q. Wang, and C. W. Chu, "Superconductivity at 93 K in a new mixed-phase Y-Ba-Cu-O compound system at ambient pressure," *Physical Review Letters*, vol. 58, no. 9, pp. 908–910, Mar. 1987. [Online]. Available: <https://link.aps.org/doi/10.1103/PhysRevLett.58.908>
  - [79] H. U. o. T. Laboratory of Advanced Energy Systems. (2008) High-temperature superconductivity. [Online; 2019.01.04]. [Online]. Available: <http://tfy.tkk.fi/aes/AES/projects/prlaser/supercond.htm>
  - [80] H. W. Werner Martienssen, *Springer Handbook of Condensed Matter and Materials Data*, H. Springer, Berlin, Ed. Springer, Berlin, Heidelberg, 2005. [Online]. Available: <https://link.springer.com/referencework/10.1007%2F3-540-30437-1#about>
  - [81] R. Werner, C. Raisch, A. Ruosi, B. A. Davidson, P. Nagel, M. Merz, S. Schuppler, M. Glaser, J. Fujii, T. Chassé, R. Kleiner, and D. Kölle, "YBa<sub>2</sub>Cu<sub>3</sub>O<sub>7</sub>/La<sub>0.7</sub>Ca<sub>0.3</sub>MnO<sub>3</sub> bilayers: Interface coupling and electric transport properties," *Physical Review B*, vol. 82, no. 22, p. 224509, Dec. 2010. [Online]. Available: <https://link.aps.org/doi/10.1103/PhysRevB.82.224509>
  - [82] S. Scharinger, M. Turad, A. Stöhr, V. Leca, E. Goldobin, R. G. Mints, D. Kölle, and R. Kleiner, "Magnetic field dependence of the critical current in YBa<sub>2</sub>Cu<sub>3</sub>O<sub>7-δ</sub>/Au/Nb ramp-zigzag Josephson junctions," *Physical Review B*, vol. 86, no. 14, p. 144531, Oct. 2012. [Online]. Available: <https://link.aps.org/doi/10.1103/PhysRevB.86.144531>
  - [83] J. W. Guikema, H. Bluhm, D. A. Bonn, R. Liang, W. N. Hardy, and K. A. Moler, "Two-dimensional vortex behavior in highly underdoped YBa<sub>2</sub>Cu<sub>3</sub>O<sub>6+x</sub> observed by scanning Hall probe microscopy," *Physical Review B*, vol. 77, no. 10, p. 104515, Mar. 2008. [Online]. Available: <https://link.aps.org/doi/10.1103/PhysRevB.77.104515>
  - [84] G. E. Volovik, "Monopoles and fractional vortices in chiral superconductors," *Proc Natl Acad Sci USA*, vol. 97, no. 6, p. 2431, Mar. 2000. [Online]. Available: <http://www.pnas.org/content/97/6/2431.abstract>
  - [85] C. C. Tsuei, J. R. Kirtley, C. C. Chi, L. S. Yu-Jahnes, A. Gupta, T. Shaw, J. Z. Sun, and M. B. Ketchen, "Pairing Symmetry and Flux Quantization in a Tricrystal Superconducting Ring of YBa<sub>2</sub>Cu<sub>3</sub>O<sub>7-δ</sub>," *Physical Review Letters*, vol. 73, no. 4, pp. 593–596, Jul. 1994. [Online]. Available: <https://link.aps.org/doi/10.1103/PhysRevLett.73.593>
  - [86] J. R. Kirtley, C. C. Tsuei, H. Raffy, Z. Z. Li, A. Gupta, J. Z. Sun, and S. Megtert, "Half-integer flux quantum effect in tricrystal Bi<sub>2</sub>Sr<sub>2</sub>CaCu<sub>2</sub>O<sub>8+δ</sub>," *Europhysics Letters*, vol. 36, no. 9, pp. 707–712, Dec. 1996. [Online]. Available: <http://dx.doi.org/10.1209/epl/i1996-00291-y>
  - [87] C. C. Tsuei, J. R. Kirtley, M. Rupp, J. Z. Sun, A. Gupta, M. B. Ketchen, C. A. Wang, Z. F. Ren, J. H. Wang, and M. Bhushan, "Pairing



- Symmetry in Single-Layer Tetragonal  $\text{Ti}_2\text{Ba}_2\text{CuO}_{6+\delta}$  Superconductors,” *Science*, vol. 271, no. 5247, p. 329, Jan. 1996. [Online]. Available: <http://science.sciencemag.org/content/271/5247/329.abstract>
- [88] A. M. Chang, H. D. Hallen, L. Harriott, H. F. Hess, H. L. Kao, J. Kwo, R. E. Miller, R. Wolfe, J. van der Ziel, and T. Y. Chang, “Scanning Hall probe microscopy,” *Applied Physics Letters*, vol. 61, no. 16, pp. 1974–1976, Jan. 1992. [Online]. Available: <https://doi.org/10.1063/1.108334>
- [89] L. Luan, O. M. Auslaender, D. A. Bonn, R. Liang, W. N. Hardy, and K. A. Moler, “Magnetic force microscopy study of interlayer kinks in individual vortices in the underdoped cuprate superconductor  $\text{YBa}_2\text{Cu}_3\text{O}_{6+x}$ ,” *Physical Review B*, vol. 79, no. 21, p. 214530, Jun. 2009. [Online]. Available: <https://link.aps.org/doi/10.1103/PhysRevB.79.214530>
- [90] J. Ge, J. Gutierrez, J. Cuppens, and V. V. Moshchalkov, “Observation of single flux quantum vortices in the intermediate state of a type-I superconducting film,” *Physical Review B*, vol. 88, no. 17, p. 174503, Nov. 2013. [Online]. Available: <https://link.aps.org/doi/10.1103/PhysRevB.88.174503>
- [91] J. Pearl, “Current distribution in superconducting films carrying quantized fluxoids,” *Applied Physics Letters*, vol. 5, no. 4, pp. 65–66, Jan. 1964. [Online]. Available: <https://doi.org/10.1063/1.1754056>
- [92] F. Tafuri, J. R. Kirtley, P. G. Medaglia, P. Orgiani, and G. Balestrino, “Magnetic Imaging of Pearl Vortices in Artificially Layered  $(\text{Ba}_{0.9}\text{Nd}_{0.1}\text{CuO}_{2+x})_m/(\text{CaCuO}_2)_n$  Systems,” *Physical Review Letters*, vol. 92, no. 15, p. 157006, Apr. 2004. [Online]. Available: <https://link.aps.org/doi/10.1103/PhysRevLett.92.157006>
- [93] R. Wölbing, T. Schwarz, B. Müller, J. Nagel, M. Kemmler, R. Kleiner, and D. Kölle, “Optimizing the spin sensitivity of grain boundary junction nanoSQUIDS—towards detection of small spin systems with single-spin resolution,” *Superconductor Science and Technology*, vol. 27, no. 12, p. 125007, 2014. [Online]. Available: <http://stacks.iop.org/0953-2048/27/i=12/a=125007>
- [94] L. Luan, O. M. Auslaender, T. M. Lippman, C. W. Hicks, B. Kalisky, J.-H. Chu, J. G. Analytis, I. R. Fisher, J. R. Kirtley, and K. A. Moler, “Local measurement of the penetration depth in the pnictide superconductor  $\text{Ba}(\text{Fe}_{0.95}\text{Co}_{0.05})_2\text{As}_2$ ,” *Physical Review B*, vol. 81, p. 100501, Mar 2010. [Online]. Available: <https://link.aps.org/doi/10.1103/PhysRevB.81.100501>
- [95] W. N. Hardy, D. A. Bonn, D. C. Morgan, R. Liang, and K. Zhang, “Precision measurements of the temperature dependence of  $\lambda$  in  $\text{YBa}_2\text{Cu}_3\text{O}_{6.95}$ : Strong evidence for nodes in the gap function,” *Physical Review Letters*, vol. 70, no. 25, pp. 3999–4002, Jun. 1993. [Online]. Available: <https://link.aps.org/doi/10.1103/PhysRevLett.70.3999>
- [96] L. Krusin-Elbaum, R. L. Greene, F. Holtzberg, A. P. Malozemoff, and Y. Yeshurun, “Direct Measurement of the Temperature-Dependent



- 
- Magnetic Penetration Depth in Y-Ba-Cu-O Crystals,” *Physical Review Letters*, vol. 62, no. 2, pp. 217–220, Jan. 1989. [Online]. Available: <https://link.aps.org/doi/10.1103/PhysRevLett.62.217>
- [97] A. Carrington, R. W. Giannetta, J. T. Kim, and J. Giapintzakis, “Absence of nonlinear Meissner effect in  $\text{YBa}_2\text{Cu}_3\text{O}_{6.95}$ ,” *Physical Review B*, vol. 59, no. 22, pp. R14 173–R14 176, Jun. 1999. [Online]. Available: <https://link.aps.org/doi/10.1103/PhysRevB.59.R14173>
- [98] A. T. Fiory, A. F. Hebard, P. M. Mankiewich, and R. E. Howard, “Penetration depths of high  $T_c$  films measured by two-coil mutual inductances,” *Applied Physics Letters*, vol. 52, no. 25, pp. 2165–2167, Jan. 1988. [Online]. Available: <https://doi.org/10.1063/1.99757>
- [99] J. Y. Lee, K. M. Paget, T. R. Lemberger, S. R. Foltyn, and X. Wu, “Crossover in temperature dependence of penetration depth  $\lambda(T)$  in superconducting  $\text{YBa}_2\text{Cu}_3\text{O}_{7-\delta}$  films,” *Physical Review B*, vol. 50, no. 5, pp. 3337–3341, Aug. 1994. [Online]. Available: <https://link.aps.org/doi/10.1103/PhysRevB.50.3337>
- [100] J. E. Sonier, J. H. Brewer, and R. F. Kiefl, “ $\mu$ -SR studies of the vortex state in type-II superconductors,” *Review of Modern Physics*, vol. 72, no. 3, pp. 769–811, Jul. 2000. [Online]. Available: <https://link.aps.org/doi/10.1103/RevModPhys.72.769>
- [101] L. Robledo, L. Childress, H. Bernien, B. Hensen, P. F. A. Alkemade, and R. Hanson, “High-fidelity projective read-out of a solid-state spin quantum register,” *Nature*, vol. 477, p. 574, Sep. 2011. [Online]. Available: <https://doi.org/10.1038/nature10401>
- [102] C. G. Yale, B. B. Buckley, D. J. Christle, G. Burkard, F. J. Heremans, L. C. Bassett, and D. D. Awschalom, “All-optical control of a solid-state spin using coherent dark states,” *Proc. Natl. Acad. Sci. USA*, vol. 110, no. 19, p. 7595, May 2013. [Online]. Available: <http://www.pnas.org/content/110/19/7595.abstract>
- [103] J. Ge, J. Gutierrez, J. Cuppens, and V. V. Moshchalkov, “Quantification of the flux tubes and the stability of stripe pattern in the intermediate state of a type-1 superconducting film,” *Physica C: Superconductivity and its Applications*, vol. 503, pp. 38–41, Aug. 2014. [Online]. Available: <http://www.sciencedirect.com/science/article/pii/S0921453414001348>
- [104] J. Gutierrez, B. Raes, A. V. Silhanek, L. J. Li, N. D. Zhigadlo, J. Karpinski, J. Tempere, and V. V. Moshchalkov, “Scanning Hall probe microscopy of unconventional vortex patterns in the two-gap  $\text{MgB}_2$  superconductor,” *Physical Review B*, vol. 85, no. 9, p. 094511, Mar. 2012. [Online]. Available: <https://link.aps.org/doi/10.1103/PhysRevB.85.094511>
- [105] E. Babaev and M. Speight, “Semi-Meissner state and neither type-I nor type-II superconductivity in multicomponent superconductors,” *Physical Review B*, vol. 72, no. 18, p. 180502, Nov. 2005. [Online]. Available: <https://link.aps.org/doi/10.1103/PhysRevB.72.180502>

- [106] L.-S. Bouchard, V. M. Acosta, E. Bauch, and D. Budker, "Detection of the Meissner effect with a diamond magnetometer," *New Journal of Physics*, vol. 13, no. 2, p. 025017, 2011. [Online]. Available: <http://stacks.iop.org/1367-2630/13/i=2/a=025017>
- [107] A. Waxman, Y. Schlussel, D. Groswasser, V. M. Acosta, L.-S. Bouchard, D. Budker, and R. Folman, "Diamond magnetometry of superconducting thin films," *Physical Review B*, vol. 89, no. 5, p. 054509, Feb. 2014. [Online]. Available: <https://link.aps.org/doi/10.1103/PhysRevB.89.054509>
- [108] N. M. Nusran, K. R. Joshi, K. Cho, M. A. Tanatar, W. R. Meier, S. L. Bud'ko, P. C. Canfield, Y. Liu, T. A. Lograsso, and R. Prozorov, "Spatially-resolved study of the Meissner effect in superconductors using NV-centers-in-diamond optical magnetometry," *New Journal of Physics*, vol. 20, no. 4, p. 043010, 2018. [Online]. Available: <http://stacks.iop.org/1367-2630/20/i=4/a=043010>
- [109] N. Alfasi, S. Masis, O. Shtempluck, V. Kochetok, and E. Buks, "Diamond magnetometry of Meissner currents in a superconducting film," *American Institute of Physics Advances*, vol. 6, no. 7, p. 075311, Jan. 2019. [Online]. Available: <https://doi.org/10.1063/1.4959225>
- [110] L. F. Chibotaru, A. Ceulemans, V. Bruyndoncx, and V. V. Moshchalkov, "Symmetry-induced formation of antivortices in mesoscopic superconductors," *Nature*, vol. 408, p. 833, Dec. 2000. [Online]. Available: <https://doi.org/10.1038/35048521>
- [111] R. B. Dinner, A. P. Robinson, S. C. Wimbush, J. L. MacManus-Driscoll, and M. G. Blamire, "Depairing critical current achieved in superconducting thin films with through-thickness arrays of artificial pinning centers," *Superconductor Science and Technology*, vol. 24, no. 5, p. 055017, Mar. 2011. [Online]. Available: <http://dx.doi.org/10.1088/0953-2048/24/5/055017>
- [112] K. Xu, P. Cao, and J. R. Heath, "Achieving the Theoretical Depairing Current Limit in Superconducting Nanomesh Films," *Nano Letters*, vol. 10, no. 10, pp. 4206–4210, Oct. 2010. [Online]. Available: <https://doi.org/10.1021/nl102584j>
- [113] L. Pauling, "The structure and entropy of ice and of other crystals with some randomness of atomic arrangement," *J. Am. Chem. Soc.*, vol. 57, no. 12, pp. 2680–2684, Dec. 1935. [Online]. Available: <https://doi.org/10.1021/ja01315a102>
- [114] L. J. Heyderman, "Crystal-clear order," *Nature Nanotechnology*, vol. 8, p. 705, Sep. 2013. [Online]. Available: <https://doi.org/10.1038/nnano.2013.193>
- [115] Y.-L. Wang, Z.-L. Xiao, A. Snezhko, J. Xu, L. E. Ocola, R. Divan, J. E. Pearson, G. W. Crabtree, and W.-K. Kwok, "Rewritable artificial magnetic charge ice," *Science*, vol. 352, no. 6288, p. 962, May 2016. [Online]. Available: <http://science.sciencemag.org/content/352/6288/962.abstract>

- 
- [116] E. Y. Vedmedenko, “Dynamics of bound monopoles in artificial spin ice: How to store energy in dirac strings,” *PRL*, vol. 116, no. 7, p. 077202, Feb. 2016. [Online]. Available: <https://link.aps.org/doi/10.1103/PhysRevLett.116.077202>
- [117] R. F. Wang, C. Nisoli, R. S. Freitas, J. Li, W. McConville, B. J. Cooley, M. S. Lund, N. Samarth, C. Leighton, V. H. Crespi, and P. Schiffer, “Artificial ‘spin ice’ in a geometrically frustrated lattice of nanoscale ferromagnetic islands,” *Nature*, vol. 439, p. 303, Jan. 2006. [Online]. Available: <https://doi.org/10.1038/nature04447>
- [118] A. Libál, C. J. O. Reichhardt, and C. Reichhardt, “Creating Artificial Ice States Using Vortices in Nanostructured Superconductors,” *Physical Review Letters*, vol. 102, p. 237004, Jun 2009. [Online]. Available: <https://link.aps.org/doi/10.1103/PhysRevLett.102.237004>
- [119] J. Trastoy, M. Malnou, C. Ulysse, R. Bernard, N. Bergeal, G. Faini, J. Lesueur, J. Briatico, and J. E. Villegas, “Freezing and thawing of artificial ice by thermal switching of geometric frustration in magnetic flux lattices,” *Nature Nanotechnology*, vol. 9, p. 710, Aug. 2014. [Online]. Available: <https://doi.org/10.1038/nnano.2014.158>
- [120] J. P. Morgan, A. Stein, S. Langridge, and C. H. Marrows, “Thermal ground-state ordering and elementary excitations in artificial magnetic square ice,” *Nature Physics*, vol. 7, p. 75, Nov. 2010. [Online]. Available: <https://doi.org/10.1038/nphys1853>
- [121] G. de Lange, D. Risté, V. V. Dobrovitski, and R. Hanson, “Single-Spin Magnetometry with Multipulse Sensing Sequences,” *Physical Review Letters*, vol. 106, no. 8, p. 080802, Feb. 2011. [Online]. Available: <https://link.aps.org/doi/10.1103/PhysRevLett.106.080802>
- [122] L. Embon, Y. Anahory, A. Suhov, D. Halbertal, J. Cuppens, A. Yakovenko, A. Uri, Y. Myasoedov, M. L. Rappaport, M. E. Huber, A. Gurevich, and E. Zeldov, “Probing dynamics and pinning of single vortices in superconductors at nanometer scales,” *Scientific Reports*, vol. 5, p. 7598, Jan. 2015. [Online]. Available: <https://doi.org/10.1038/srep07598>
- [123] L. Embon, Y. Anahory, . L. Jelić, E. O. Lachman, Y. Myasoedov, M. E. Huber, G. P. Mikitik, A. V. Silhanek, M. V. Milošević, A. Gurevich, and E. Zeldov, “Imaging of super-fast dynamics and flow instabilities of superconducting vortices,” *Nature Communications*, vol. 8, no. 1, p. 85, Jul. 2017. [Online]. Available: <https://doi.org/10.1038/s41467-017-00089-3>
- [124] K. S. Novoselov, A. K. Geim, S. V. Morozov, D. Jiang, Y. Zhang, S. V. Dubonos, I. V. Grigorieva, and A. A. Firsov, “Electric Field Effect in Atomically Thin Carbon Films,” *Science*, vol. 306, no. 5696, pp. 666–669, 2004. [Online]. Available: <http://science.sciencemag.org/content/306/5696/666>
- [125] C. R. Dean, A. F. Young, I. Meric, C. Lee, L. Wang, S. Sorgenfrei, K. Watanabe, T. Taniguchi, P. Kim, K. L. Shepard, and J. Hone, “Boron nitride substrates

- for high-quality graphene electronics,” *Nature Nanotechnology*, vol. 5, p. 722, Aug. 2010. [Online]. Available: <https://doi.org/10.1038/nnano.2010.172>
- [126] D. Pacilé, J. C. Meyer, C. O. Girit, and A. Zettl, “The two-dimensional phase of boron nitride: Few-atomic-layer sheets and suspended membranes,” *Applied Physics Letters*, vol. 92, no. 13, p. 133107, 2008. [Online]. Available: <https://doi.org/10.1063/1.2903702>
- [127] I. Meric, C. R. Dean, N. Petrone, L. Wang, J. Hone, P. Kim, and K. L. Shepard, “Graphene Field-Effect Transistors Based on Boron–Nitride Dielectrics,” *Proceedings of the IEEE*, vol. 101, pp. 1609–1619, 2013. [Online]. Available: <https://www.semanticscholar.org/paper/Graphene-Field-Effect-Transistors-Based-on-Meric-Dean/16a47b9b3e0ace931d65aa373e98787c74b4b9e4>
- [128] M. Osada and T. Sasaki, “Two-Dimensional Dielectric Nanosheets: Novel Nanoelectronics From Nanocrystal Building Blocks,” *Advanced Materials*, vol. 24, no. 2, pp. 210–228, 2011. [Online]. Available: <https://onlinelibrary.wiley.com/doi/abs/10.1002/adma.201103241>
- [129] K. F. Mak, C. Lee, J. Hone, J. Shan, and T. F. Heinz, “Atomically Thin MoS<sub>2</sub>: A New Direct-Gap Semiconductor,” *Physical Review Letters*, vol. 105, p. 136805, Sep 2010. [Online]. Available: <https://link.aps.org/doi/10.1103/PhysRevLett.105.136805>
- [130] Y. Ding, Y. Wang, J. Ni, L. Shi, S. Shi, and W. Tang, “First principles study of structural, vibrational and electronic properties of graphene-like MX<sub>2</sub> (M=Mo, Nb, W, Ta; X=S, Se, Te) monolayers,” *Physica B: Condensed Matter*, vol. 406, no. 11, pp. 2254 – 2260, 2011. [Online]. Available: <http://www.sciencedirect.com/science/article/pii/S0921452611002651>
- [131] Z. Fei, W. Zhao, T. A. Palomaki, B. Sun, M. K. Miller, Z. Zhao, J. Yan, X. Xu, and D. H. Cobden, “Ferroelectric switching of a two-dimensional metal,” *Nature*, vol. 560, no. 7718, pp. 336–339, Aug. 2018. [Online]. Available: <https://doi.org/10.1038/s41586-018-0336-3>
- [132] J. M. Lu, O. Zheliuk, I. Leermakers, N. F. Q. Yuan, U. Zeitler, K. T. Law, and J. T. Ye, “Evidence for two-dimensional Ising superconductivity in gated MoS<sub>2</sub>,” *Science*, vol. 350, no. 6266, pp. 1353–1357, 2015. [Online]. Available: <http://science.sciencemag.org/content/350/6266/1353>
- [133] X. Xi, L. Zhao, Z. Wang, H. Berger, L. Forró, J. Shan, and K. F. Mak, “Strongly enhanced charge-density-wave order in monolayer NbSe<sub>2</sub>,” *Nature Nanotechnology*, vol. 10, p. 765, Jul. 2015. [Online]. Available: <https://doi.org/10.1038/nnano.2015.143>
- [134] K. Chang, J. Liu, H. Lin, N. Wang, K. Zhao, A. Zhang, F. Jin, Y. Zhong, X. Hu, W. Duan, Q. Zhang, L. Fu, Q.-K. Xue, X. Chen, and S.-H. Ji, “Discovery of robust in-plane ferroelectricity in atomic-thick SnTe,” *Science*, vol. 353, no. 6296, pp. 274–278, 2016. [Online]. Available: <http://science.sciencemag.org/content/353/6296/274>

- 
- [135] S. Hastrup, M. Strange, M. Pandey, T. Deilmann, P. S. Schmidt, N. F. Hinsche, M. N. Gjerding, D. Torelli, P. M. Larsen, A. C. Riis-Jensen, J. Gath, K. W. Jacobsen, J. J. Mortensen, T. Olsen, and K. S. Thygesen, “The Computational 2D Materials Database: high-throughput modeling and discovery of atomically thin crystals,” *2D Materials*, vol. 5, no. 4, p. 042002, 2018. [Online]. Available: <http://stacks.iop.org/2053-1583/5/i=4/a=042002>
- [136] L. Britnell, R. V. Gorbachev, R. Jalil, B. D. Belle, F. Schedin, A. Mishchenko, T. Georgiou, M. I. Katsnelson, L. Eaves, S. V. Morozov, N. M. R. Peres, J. Leist, A. K. Geim, K. S. Novoselov, and L. A. Ponomarenko, “Field-effect tunneling transistor based on vertical graphene heterostructures,” *Science*, vol. 335, no. 6071, pp. 947–950, 2012. [Online]. Available: <http://science.sciencemag.org/content/335/6071/947>
- [137] F. Bonaccorso, Z. Sun, T. Hasan, and A. C. Ferrari, “Graphene photonics and optoelectronics,” *Nature Photonics*, vol. 4, p. 611, Aug. 2010. [Online]. Available: <https://doi.org/10.1038/nphoton.2010.186>
- [138] Q. H. Wang, K. Kalantar-Zadeh, A. Kis, J. N. Coleman, and M. S. Strano, “Electronics and optoelectronics of two-dimensional transition metal dichalcogenides,” *Nature Nanotechnology*, vol. 7, p. 699, Nov. 2012. [Online]. Available: <https://doi.org/10.1038/nnano.2012.193>
- [139] F. H. L. Koppens, T. Mueller, P. Avouris, A. C. Ferrari, M. S. Vitiello, and M. Polini, “Photodetectors based on graphene, other two-dimensional materials and hybrid systems,” *Nature Nanotechnology*, vol. 9, p. 780, Oct. 2014. [Online]. Available: <https://doi.org/10.1038/nnano.2014.215>
- [140] K. Roy, M. Padmanabhan, S. Goswami, T. P. Sai, G. Ramalingam, S. Raghavan, and A. Ghosh, “Graphene-MoS<sub>2</sub> hybrid structures for multifunctional photoresponsive memory devices,” *Nature Nanotechnology*, vol. 8, p. 826, Oct. 2013. [Online]. Available: <https://doi.org/10.1038/nnano.2013.206>
- [141] R. Cheng, D. Li, H. Zhou, C. Wang, A. Yin, S. Jiang, Y. Liu, Y. Chen, Y. Huang, and X. Duan, “Electroluminescence and Photocurrent Generation from Atomically Sharp WSe<sub>2</sub>/MoS<sub>2</sub> Heterojunction p-n Diodes,” *Nano Letters*, vol. 14, no. 10, pp. 5590–5597, Oct. 2014. [Online]. Available: <https://doi.org/10.1021/nl502075n>
- [142] B. Huang, G. Clark, E. Navarro-Moratalla, D. R. Klein, R. Cheng, K. L. Seyler, D. Zhong, E. Schmidgall, M. A. McGuire, D. H. Cobden, W. Yao, D. Xiao, P. Jarillo-Herrero, and X. Xu, “Layer-dependent ferromagnetism in a van der Waals crystal down to the monolayer limit,” *Nature*, vol. 546, p. 270, Jun. 2017. [Online]. Available: <https://doi.org/10.1038/nature22391>
- [143] C. Gong, L. Li, Z. Li, H. Ji, A. Stern, Y. Xia, T. Cao, W. Bao, C. Wang, Y. Wang, Z. Q. Qiu, R. J. Cava, S. G. Louie, J. Xia, and X. Zhang, “Discovery of intrinsic ferromagnetism in two-dimensional van der Waals crystals,” *Nature*, vol. 546, p. 265, Apr. 2017. [Online]. Available: <https://doi.org/10.1038/nature22060>

- [144] M. Bonilla, S. Kolekar, Y. Ma, H. C. Diaz, V. Kalappattil, R. Das, T. Eggers, H. R. Gutierrez, M.-H. Phan, and M. Batzill, “Strong room-temperature ferromagnetism in VSe<sub>2</sub> monolayers on van der Waals substrates,” *Nature Nanotechnology*, vol. 13, no. 4, pp. 289–293, Apr. 2018. [Online]. Available: <https://doi.org/10.1038/s41565-018-0063-9>
- [145] N. D. Mermin and H. Wagner, “Absence of Ferromagnetism or Antiferromagnetism in One- or Two-Dimensional Isotropic Heisenberg Models,” *Physical Review Letters*, vol. 17, pp. 1133–1136, Nov 1966. [Online]. Available: <https://link.aps.org/doi/10.1103/PhysRevLett.17.1133>
- [146] T. Song, X. Cai, M. W.-Y. Tu, X. Zhang, B. Huang, N. P. Wilson, K. L. Seyler, L. Zhu, T. Taniguchi, K. Watanabe, M. A. McGuire, D. H. Cobden, D. Xiao, W. Yao, and X. Xu, “Giant tunneling magnetoresistance in spin-filter van der Waals heterostructures,” *Science*, 2018. [Online]. Available: <http://science.sciencemag.org/content/early/2018/05/02/science.aar4851>
- [147] D. R. Klein, D. MacNeill, J. L. Lado, D. Soriano, E. Navarro-Moratalla, K. Watanabe, T. Taniguchi, S. Manni, P. Canfield, J. Fernández-Rossier, and P. Jarillo-Herrero, “Probing magnetism in 2D van der Waals crystalline insulators via electron tunneling,” *Science*, vol. 360, no. 6394, pp. 1218–1222, 2018. [Online]. Available: <http://science.sciencemag.org/content/360/6394/1218>
- [148] S. Jiang, L. Li, Z. Wang, J. Shan, and K. F. Mak, “Spin transistor built on 2D van der Waals heterostructures,” *ArXiv e-prints*, Jul. 2018. [Online]. Available: <https://arxiv.org/abs/1807.04898>
- [149] Z. Wang, I. Gutiérrez-Lezama, N. Ubrig, M. Kroner, M. Gibertini, T. Taniguchi, K. Watanabe, A. Imamoglu, E. Giannini, and A. F. Morpurgo, “Very large tunneling magnetoresistance in layered magnetic semiconductor CrI<sub>3</sub>,” *Nature Communications*, vol. 9, no. 1, p. 2516, Jun. 2018. [Online]. Available: <https://doi.org/10.1038/s41467-018-04953-8>
- [150] H. H. Kim, B. Yang, T. Patel, F. Sfigakis, C. Li, S. Tian, H. Lei, and A. W. Tsen, “One Million Percent Tunnel Magnetoresistance in a Magnetic van der Waals Heterostructure,” *Nano Letters*, vol. 18, no. 8, pp. 4885–4890, Aug. 2018. [Online]. Available: <https://doi.org/10.1021/acs.nanolett.8b01552>
- [151] S. Jiang, J. Shan, and K. F. Mak, “Electric-field switching of two-dimensional van der Waals magnets,” *Nature Materials*, vol. 17, no. 5, pp. 406–410, May 2018. [Online]. Available: <https://doi.org/10.1038/s41563-018-0040-6>
- [152] S. Jiang, L. Li, Z. Wang, K. F. Mak, and J. Shan, “Controlling magnetism in 2D CrI<sub>3</sub> by electrostatic doping,” *Nature Nanotechnology*, vol. 13, no. 7, pp. 549–553, Jul. 2018. [Online]. Available: <https://doi.org/10.1038/s41565-018-0135-x>
- [153] B. Huang, G. Clark, D. R. Klein, D. MacNeill, E. Navarro-Moratalla, K. L. Seyler, N. Wilson, M. A. McGuire, D. H. Cobden, D. Xiao, W. Yao, P. Jarillo-Herrero, and X. Xu, “Electrical control of 2D magnetism in bilayer

- CrI<sub>3</sub>,” *Nature Nanotechnology*, vol. 13, no. 7, pp. 544–548, Jul. 2018. [Online]. Available: <https://doi.org/10.1038/s41565-018-0121-3>
- [154] D. Zhong, K. L. Seyler, X. Linpeng, R. Cheng, N. Sivadas, B. Huang, E. Schmidgall, T. Taniguchi, K. Watanabe, M. A. McGuire, W. Yao, D. Xiao, K.-M. C. Fu, and X. Xu, “Van der Waals engineering of ferromagnetic semiconductor heterostructures for spin and valleytronics,” *Science Advances*, vol. 3, no. 5, 2017. [Online]. Available: <http://advances.sciencemag.org/content/3/5/e1603113>
- [155] K. L. Seyler, D. Zhong, D. R. Klein, S. Gao, X. Zhang, B. Huang, E. Navarro-Moratalla, L. Yang, D. H. Cobden, M. A. McGuire, W. Yao, D. Xiao, P. Jarillo-Herrero, and X. Xu, “Ligand-field helical luminescence in a 2D ferromagnetic insulator,” *Nature Physics*, vol. 14, no. 3, pp. 277–281, Mar. 2018. [Online]. Available: <https://doi.org/10.1038/s41567-017-0006-7>
- [156] Z. Fei, B. Huang, P. Malinowski, W. Wang, T. Song, J. Sanchez, W. Yao, D. Xiao, X. Zhu, A. F. May, W. Wu, D. H. Cobden, J.-H. Chu, and X. Xu, “Two-dimensional itinerant ferromagnetism in atomically thin Fe<sub>3</sub>GeTe<sub>2</sub>,” *Nature Materials*, vol. 17, no. 9, pp. 778–782, Sep. 2018. [Online]. Available: <https://doi.org/10.1038/s41563-018-0149-7>
- [157] W.-B. Zhang, Q. Qu, P. Zhu, and C.-H. Lam, “Robust intrinsic ferromagnetism and half semiconductivity in stable two-dimensional single-layer chromium trihalides,” *Journal of Materials Chemistry C*, vol. 3, pp. 12 457–12 468, 2015. [Online]. Available: <http://dx.doi.org/10.1039/C5TC02840J>
- [158] J. Cable, M. Wilkinson, and E. Wollan, “Neutron diffraction investigation of antiferromagnetism in CrCl<sub>3</sub>,” *Journal of Physics and Chemistry of Solids*, vol. 19, no. 1, pp. 29 – 34, 1961. [Online]. Available: <http://www.sciencedirect.com/science/article/pii/0022369761900531>
- [159] I. Tsubokawa, “On the Magnetic Properties of a CrBr<sub>3</sub> Single Crystal,” *Journal of the Physical Society of Japan*, vol. 15, no. 9, pp. 1664–1668, 1960. [Online]. Available: <https://doi.org/10.1143/JPSJ.15.1664>
- [160] M. A. McGuire, H. Dixit, V. R. Cooper, and B. C. Sales, “Coupling of Crystal Structure and Magnetism in the Layered, Ferromagnetic Insulator CrI<sub>3</sub>,” *Chemistry of Materials*, vol. 27, no. 2, pp. 612–620, Jan. 2015. [Online]. Available: <https://doi.org/10.1021/cm504242t>
- [161] J. M. Friedt and J. P. Sanchez, “Origin of the magnetic hyperfine field transferred at iodine in ferromagnetic CrI<sub>3</sub>,” *Journal of Physics C: Solid State Physics*, vol. 11, no. 17, p. 3731, 1978. [Online]. Available: <http://stacks.iop.org/0022-3719/11/i=17/a=024>
- [162] P. Jiang, C. Wang, D. Chen, Z. Zhong, Z. Yuan, Z.-Y. Lu, and W. Ji, “Stacking tunable interlayer magnetism in bilayer CrI<sub>3</sub>,” *ArXiv e-prints*, Jun. 2018. [Online]. Available: <https://arxiv.org/abs/1806.09274>



- [163] J. M. D. Coey, *Magnetism and Magnetic Materials*. Cambridge University Press, 2010.
- [164] J. B. Goodenough, *Magnetism and the Chemical Bond*. Interscience-Wiley, 1963.
- [165] J. L. Lado and J. Fernández-Rossier, “On the origin of magnetic anisotropy in two dimensional  $\text{CrI}_3$ ,” *2D Materials*, vol. 4, no. 3, p. 035002, 2017. [Online]. Available: <http://stacks.iop.org/2053-1583/4/i=3/a=035002>
- [166] J. F. Dillon and C. E. Olson, “Magnetization, Resonance, and Optical Properties of the Ferromagnet  $\text{CrI}_3$ ,” *Journal of Applied Physics*, vol. 36, no. 3, pp. 1259–1260, 1965. [Online]. Available: <https://doi.org/10.1063/1.1714194>
- [167] N. Sivadas, S. Okamoto, and D. Xiao, “Gate-Controllable Magneto-optic Kerr Effect in Layered Collinear Antiferromagnets,” *Physical Review Letters*, vol. 117, p. 267203, Dec 2016. [Online]. Available: <https://link.aps.org/doi/10.1103/PhysRevLett.117.267203>
- [168] D. Soriano, C. Cardoso, and J. Fernández-Rossier, “Interplay between interlayer exchange and stacking in  $\text{CrI}_3$  bilayers,” *ArXiv e-prints*, Jul. 2018. [Online]. Available: <https://arxiv.org/abs/1807.00357>
- [169] S. W. Jang, M. Y. Jeong, H. Yoon, S. Ryee, and M. J. Han, “Microscopic understanding of magnetic interactions in bilayer  $\text{CrI}_3$ ,” *ArXiv e-prints*, Sep. 2018. [Online]. Available: <https://arxiv.org/abs/1809.01388>
- [170] L. Wang, I. Meric, P. Y. Huang, Q. Gao, Y. Gao, H. Tran, T. Taniguchi, K. Watanabe, L. M. Campos, D. A. Muller, J. Guo, P. Kim, J. Hone, K. L. Shepard, and C. R. Dean, “One-Dimensional Electrical Contact to a Two-Dimensional Material,” *Science*, vol. 342, no. 6158, pp. 614–617, 2013. [Online]. Available: <http://science.sciencemag.org/content/342/6158/614>
- [171] T. Hingant, J.-P. Tetienne, L. J. Martínez, K. Garcia, D. Ravelosona, J.-F. Roch, and V. Jacques, “Measuring the Magnetic Moment Density in Patterned Ultrathin Ferromagnets with Submicrometer Resolution,” *Physical Review Applied*, vol. 4, p. 014003, Jul 2015. [Online]. Available: <https://link.aps.org/doi/10.1103/PhysRevApplied.4.014003>
- [172] F. Garcia-Sanchez, P. Borys, A. Vansteenkiste, J.-V. Kim, and R. L. Stamps, “Nonreciprocal spin-wave channeling along textures driven by the Dzyaloshinskii-Moriya interaction,” *Physical Review B*, vol. 89, p. 224408, Jun 2014. [Online]. Available: <https://link.aps.org/doi/10.1103/PhysRevB.89.224408>
- [173] S. Djurdjic, M. J. Mijin, A. Šolajić, J. Pešić, M. Šćepanović, Y. Liu, A. Baum, C. Petrovic, N. Lazarević, and Z. V. Popović, “Lattice dynamics and phase transition in  $\text{CrI}_3$  single crystals,” *Physical Review B*, vol. 98, p. 104307, Sep 2018. [Online]. Available: <https://link.aps.org/doi/10.1103/PhysRevB.98.104307>



- 
- [174] S. S. P. Parkin, M. Hayashi, and L. Thomas, “Magnetic Domain-Wall Racetrack Memory,” *Science*, vol. 320, no. 5873, p. 190, Apr. 2008. [Online]. Available: <http://science.sciencemag.org/content/320/5873/190.abstract>
- [175] L. Chen, J.-H. Chung, B. Gao, T. Chen, M. B. Stone, A. I. Kolesnikov, Q. Huang, and P. Dai, “Topological Spin Excitations in Honeycomb Ferromagnet  $\text{CrI}_3$ ,” *Physical Review X*, vol. 8, no. 4, p. 041028, Nov. 2018. [Online]. Available: <https://link.aps.org/doi/10.1103/PhysRevX.8.041028>
- [176] P. Chauve, T. Giamarchi, and P. Le Doussal, “Creep and depinning in disordered media,” *Physical Review B*, vol. 62, no. 10, pp. 6241–6267, Sep. 2000. [Online]. Available: <https://link.aps.org/doi/10.1103/PhysRevB.62.6241>
- [177] E. E. Ferrero, L. Foini, T. Giamarchi, A. B. Kolton, and A. Rosso, “Spatiotemporal Patterns in Ultraslow Domain Wall Creep Dynamics,” *Physical Review Letters*, vol. 118, no. 14, p. 147208, Apr. 2017. [Online]. Available: <https://link.aps.org/doi/10.1103/PhysRevLett.118.147208>
- [178] P. J. Metaxas, J. P. Jamet, A. Mougin, M. Cormier, J. Ferré, V. Baltz, B. Rodmacq, B. Dieny, and R. L. Stamps, “Creep and Flow Regimes of Magnetic Domain-Wall Motion in Ultrathin Pt/Co/Pt Films with Perpendicular Anisotropy,” *Physical Review Letters*, vol. 99, no. 21, p. 217208, Nov. 2007. [Online]. Available: <https://link.aps.org/doi/10.1103/PhysRevLett.99.217208>
- [179] T. Moriya, “Anisotropic Superexchange Interaction and Weak Ferromagnetism,” *Physical Review*, vol. 120, no. 1, pp. 91–98, Oct. 1960. [Online]. Available: <https://link.aps.org/doi/10.1103/PhysRev.120.91>
- [180] J. Liu, M. Shi, P. Mo, and J. Lu, “Electrical-field-induced magnetic Skyrmion ground state in a two-dimensional chromium tri-iodide ferromagnetic monolayer,” *American Institute of Physics Advances*, vol. 8, no. 5, p. 055316, Nov. 2018. [Online]. Available: <https://doi.org/10.1063/1.5030441>
- [181] A. V. Chumak, V. Vasyuchka, A. Serga, and B. Hillebrands, “Magnon spintronics,” *Nature Physics*, vol. 11, p. 453, Jun. 2015. [Online]. Available: <https://doi.org/10.1038/nphys3347>
- [182] S. Neusser and D. Grundler, “Magnonics: Spin Waves on the Nanoscale,” *Advanced Materials*, vol. 21, no. 28, pp. 2927–2932, Feb. 2009. [Online]. Available: <https://doi.org/10.1002/adma.200900809>
- [183] J. M. Winter, “Bloch Wall Excitation. Application to Nuclear Resonance in a Bloch Wall,” *Physical Review*, vol. 124, no. 2, pp. 452–459, Oct. 1961. [Online]. Available: <https://link.aps.org/doi/10.1103/PhysRev.124.452>
- [184] K. Wagner, A. Kákay, K. Schultheiss, A. Henschke, T. Sebastian, and H. Schultheiss, “Magnetic domain walls as reconfigurable spin-wave nanochannels,” *Nature Nanotechnology*, vol. 11, p. 432, Feb. 2016. [Online]. Available: <https://doi.org/10.1038/nnano.2015.339>

- [185] A. Haldar, D. Kumar, and A. O. Adeyeye, “A reconfigurable waveguide for energy-efficient transmission and local manipulation of information in a nanomagnetic device,” *Nature Nanotechnology*, vol. 11, p. 437, Feb. 2016. [Online]. Available: <https://doi.org/10.1038/nnano.2015.332>
- [186] V. Sluka, T. Schneider, R. A. Gallardo, A. Kakay, M. Weigand, T. Warnatz, R. Mattheis, A. Roldan-Molina, P. Landeros, V. Tiberkevich, A. Slavin, G. Schütz, A. Erbe, A. Deac, J. Lindner, J. Raabe, J. Fassbender, and S. Wintz, “Emission and Propagation of Multi-Dimensional Spin Waves with nanoscale wavelengths in Anisotropic Spin Textures,” *arXiv e-prints*, p. arXiv:1807.00897, Jul. 2018.
- [187] P. Andrich, C. F. de las Casas, X. Liu, H. L. Bretscher, J. R. Berman, F. J. Heremans, P. F. Nealey, and D. D. Awschalom, “Long-range spin wave mediated control of defect qubits in nanodiamonds,” *npj Quantum Information*, vol. 3, no. 1, p. 28, Jul. 2017. [Online]. Available: <https://doi.org/10.1038/s41534-017-0029-z>
- [188] A. K. Geim and K. S. Novoselov, “The rise of graphene,” *Nature Materials*, vol. 6, p. 183, Mar. 2007. [Online]. Available: <https://doi.org/10.1038/nmat1849>
- [189] A. F. Young and P. Kim, “Electronic Transport in Graphene Heterostructures,” *Annual Review of Condensed Matter Physics*, vol. 2, no. 1, pp. 101–120, Jan. 2011. [Online]. Available: <https://doi.org/10.1146/annurev-conmatphys-062910-140458>
- [190] S. Das Sarma, S. Adam, E. H. Hwang, and E. Rossi, “Electronic transport in two-dimensional graphene,” *Review of Modern Physics*, vol. 83, no. 2, pp. 407–470, May 2011. [Online]. Available: <https://link.aps.org/doi/10.1103/RevModPhys.83.407>
- [191] A. S. Mayorov, R. V. Gorbachev, S. V. Morozov, L. Britnell, R. Jalil, L. A. Ponomarenko, P. Blake, K. S. Novoselov, K. Watanabe, T. Taniguchi, and A. K. Geim, “Micrometer-Scale Ballistic Transport in Encapsulated Graphene at Room Temperature,” *Nano Letters*, vol. 11, no. 6, pp. 2396–2399, Jun. 2011. [Online]. Available: <https://doi.org/10.1021/nl200758b>
- [192] V. S. Tsoi, J. Bass, and P. Wyder, “Studying conduction-electron/interface interactions using transverse electron focusing,” *Review of Modern Physics*, vol. 71, no. 5, pp. 1641–1693, Oct. 1999. [Online]. Available: <https://link.aps.org/doi/10.1103/RevModPhys.71.1641>
- [193] L. P. Rokhinson, V. Larkina, Y. B. Lyanda-Geller, L. N. Pfeiffer, and K. W. West, “Spin Separation in Cyclotron Motion,” *Physical Review Letters*, vol. 93, no. 14, p. 146601, Sep. 2004. [Online]. Available: <https://link.aps.org/doi/10.1103/PhysRevLett.93.146601>
- [194] V. J. Goldman, B. Su, and J. K. Jain, “Detection of composite fermions by magnetic focusing,” *Physical Review Letters*, vol. 72, no. 13, pp. 2065–2068,

- Mar. 1994. [Online]. Available: <https://link.aps.org/doi/10.1103/PhysRevLett.72.2065>
- [195] T. Taychatanapat, K. Watanabe, T. Taniguchi, and P. Jarillo-Herrero, “Electrically tunable transverse magnetic focusing in graphene,” *Nature Physics*, vol. 9, p. 225, Feb. 2013. [Online]. Available: <https://doi.org/10.1038/nphys2549>
- [196] K. S. Novoselov, A. K. Geim, S. V. Morozov, D. Jiang, M. I. Katsnelson, I. V. Grigorieva, S. V. Dubonos, and A. A. Firsov, “Two-dimensional gas of massless Dirac fermions in graphene,” *Nature*, vol. 438, p. 197, Nov. 2005. [Online]. Available: <https://doi.org/10.1038/nature04233>
- [197] G. Li, A. Luican-Mayer, D. Abanin, L. Levitov, and E. Y. Andrei, “Evolution of landau levels into edge states in graphene,” *Nature Communications*, vol. 4, p. 1744, Apr. 2013. [Online]. Available: <https://doi.org/10.1038/ncomms2767>
- [198] J. R. Williams, D. A. Abanin, L. DiCarlo, L. S. Levitov, and C. M. Marcus, “Quantum Hall conductance of two-terminal graphene devices,” *Physical Review B*, vol. 80, no. 4, p. 045408, Jul. 2009. [Online]. Available: <https://link.aps.org/doi/10.1103/PhysRevB.80.045408>
- [199] J. Weis and von Klitzing K., “Metrology and microscopic picture of the integer quantum Hall effect,” *Philosophical Transactions of the Royal Society A: Mathematical, Physical and Engineering Sciences*, vol. 369, no. 1953, pp. 3954–3974, Mar. 2011. [Online]. Available: <https://doi.org/10.1098/rsta.2011.0198>
- [200] D. Ghazaryan, M. T. Greenaway, Z. Wang, V. H. Guarochico-Moreira, I. J. Vera-Marun, J. Yin, Y. Liao, S. V. Morozov, O. Kristanovski, A. I. Lichtenstein, M. I. Katsnelson, F. Withers, A. Mishchenko, L. Eaves, A. K. Geim, K. S. Novoselov, and A. Misra, “Magnon-assisted tunnelling in van der Waals heterostructures based on CrBr<sub>3</sub>,” *Nature Electronics*, vol. 1, no. 6, pp. 344–349, Jun. 2018. [Online]. Available: <https://doi.org/10.1038/s41928-018-0087-z>
- [201] A. Y. Meltzer, E. Levin, and E. Zeldov, “Direct Reconstruction of Two-Dimensional Currents in Thin Films from Magnetic-Field Measurements,” *Physical Review Applied*, vol. 8, no. 6, p. 064030, Dec. 2017. [Online]. Available: <https://link.aps.org/doi/10.1103/PhysRevApplied.8.064030>
- [202] C. P. Slichter, *Principles of Magnetic Resonance*, H. Springer, Berlin, Ed. Springer-Verlag Berlin Heidelberg, 1990. [Online]. Available: <https://link.springer.com/book/10.1007%2F978-3-662-09441-9#authorsandaffiliationsbook>
- [203] S. Rohart and A. Thiaville, “Skyrmion confinement in ultrathin film nanostructures in the presence of Dzyaloshinskii-Moriya interaction,” *Physical Review B*, vol. 88, p. 184422, Nov. 2013. [Online]. Available: <https://link.aps.org/doi/10.1103/PhysRevB.88.184422>



# Curriculum Vitae

## Personal Details

Name	Lucas Thiel
Date of Birth	31 of March 1990
Place of Birth	Lörrach, Germany
email	<a href="mailto:lucasthiel.physics@gmail.com">lucasthiel.physics@gmail.com</a>

## Education

2014-2019	University of Basel, Quantum Sensing Group, PhD
2013-2014	Havard University, Master thesis
2011-2014	University of Basel, Master of Science in Physics
2008-2011	University of Basel, Bachelor of Science in Nanoscience
2000-2008	Hebelgymnasium Lörrach, Abitur

## Publications

- [204] L. Thiel, Z. Wang, M. A. Tschudin, D. Rohner, I. Gutiérrez-Lezama, N. Ubrig, M. Gibertini, E. Giannini, A. F. Morpurgo, and P. Maletinsky, “Probing magnetism in 2D materials at the nanoscale with single spin microscopy”, *arXiv e-prints*, 1902.01406 (2019), accepted in Science
- [205] J. Kölbl, A. Barfuss, M. Kasperczyk, L. Thiel, A. Clerk, H. Ribeiro, P. Maletinsky, “Initialization of single spin dressed states using shortcuts to adiabaticity”, *Physical Review Letters*, **122**, 090502 (2019)
- [206] V. M. Acosta, L. S. Bouchard, D. Budker, R. Folman, T. Lenz, P. Maletinsky, D. Rohner, Y. Schlusser, L. Thiel, “Color centers in diamond as novel probes of superconductivity”, *Journal of Superconductivity and Novel Magnetism* **32**, 85 (2019)
- [207] D. Rohner\*, L. Thiel\*, B. Müller, M. Kasperczyk, R. Kleiner, D. Kölle, and P. Maletinsky, “Real-Space Probing of the Local Magnetic Response of Thin-Film Superconductors Using Single Spin Magnetometry”, *Sensors* **18**, 11 (2018)
- [208] Y. Schlusser, T. Lenz, D. Rohner, Y. Bar-Haim, L. Bougas, D. Groswasser, M. Kieschnick, E. Rozenberg, L. Thiel, A. Waxman, J. Meijer, P. Maletinsky, D. Budker, and R. Folman, “Wide-Field Imaging of Superconductor Vortices with Electron Spins in Diamond”, *Physical Review Applied* **10**, 034032 (2018)

- [209] A. Barfuss, J. Kölbl, L. Thiel, J. Teissier, M. Kasperczyk, P. Maletinsky, “Phase-controlled coherent dynamics of a single spin under closed-contour interaction” in *Nature Physics* **14**, 1087 (2018)
- [210] L. Thiel, D. Rohner, M. Ganzhorn, P. Appel, E. Neu, B. Müller, R. Kleiner, D. Kölle, and P. Maletinsky, “Quantitative nanoscale vortex imaging using a cryogenic quantum magnetometer”, *Nature Nanotechnology* **11**, 677 (2016)
- [211] M. S. Grinolds, M. Warner, K. De Greve, Y. Dovzhenko, L. Thiel, R. L. Walsworth, S. Hong, P. Maletinsky, and A. Yacoby, “Subnanometre resolution in three-dimensional magnetic resonance imaging of individual dark spins”, *Nature Nanotechnology* **9**, 279 (2014)

March 8, 2019